

SINFONI observations of Nearby AGN
and
Design of an interferometric integral-field
spectrograph for the LBT

DISSERTATION



submitted to the
Faculty of Physics of the Ludwig Maximilians University of München, Germany
for the degree of
Doctor of Natural Sciences
Dr. rer. nat

presented by
Francisco Müller Sánchez
born in Mexico City, Mexico

April 2008

1. Gutachter: Prof. Dr. Reinhard Genzel
2. Gutachter: Prof. Dr. Ortwin Gerhard
Datum der Einreichung: 14. April 2008
Datum der mündlichen Prüfung: 17. Juni 2008

Zusammenfassung

Der starke Energieausstoß von Aktiven Galaxienkernen (AGN) beruht auf der Akkretion von Materie auf ein supermassives Schwarzes Loch (SMBH) und impliziert ein Gasreservoir in der Nähe des AGN. Gemäß dem Standardmodell für AGN spielt das Gas auch eine wichtige Rolle für die winkelabhängige Bedeckung des Kerns durch einen molekularen bzw. staubigen Torus. Im Falle von AGN des Typs 2 schneidet die Sichtlinie den Torus (“edge-on”) und verdeckt die breiten Emissionslinien. Beim Typ 1 verläuft die Sichtlinie etwa senkrecht zur Ebene des Torus (“pole-on”), was die Beobachtung breiter Emissionslinien aus der Nähe des SMBH erlaubt. Ein weiteres bedeutsames Gebiet der AGN-Forschung - neben der Verteilung und Dynamik des Gases - befasst sich mit der Wechselwirkung von AGN und Gebieten starker Sternentstehung (“starburst regions”) die im Umkreis von einigen Parsec um AGN beobachtet werden. Die Beobachtung dieser Sternentstehungsgebiete führt zu der Frage wie sich AGN und Sternentstehung gegenseitig beeinflussen.

Gegenstand dieser Dissertation ist die Physik der Sternentstehung und des molekularen Gases in ausgewählten nahegelegenen AGN. Diese Arbeit beruht auf räumlich hochaufgelösten Daten bei nahinfraroten Wellenlängen, die mit dem abbildenden Spektrometer SINFONI am Very Large Telescope unter Verwendung einer adaptiver Optik gewonnen wurden. Die beiden untersuchten Zielobjekte – die Circinus-Galaxie und NGC1068 – gehören zu den auffälligsten und hellsten Seyfert-2-Galaxien.

In Falle von Circinus ähneln die Emissionslinien von H_2 1–0 S(1) und $Br\gamma$ dem stellaren Kontinuum in Bezug auf Kinematik und Morphologie. Diese Ähnlichkeit spricht für einen gemeinsamen Ursprung in Sternentstehung. Innerhalb von 8 pc um den AGN ereignet sich seit 100 Myr starke Sternentstehung, die momentan für 1.4% der Leuchtkraft der Galaxie verantwortlich ist. Morphologie und Kinematik des Gases sind konsistent mit einer rotierenden opaken dicken Scheibe; diese Scheibe interpretieren wir als Analogon zu einem molekularen/staubigen Torus. Da sich Gas und Sterne im selben Gebiet befinden, muss dieser Torus Sterne bilden. Aus den Grenzen für die Extinktion von Sternlicht ergibt sich, dass es sich um ein klumpiges Medium handelt.

In Falle von NGC1068 konzentriert sich die Analyse auf die Eigenschaften des molekularen Gases im zentralen Parsec des AGN. Bei einer Winkelauflösung von $0.075''$ zeigt eine Karte der Emission von molekularem Wasserstoff zwei auffällige lineare Strukturen, die von Norden nach Süden auf den AGN zeigen. Die Kinematik des Gases in diesen Strukturen ist von nicht-zirkularer Bewegung dominiert; dies deutet auf das Einströmen von Gas auf hochelliptischen oder parabolischen Bahnen hin, deren Lage mit der galaktischen Ebene übereinstimmt. Dies lässt sich als Gaszufuhr in die Zentralregion verstehen. Eine der einfallenden Wolken befindet sich direkt vor dem Schwarzen Loch. Diese durch Gezeitenkräfte zerrissene Wolke bildet eine amorphe, klumpige molekulare/staubige Struktur die den AGN verdeckt.

Die geschilderten Beobachtungen machen die Vorteile von abbildender Nahinfrarot-Spektroskopie bei der Untersuchung der Verteilung und Kinematik von Gas und Sternen im zentralen Parsec von AGN deutlich.

Dieses Forschungsprogramm könnte durch Verwendung des interferometrischen Fokus des Large Binocular Telescope (LBT) eine neue Qualität im Sinne von Empfindlichkeit und räumlicher Auflösung erreichen. Die Halbwertsbreite (FWHM) einer interferometrisch abgebildeten Punktquelle wird etwa 16 mas bei $2.0\ \mu\text{m}$ betragen, weit jenseits der Fähigkeiten bisheriger 8–10m Teleskope. Das MPE und die Universität Köln haben im Rahmen des Projekts SERPIL/LIINUS verschiedene Ausführungen eines abbildenden Spektrometers für den interferometrischen Fokus des LBT untersucht. Gegenstand des instrumentellen Teils dieser Arbeit ist die Einkopplung von Licht aus einer doppelten Pupille in optische Fasern in verschiedenen Konfigurationen. Dieses Verfahren ist entscheidend für den Entwurf eines Spektrographen der auf einer Lenslet+Faser Integralfeldeinheit (IFU) beruht. Speziell für LBT kommen zwei Konzepte für ein derartiges Instrument in Frage: Einerseits anamorphe Vergrößerung in Verbindung mit quadratischen Mikrolinsen, die an Einzel- oder wenige-Moden-Fasern gekoppelt werden; andererseits rechteckige Mikrolinsen, die an wenige-Moden-Fasern mit mehr als drei übertragenen Moden gekoppelt werden.

Abstract

The high energy output of an Active Galactic Nucleus (AGN) is due to the accretion of material onto a supermassive black hole (SMBH) and implies the presence of a gas reservoir close to the AGN. Furthermore, according to the Unified Model of AGN, the gas also plays an important role in the aspect-angle obscuration of the nucleus produced by a molecular/dusty torus. In the case of Type 2 AGN the line-of-sight intercepts the torus (edge-on) and obscures the broad emission lines. In Type 1 the torus is orientated such that the line-of-sight is perpendicular to the plane of the torus (pole-on) allowing observations of the broad emission lines close to the SMBH. In addition to the gas distribution and dynamics in the nucleus, the coexistence of an AGN and a starburst region on scales of a few parsecs around the centers of active galaxies, is one of the key issues to investigate in the field of AGN research. Increasing evidence that starbursts do occur in the vicinity of AGN has revived the importance of disentangling how AGN and star formation activity impact on each other.

The scientific goal of this thesis is to carefully explore, at the highest available spatial resolution, the nature of the nuclear star formation and the molecular gas in a selected number of nearby AGN by means of adaptive optics assisted near-infrared integral field spectroscopy with the SINFONI instrument at the Very Large Telescope. The two studied targets are the most prominent and brightest Seyfert 2 galaxies: The Circinus galaxy and NGC1068.

In Circinus, the similarity of the morphologies of the H_2 1-0S(1) and $Br\gamma$ emission lines to the stellar continuum and also their kinematics, suggest a common origin in star formation. Within 8 pc of the AGN there has been a recent starburst in the last 100Myr, which currently accounts for 1.4% of the galaxy's bolometric luminosity. The morphology and kinematics of the gas are consistent with those of a rotating opaque thick disk, which we associate with the molecular/dusty torus. Since the scales on which the gas and stars exist are similar, this torus must be forming stars, and due to the limits on extinction to the stars, it must be a clumpy medium rather than an uniform structure.

In NGC1068, the analysis was focused to the properties of the molecular gas in the central parsec of the AGN. At a resolution of $0.075''$, the flux map of molecular hydrogen emission around the nucleus reveals two prominent linear structures leading to the AGN from the north and south. The kinematics of the gas in these features are dominated by non-circular motions and indicate that material is streaming towards the nucleus on highly elliptical or parabolic trajectories whose orientations are compatible with that of the disk plane of the galaxy. This is interpreted as evidence for fueling of gas to the central region. One of the infalling clouds lies directly in front of the central engine. This is understood as a tidally disrupted streamer that forms the optically thick outerpart of an amorphous clumpy molecular/dusty structure which contributes to the nuclear obscuration.

These observations show the advantages of near-IR integral-field spectroscopy in studying the distribution and kinematics of the stars and gas in the central parsec of AGN.

This science program could be brought to a next level in terms of increased sensitivity and spatial resolution by performing similar observations at the interferometric focus of the Large Binocular Telescope (LBT). The FWHM of the interferometric beam at $2.0\mu\text{m}$ will be ~ 16 mas, offering unique imaging and spectroscopic capabilities well beyond the angular resolution of current 8–10m telescopes. A design study which explores the several technical solutions for the design of an interferometric integral-field spectrometer for the LBT has been undertaken by the Max Planck Institute for extraterrestrial Physics and the University of Cologne under the name of SERPIL/LIINUS. The goal of the instrumental part of the thesis is to investigate the physics of coupling light from a double pupil to optical fibers in several configurations. This is crucial for the design of the spectrograph based on a lenslet+fibers integral field unit (IFU). Particularly for the LBT, two options are viable for an instrument with a lenslet+fibers IFU: Anamorphic magnification together with square microlenses coupled to single- or few-mode fibers, and rectangular microlenses coupled to few-mode fibers with more than 3 propagating modes.

Publications

Chapters 2, 3 and 5 are all almost exact reproductions of papers published in or to be submitted to refereed journals:

- Müller Sánchez, F., Davies, R. I., Eisenhauer, F., Tacconi, L.J., Genzel, R., & Sternberg, A. 2006, *A&A*, 454, 481
- Müller Sánchez, F., Davies, R. I., Genzel, R., Tacconi, L.J., Eisenhauer, F., Hicks, E., Friedrich, S., & Sternberg, A. 2008a, *ApJ*, submitted
- Müller Sánchez, F., Eisenhauer, F., Genzel, R., Gál, C., Krabbe, A., & Herbst, T. 2008c, *ApJS*, to be submitted

In addition, the following publications partially resulted from work done in this thesis:

- Davies, R. I., Müller Sánchez, F., Genzel, R., Tacconi, L. J., Hicks, E., Friedrich, S., & Sternberg, A. 2007, *ApJ*, 671, 1388
- Müller Sánchez, F., Davies, R. I., Genzel, R., Tacconi, L. J., Hicks, E., & Friedrich, S. 2007, to appear in Proceedings of the conference “The nuclear region, host galaxy and environment of AGN”, Mexico, April 2007
- Müller Sánchez, F., Davies, R. I., Eisenhauer, F., Tacconi, L. J., & Genzel, R. 2006, *New Astronomy Reviews*, 50, 439
- Davies, R.I., Genzel, R., Tacconi, L., Müller Sánchez, F., and Sternberg, A. 2006, in Proceedings of the conference “The Central Engine of Active Galactic Nuclei”, ed. L. C. Ho and J.-M. Wang (San Francisco: ASP), China, September 2006
- Davies, R. I., Genzel, R., Tacconi, L., Müller Sánchez, F., and Sternberg, A. 2006, in Proceedings of the conference “Mapping the Galaxy and Nearby galaxies”, Japan, June 2006
- Gál, C., Müller Sánchez, F., Krabbe, A., Eisenhauer, F., Iserlohe, C., Haug, M., & Herbst, T. M. 2006, in *Ground-based and Airborne Instrumentation for Astronomy*, Edited by McLean, Ian S., Iye, Masanori, *Proc. SPIE*, 6269, 62693O

Contents

Zusammenfassung	i
Abstract	iii
Publications	v
List of Tables	xi
List of Figures	xiii
I SINFONI observations of Nearby AGN	1
1 Introduction to the nearby AGN project	3
1.1 The AGN phenomenon	4
1.1.1 The nearby AGN: Seyfert Galaxies	6
1.2 Scientific Rationale	8
1.2.1 Nuclear Star Formation	8
1.2.2 The Molecular/Dusty Torus	9
1.2.3 The central black hole mass	10
1.3 Integral-Field Spectroscopy	11
1.3.1 The SINFONI Instrument	14
1.4 The nearby AGN SINFONI sample	15
2 The Circinus Galaxy	19
2.1 Introduction	20
2.2 Observations and data reduction	21
2.3 Spectroscopic features and spatial resolution	22
2.3.1 Spatial Resolution	22
2.3.2 Distribution of emission and absorption features	25
2.4 Nuclear dust emission	25
2.5 Nuclear star formation	29
2.6 Gas kinematics and mass	36

2.7	The star forming torus	38
2.8	Coronal lines	40
2.9	Conclusions	44
3	Gas streamers in the nucleus of NGC1068	47
3.1	Introduction	48
3.2	Observations	49
3.3	Physical properties of the molecular gas	50
3.3.1	Molecular gas morphology	50
3.3.2	Kinematic evidence for inflow	55
3.3.2.1	Detection of non-circular motions around the nucleus	55
3.3.2.2	Quantitative modelling	59
3.3.2.3	Gas is on highly elliptical/parabolic orbits	61
3.3.2.4	Streamers flow inwards in the plane of the galaxy . .	65
3.3.3	Mass of the infalling molecular material	67
3.3.4	Mass accretion rate	70
3.3.5	Obscuration by inflowing gas	70
3.3.6	Connection of the streamers with the circumnuclear environment	71
3.4	Conclusions	74
 II Design of an interferometric integral-field spectrograph for the LBT		77
4	Introduction to the design study SERPIL/LIINUS	79
4.1	The Large Binocular telescope (LBT)	80
4.2	LINC/NIRVANA	82
4.3	Scientific Justification	83
4.3.1	Nearby Active Galactic Nuclei	85
4.3.2	Stellar content and supermassive black holes in nearby galaxies: the case of M31	86
4.3.3	Galactic Center	87
4.3.4	Extrasolar Planets	87
4.4	Top level requirements	88
4.5	The SERPIL/LIINUS project	88
4.5.1	Technical options for SERPIL/LIINUS	89
4.5.2	Key components of SERPIL/LIINUS	91
4.5.2.1	Preliminary optical design using microlenses	91
4.5.3	Status of the project	93
5	Coupling light into optical fibers	95
5.1	Introduction	96
5.2	Optical Fundamentals	98

5.2.1	Imaging Interferometry on the LBT	98
5.2.2	Theory of fibers	103
5.2.3	Coupling efficiency	104
5.3	Results	105
5.3.1	Description of the simulations	105
5.3.2	Focal-Plane coupling	106
5.3.2.1	Single-dish telescope	106
5.3.2.2	LBT's double pupil	106
5.3.3	Pupil-Plane coupling	110
5.3.3.1	Single-dish telescope	110
5.3.3.2	LBT's double pupil	115
5.4	Implications for the LBT	120
5.4.1	The case of Anamorphic magnification	120
5.4.2	The SERPIL/LIINUS spectrograph	124
5.4.3	Background Noise considerations	130
5.5	Conclusions	130
6	Conclusions and Outlook	133
6.1	Outlook	135
	Bibliography	139

List of Tables

1.1	The Nearby AGN SINFONI Sample	17
2.1	Line fluxes in Circinus	22
2.2	Sample of luminous and ultraluminous galaxies	36
2.3	Properties of the coronal lines	43
3.1	Orbital parameters of the southern gas streamers	63
3.2	Orbital parameters of the northern gas streamers	64
4.1	Important parameters of LINC/NIRVANA	83
4.2	SERPIL/LIINUS AGN sample	86
5.1	First ten linearly polarised modes of a step index fiber	105

List of Figures

1.1	Schematic diagram of the unified scheme for AGN	5
1.2	NGC1068 spectra	7
1.3	The $M_{BH} - M_{B,bulge}$ and $M_{BH} - \sigma_*$ relations	12
1.4	Schematic of IFU types	13
1.5	Inside view of SPIFFI	16
2.1	Nuclear spectrum of Circinus	24
2.2	Intensity images of Circinus	26
2.3	Radial profiles of the continuum in Circinus	28
2.4	Radial profiles of the emission lines and the stars in Circinus	29
2.5	Star clusters simulations	31
2.6	Evolutionary models of the stars	33
2.7	Velocity maps of the H ₂ 1–0S(1) and Br γ lines	35
2.8	Nuclear spectrum around CaVIII	38
2.9	Comparison of coronal line profiles in velocity space	40
2.10	Radial profiles of the coronal lines	42
3.1	SINFONI H ₂ 1–0S(1) flux map of the central 4'' \times 4'' of NGC1068	52
3.2	SINFONI H ₂ 1–0S(1) flux map of the central 0.8'' \times 0.8'' of NGC1068	53
3.3	Integrated spectrum of the nucleus of NGC1068 in the wavelength range between 1.5 and 2.35 μ m	54
3.4	Contour plot of the 12.5 μ m deconvolved image overlaid on the SINFONI H ₂ 1–0S(1) flux maps	56
3.5	Morphology of the H ₂ 1–0S(1) emission with the 5 GHz radio continuum overplotted in contours	57
3.6	Velocity and dispersion maps of the molecular gas in the central $\pm 0.4''$ of NGC1068	58
3.7	Trajectories of the northern and southern streamers plotted over the intensity H ₂ map	62
3.8	Line-of-sight velocities (v_z) of the streamers	66
3.9	Complete trajectories of the gas streamers plotted over the large scale H ₂ intensity map	72
4.1	The Large Binocular Telescope	81

4.2	The LINC-NIRVANA optical path	84
4.3	Technical solutions for SERPIL/LIINUS	89
4.4	Example of a TIGER-type integral field spectrograph based on a microlens array	92
5.1	Instrument concept of a Lenslet+Fibers integral-field spectrograph . .	97
5.2	Geometry of the Fresnel-Kirchoff equation for a double pupil configuration similar to the LBT.	99
5.3	Point Spread Function of the interferometric configuration of the LBT	102
5.4	Coupling efficiency versus focal ratio. Case study: LBT focal plane coupling	108
5.5	Maximum coupling efficiency versus normalized frequency (V). Case study: LBT focal plane coupling	109
5.6	First 12 modes of a multi-mode fiber	111
5.7	Coupling efficiency versus wavelength. Case study: LBT focal plane coupling	112
5.8	Maximum coupling efficiency versus microlens size. Case study: Single dish pupil plane coupling	114
5.9	Maximum coupling efficiency versus normalized frequency for three different microlens sizes. Case study: Single dish pupil plane coupling	116
5.10	Coupling efficiency versus wavelength. Case study: Single dish pupil plane coupling	117
5.11	PSF of the LBT filtered by a rectangular microlens	118
5.12	Micropupil of the LBT PSF filtered by a rectangular microlens	119
5.13	Maximum coupling efficiency versus microlens size for four different types of fibers. Case study: LBT pupil plane coupling	121
5.14	Maximum coupling efficiency versus normalized frequency for three different microlens sizes. Case study: LBT pupil plane coupling . . .	122
5.15	Coupling efficiency versus wavelength. Case study: LBT pupil plane coupling	123
5.16	Anamorphic double pupil and its correspondent PSF	125
5.17	Micropupil of the anamorphic LBT PSF filtered by a square microlens	126
5.18	Space available inside LINC	128
5.19	Required optical path to re-image LINC's focal plane at the upper part of the cryostat	129

Part I

**SINFONI observations of Nearby
AGN**

Chapter 1

Introduction to the nearby AGN project

Active Galactic Nuclei (AGN) are the most luminous sources of electromagnetic radiation in the universe, and as such they represent one of the most interesting areas of research in astronomy. The physical structure of AGN is a topic of great importance for the understanding of galactic structure and evolution. Due to their nature, high spatial resolution observations are needed to study them in detail. So far, our knowledge of AGN remains limited as most of their physical properties are among the main debated topics in astrophysics.

In the first part of this thesis, we analyse a sample of nearby sources that are known to be representative of the AGN phenomenon. Integral-field spectroscopic observations of these galaxies near the diffraction limit of an 8m-telescope were performed in order to study their near-infrared properties. Our main interests lie on the distribution and kinematics of the stars and the molecular gas surrounding the nucleus.

This part of the thesis is organised as follows: Chapter 1 provides a general overview of our current understanding of the AGN paradigm. As we concentrate on the nuclear regions of active galaxies, emphasis is given to Seyfert galaxies, which due to their proximity, form our sample of nearby AGN. After a few words about the Scientific Rationale of the thesis, we describe the employed observational technique together with the SINFONI instrument. At the end of this chapter the nearby AGN sample is presented. The actual work of this part of the thesis is the detailed analysis of the SINFONI observations of the Circinus galaxy and NGC1068 presented in chapter 2 and 3 respectively. The conclusions and future work prospects are discussed in chapter 6.

1.1 The AGN phenomenon

The nuclei of certain galaxies produce a great amount of energy, in the range of 10^7 to $10^{15} L_{\odot}$, on very small spatial scales. These objects are known as “Active Galactic Nuclei” (AGN). An AGN can contribute more to the total luminosity of its host galaxy than the entire stellar component ($\approx 10^{11} L_{\odot}$). These galaxies possess powerful non-stellar central engines which produce radiation over the entire electromagnetic spectrum. The most likely source of this central power is the accretion of matter onto a supermassive black hole ($> 10^6 M_{\odot}$) (Rees 1984). In addition to high luminosities from a small area due to non-stellar processes, AGN display many other characteristics. In contrast to normal galaxies, AGN commonly show bright highly ionized emission lines which at optical and ultraviolet (UV) wavelengths can contribute several percent to the total continuum flux and show a FWHM of up to 10^3 km s^{-1} . AGN also show high degrees of variability in their nuclei usually at X-ray, UV, and optical wavelengths. This variability can be as large as an order of magnitude or greater on scales ranging from seconds to decades. Active galactic nuclei also show high degrees of polarized emission, a signature of non-thermal emission processes.

AGN can be classified into several subcategories, according to their type of radiation, luminosity, emission line properties, variability, and even circumstances involving initial discovery. These varieties of AGN frequently overlap and have arbitrary classification schemes. For a review of the AGN phenomenon see e.g. Lawrence 1987. The most accepted classification scheme, describing the diversity of AGN by the same physical model, is the “Unified Scheme of AGN” proposed by Antonucci (1993).

In the Unified Model, all AGN have the same basic structure but the differences we see depend on the angle of the system to the observer. This basic structure starts from the innermost region where an accretion disk dumps matter into a supermassive black hole (SMBH) of $\sim 10^6 M_{\odot}$ for Seyfert galaxies and up to $10^{11} M_{\odot}$ for distant powerful quasars. As the material spirals in, collimated jets of heated matter are ejected at velocities close to the speed of light and extend from 0.01 to 10^6 pc . The accretion disk extends from the marginally stable orbit up to thousands of Schwarzschild radii. The accretion process releases energy in the form of high-energy photons which ionize material orbiting close to the SMBH ($\sim 0.01 - 1 \text{ pc}$), producing the Doppler-broadened emission lines characteristic of the “broad line region” (BLR). The term comes from the broad spectral lines emitted from the dense clouds that reside in this region. Moving outward further to a scale of about 1-10 pc, there exists UV-opaque gas and dust that surrounds the AGN and is referred to as the “molecular/dusty torus”. Just outside the torus and along the poles of the SMBH, at distances ranging from 10-1000 pc, is a thin layer of lower density gas which is known as the “narrow line region” (NLR). In a virial sense, the greater distance from the SMBH results in a lower velocity, leading to the narrow widths of the emission lines in this region. In addition, at some point in the NLR the “forbidden” lines are produced which are generally suppressed in the higher density gases. Both the BLR and NLR are excited either by

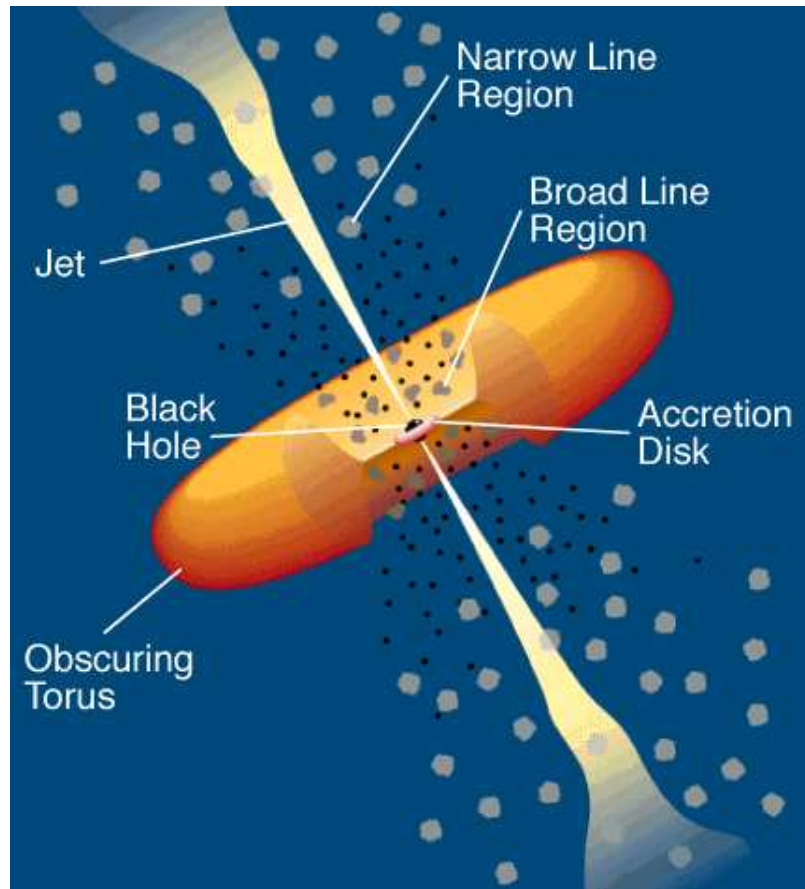


Figure 1.1: Schematic diagram of the unified scheme for AGN from Urry & Padovani (1995).

photoionization from the UV continuum of the central engine (Koski 1978; Ferland & Netzer 1983; Stasinska 1984), by shock excitation from jets (Sutherland et al. 1993; Dopita & Sutherland 1995), or by a combination of the two. Figure 1.1 illustrates the Unified Model, according to which the classification of an Active Galactic Nucleus depends on the inclination of its rotation axis to the line of sight. If the line of sight to an AGN is along the rotation axis of the system, both the BLR and NLR will be directly observed and hence it will be classified as Type 1 AGN. If the line of sight is perpendicular to the axis of the system, the torus will obscure the central engine and a Type 2 AGN will be recognised. In the case of radio loud AGN, observations along the jet axis will result in enhanced radio emission and strong variability resulting in a BL Lac or “blazar” classification.

Strong evidence supporting the unification scheme of AGN came through spectropolarimetry of the Seyfert galaxy NGC1068 by Antonucci & Miller (1985). They detected broad emission lines in polarized flux in what was previously classified as

a Type 2 Seyfert (see Figure 1.2). Thus they concluded that NGC1068 possess a BLR, similar to those detected in Type 1 but hidden from our direct view, revealed in polarized flux due to scattering from clouds of dust/electrons that scatter broad emission lines into our line of sight. Nowadays, many more such hidden BLR are known and they seem to be present in at least 30% of all Seyfert 2 galaxies (Tran et al. 2001).

1.1.1 The nearby AGN: Seyfert Galaxies

In this thesis, we concentrate on the nuclear regions of active galaxies. Among the entire variety of AGN, Seyfert Galaxies are the closest to us (3-100 Mpc) and, therefore, the best targets for integral-field spectroscopic observations with the SINFONI instrument (see Section 1.3), capable of revealing the distribution and kinematics of the stars and gas surrounding the nucleus. In Seyfert galaxies, the nuclear activity is powered by SMBHs of $10^6 - 10^{7.5} M_{\odot}$ producing AGN luminosities of the same order as the stars in their host galaxies (roughly $10^{11} L_{\odot}$). This is in contrast to quasars, where the nucleus encloses a SMBH of $10^{7.5} - 10^{9.5} M_{\odot}$ outshining the stellar content by a factor of approximately 100. Seyfert galaxies are mostly spiral galaxies presenting enhanced central luminosity, or alternatively, they are normal galaxies with an enormous amount of material feeding their central black hole. About 3% to 5% of all galaxies are Seyfert galaxies (Maiolino et al. 1995).

These nearby AGN were discovered in 1943 by Carl Seyfert while examining six galaxies selected from the archives of the redshift surveys of the Mt. Wilson Observatory. These galaxies showed bright nuclei with respect to their disk component. Also, compared to normal galaxies, these galaxies revealed broad emission lines at visible wavelengths (Seyfert 1943). They became known as Seyfert galaxies and formed the basis for an entire class of active galaxies. As spectroscopic techniques improved, Khachikian & Weedman (1974) subdivided Seyferts into two categories. In the first group, there was a marked difference between the widths of the permitted (FWHM in the range $10^3 - 10^4 \text{ km s}^{-1}$) and forbidden lines (FWHM $\sim 10^3 \text{ km s}^{-1}$), whereas in the second group both permitted and forbidden emission lines had the same width $\sim 10^3 \text{ km s}^{-1}$. Therefore Seyferts were the first class of AGN to be divided into Type 1 (showing broad and narrow lines) and Type 2 (showing only narrow line emission). Subsequent researchers have also sub-divided Seyferts into intermediate classes such as Types 1.2, 1.5, 1.8, and 1.9 based on the increasing strength of narrow lines with respect to the broad lines (Maiolino et al. 1995; Osterbrock 1989). Well-known examples of Seyfert 2 galaxies are NGC1068 and the Circinus galaxy, while NGC3227 and NGC3783 are famous Type 1 Seyferts. These four belong to the nearby AGN SINFONI sample (see Section 1.4).

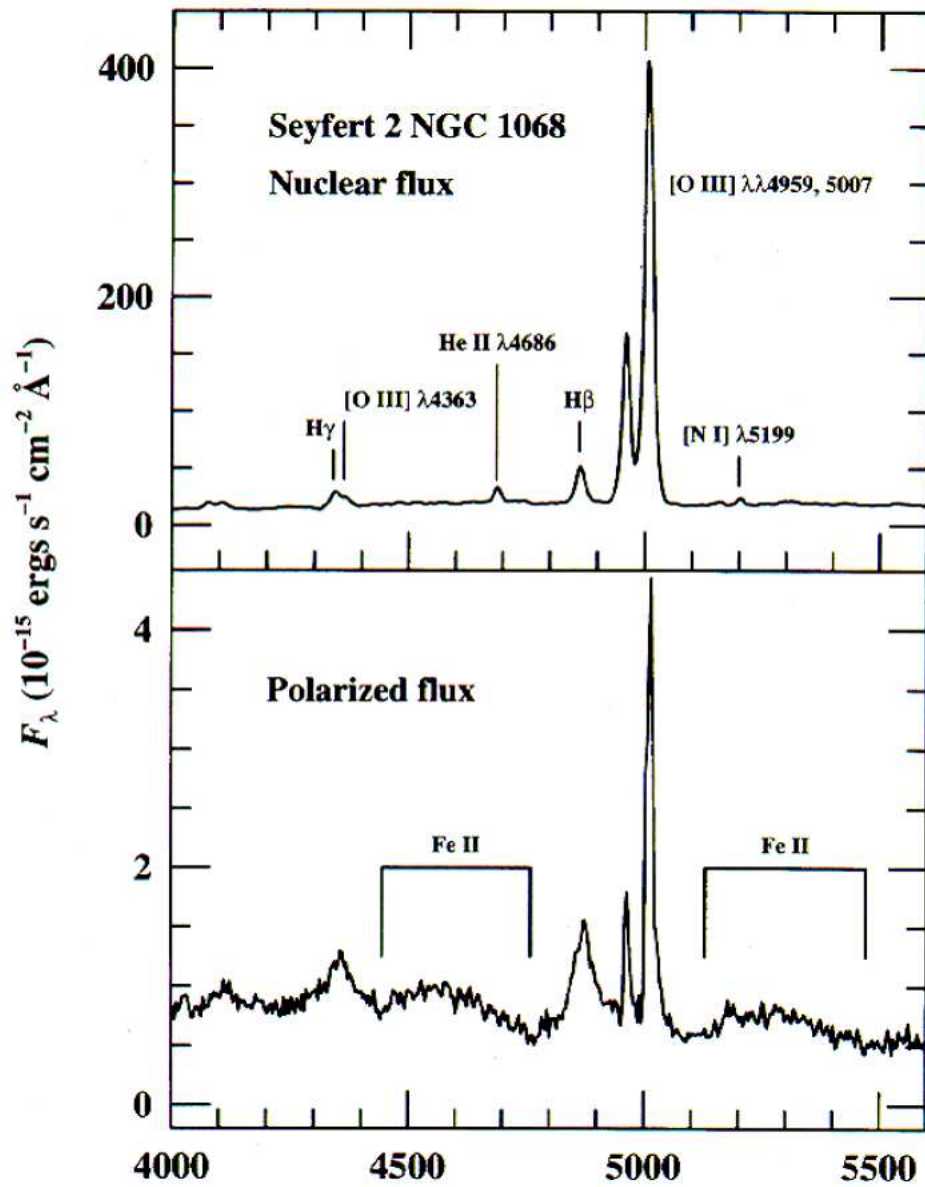


Figure 1.2: NGC1068 spectra. Notice the broad $\text{H}\beta$ emission which becomes apparent only in polarized light. (Miller et al. 1991; Robson 1996).

1.2 Scientific Rationale

This thesis grew out of the MPE nearby AGN research program, which is based mainly on observations obtained by the adaptive optics assisted near-infrared integral-field spectrograph SINFONI at the Very Large Telescope (VLT). The scientific goals of the thesis and the program are to:

- determine the extent and history of circum-nuclear star formation, and its relation to the AGN;
- measure the properties of the molecular gas, and understand its relation to the putative torus;
- derive black hole masses from spatially resolved stellar kinematics

In order to directly investigate these three issues, sensitive high resolution imaging and spectroscopy of a sample of Seyfert galaxies are required. For the observations presented in this thesis, the diffraction limited light from an 8m telescope, after correction by an adaptive optics system, was used, reaching spatial resolutions as small as $0.075''$. As it will be seen in the rest of this section and in Section 1.3, the SINFONI instrument is essential for accomplishing the three scientific goals of the thesis.

1.2.1 Nuclear Star Formation

The coexistence of an active galactic nucleus and a starburst region on scales of a few parsecs around the nucleus is one of the key issues to be investigated in state-of-the-art studies of AGN. Increasing evidence that starbursts do occur in the vicinity of AGN has revived the importance of disentangling how AGN and star formation activity impact on each other. Several studies have probed that at distances of a few hundred parsecs from the nucleus, star formation is an important process in all types of AGN (Sarzi et al. 2007; Asari et al. 2007; González Delgado et al. 2001; Cid Fernandes et al. 2004; Gu et al. 2001; Storchi-Bergmann et al. 2001). The overall conclusion of these studies - biased towards Seyfert 2 galaxies - is that in 30-50% cases the AGN is associated with young star formation (age less than a few 100 Myr). However, such star formation activity has not been able to elucidate any correlation between AGN and star formation simply because it lies so far from the AGN that it cannot influence it, or be strongly influenced by it (Heckman et al. 1997). Thus, any presumed causal connection between AGN and starburst might occur on relatively small spatial scales and short timescales (Knapen et al. 2004). In the sense that AGN are effectively accreting SMBHs, the Galactic Center is perhaps the clearest case that episodic star formation happens effectively and perhaps frequently in the sphere of influence of a SMBH (Genzel et al. 2003; Paumard et al. 2006).

Near-infrared adaptive optics assisted integral-field spectroscopy is required to reveal any relationship between nuclear star formation and nuclear activity in both types of Seyfert galaxies. The near-infrared is ideally suited for this purpose as the radiation of several star types is strong at these wavelengths, and the extinction is a factor of 10 smaller than at optical wavelengths. It would certainly help to determine whether there is evidence for star formation in AGN from radii of 100 pc down to 5 pc; and if so, to constrain its star formation history. This information could eventually reveal how the nuclear starburst and AGN are mutually influencing each other.

Results on this topic will be discussed in Chapter 2 in which the properties of the nuclear star formation in the Circinus galaxy are presented.

1.2.2 The Molecular/Dusty Torus

A fundamental prediction of the unified model of AGN is the existence of dense molecular gas and dust ($T \sim 100 - 1500$ K) in the form of a geometrically thick ($h_z \sim r$) and optically thick torus responsible for the aspect-angle and wavelength-dependent UV (and perhaps X-ray) obscuration of the nucleus. So far, most of its properties are poorly understood. As previous attempts to obtain a clear image of it have failed, its characteristics have been inferred only indirectly, leading to a controversial debate about its extent and physical properties.

Theoretical models have been developed to explain the physical properties of dusty tori in AGN. Because previously no observational means were available to resolve the dust distribution, the very first radiative transfer calculations of dust re-emission from the tori were aimed to reproduce the overall Spectral Energy Distribution (SED) of Seyfert galaxies and quasars. Based on a homogeneous dust distribution and different assumptions for the size and geometry of the torus - compact torus (Pier & Krolik 1992) or extended flat disk models (Granato et al. 1994; Efstathiou & Rowan-Robinson 1995) - these models led to confusion about the physical size of tori in AGN. The new more realistic theoretical models of tori, assuming a non-homogeneous distribution of gas and dust (Nenkova et al. 2002; Schartmann et al. 2005; Fritz et al. 2006; Hönig et al. 2006), alleviate to some extent the size crisis, favouring the compact torus scenario.

Observational evidences of the existence of the torus in a Seyfert galaxy have been reported mainly for the prototype Seyfert 2 galaxy NGC1068 at mid- and near-infrared wavelengths. The first evidence for a torus comes from the bright nuclear mid-IR source (Bock et al. 2000; Tomono et al. 2001) correlated with emission from ionized gas extended in a nearly conical structure oriented roughly northeast-southwest (Cecil et al. 2002). Moreover, the $9.7\mu\text{m}$ silicate feature is seen in absorption as predicted by the unified model for a Type 2 object (Jaffe et al. 2004, Rhee & Larkin 2006; Mason et al. 2006). Additional evidence in the mid-IR comes from the $8 - 13\mu\text{m}$ MIDI/VLTI interferometric observations of NGC1068 (Jaffe et al. 2004). They interpreted their data with a two-component model consisting of

a hot (800 K) dust structure with extension < 1 pc and a warm (320 K) structure of 3.4×2.1 pc. They identified the hot component as the inner wall of the dusty torus. However, more recently, Jaffe et al. (2007) have analyzed new interferometric mid-IR observations of NGC1068 and found that the fitted Gaussian components to the (u, v) plane of the central $10 \mu\text{m}$ source resemble a disk similar to the H_2O masers (Greenhill et al. 1996). Both, the dust and H_2O maser disks, appear to be oriented neither perpendicular to nor aligned with the radio jet.

In the near-IR, several high-resolution observations of NGC 1068 (Thatte et al. 1997; Weigelt et al. 2004; Prieto et al. 2004) show a compact central core of 1.3×2.8 pc in the K -band, which is interpreted as dust close to the sublimation radius. The high resolution VINCI/VLTI interferometric observations of Wittkowski et al. (2004) show that a K -band flux of >50 mJy originates from scales clearly smaller than about 5 mas or 0.4 pc and another part of the flux from larger scales. They interpreted this small-scale emission as a substructure of the dusty torus, as for instance part of a clumpy inner cavity or distinct clumps forming the torus, or as direct emission from the central accretion flow viewed through only moderate extinction in the K -band.

Additionally, several authors have reported radiative transfer models with application to NGC1068. Hönicg et al. (2006) employed a three-dimensional clumpy tori model, while Schartmann et al. (2005) and Fritz et al. (2006) used a physically motivated geometry and dust distribution. All of them were able to reproduce the SED of the active nucleus in the near- and mid-infrared. However, there are some discrepancies in the value of the external radius R_{out} of the torus, which goes from 17 pc in the models from Fritz et al. (2006) or ~ 20 pc in Hönicg et al. (2006) to 72 pc reported by Schartmann et al. (2005).

The analysis of the warm molecular gas traced by the $2.122 \mu\text{m}$ H_2 roto-vibrational $\nu = 1-0\text{S}(1)$ emission line could not only expose the potential presence of a molecular/dusty torus in active nuclei, but also provide physical information about the system, such as fueling or feedback mechanisms. Detailed studies of the distribution and kinematics of such gas in the nuclear regions of galaxies can be achieved for the first time by means of near-IR integral-field spectroscopy. We have used SINFONI integral-field spectroscopic data of the nuclei of the Circinus galaxy and NGC1068, in order to analyze in detail the physical conditions of warm molecular gas in the central regions of active galaxies.

1.2.3 The central black hole mass

The third issue motivating this thesis is the determination of the mass of the central supermassive black hole (M_{BH}) from resolved nuclear stellar dynamics. The masses of black holes in nearby AGN are most commonly estimated by reverberation mapping (Onken et al. 2004), a technique that can be extended to higher redshift via additional scaling relations (Kaspi et al. 2000, 2005; Vestergaard 2002, 2004). Providing an independent measure of M_{BH} for reverberation masses would allow one to begin

to understand the geometry of the broad line region. In addition, estimates of M_{BH} are important in order to acquire a more precise knowledge of the behaviour of the correlations between M_{BH} with the mass of the bulge in which it resides, and with the bulge velocity dispersion - the $M_{BH} - \sigma_*$ relation - a cornerstone in the cosmological context of galaxy evolution and black hole growth (Ferrarese & Merritt 2000; Gebhardt et al. 2000b, Kormendy & Richstone 1995) (Figure 1.3). It is generally accepted that the $M_{BH} - \sigma_*$ relation should be valid for all spheroids irrespective of their nature (spiral, bulge, pseudo-bulge, elliptical or irregular) and the nature of the black hole (quiescent, active, supermassive, intermediate mass, stellar). However, almost without exception the black hole masses estimated from stellar kinematics have been derived only for nearby bulge dominated E/S0 galaxies (Tremaine et al. 2002; Marconi & Hunt 2003; Ferrarese & Ford 2005). The smaller bulges of spiral Seyfert galaxies imply lower M_{BH} , making it difficult to spatially resolve the stellar kinematics. In addition in these galaxies the glare of the AGN itself overshines the stellar luminosity adding another obstacle to the determination of the M_{BH} . Sensitive spectroscopy of the stellar and gas kinematics at high spatial resolution is required to probe within the radius of influence of the central black hole.

Integral-field spectroscopy is extremely well suited for studying the inner dynamics in nearby AGN and therefore the determination of the nuclear mass, since it helps to avoid ambiguous interpretations as from e.g. slit spectroscopy. The high spatial resolution and integral-field capability of SINFONI provides an ideal combination to do this.

1.3 The observational technique: Integral-Field Spectroscopy

Imaging and spectroscopy are the most exploited observational techniques in optical astronomy (in contrast to e.g. optical interferometry). This is because the nature of any astronomical field of view (FoV) is inherently of three dimensions: two dimensions for the sky plane and one spectral dimension. However, current detectors are of two-dimensional nature only. This has led to the construction of instruments which do only either imaging or spectroscopy, translating to an inefficient use of telescope time and more importantly, the impossibility of extracting the entire scientific information contained in the field. An Integral-Field Spectrograph (IFS) is able to pack the full three-dimensional data in a single exposure on a 2D-detector. Generally, an IFS consists of the pre-optics, which re-image the FoV focused by the telescope onto an Integral-Field Unit (IFU) whose function is to sample or slice the FoV that is then fed into a conventional spectrograph. The IFU is the most critical part of the spectrograph. Existing integral field spectrographs use one of the following three types of IFU: lenslet array, fiber bundles, and image slicers. They differ mainly in the geometrical arrangement of the spatial elements. Figure 1.4 shows the working

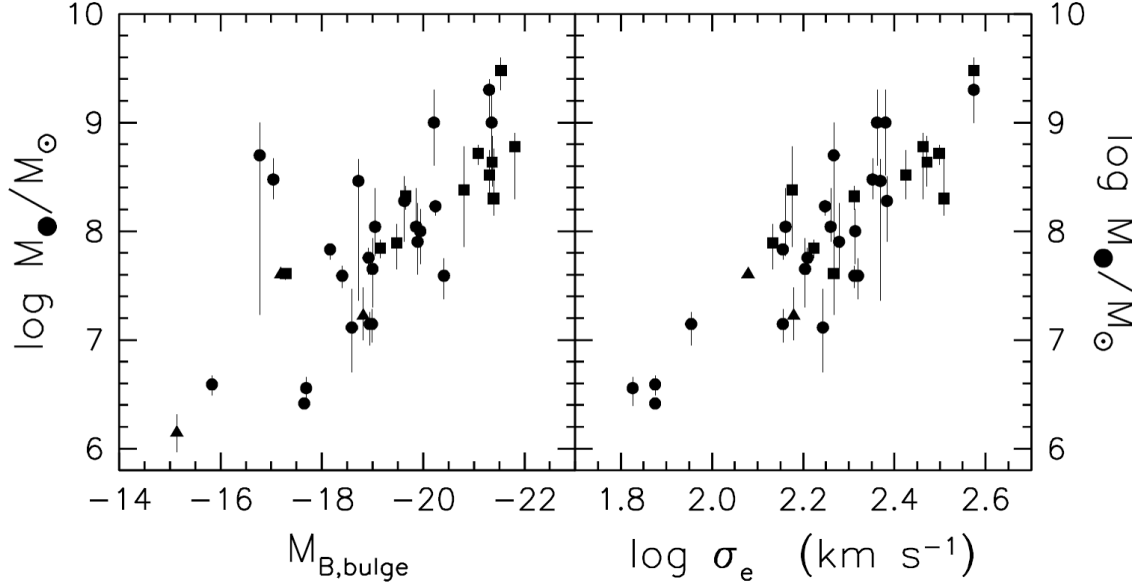


Figure 1.3: The $M_{BH}-M_{B,bulge}$ (left) and $M_{BH}-\sigma_*$ (right) relations for elliptical galaxies (circles), bulges (squares), and pseudo-bulges (triangles). From Kormendy & Gebhardt (2001).

principle of each type of IFU. Their characteristics, advantages and disadvantages compared to the others are the following:

- **Lenslet array:** Lenslet IFUs use an array of microlenses located at the focal plane of the telescope to sample the FoV. Each microlens creates a micropupil of typically $10 - 50\mu\text{m}$ diameter. All the micropupils are dispersed by the spectrograph producing a set of spectra that are then focused into the detector. It is this demagnification that saves space on the detector to store the spectral dimension. Such IFUs provide 100% covering efficiency of the image at the focal plane and the overall size of the optical system remains relatively compact. Present technologies offer square-, rectangular- or hexagonal-shaped lens arrays with a large variety of sizes and focal lengths. A disadvantage of this technique is the problematic accommodation of the spectra on the detector in order to maximize the packing efficiency. Examples of existing instruments accommodating microlens arrays are OSIRIS (Larkin et al. 2003), TIGER (Bacon et al. 1995) and SAURON (Bacon et al. 2001).
- **Fiber bundles:** Originally, fiber IFUs use optical fibers arranged in a close-packed bundle at the telescope focal plane and then reformatted into a pseudoslit, which is then fed into the spectrograph. This presents an advantage compared with lenslet IFUs in the sense that the arrangement of the spectral lines

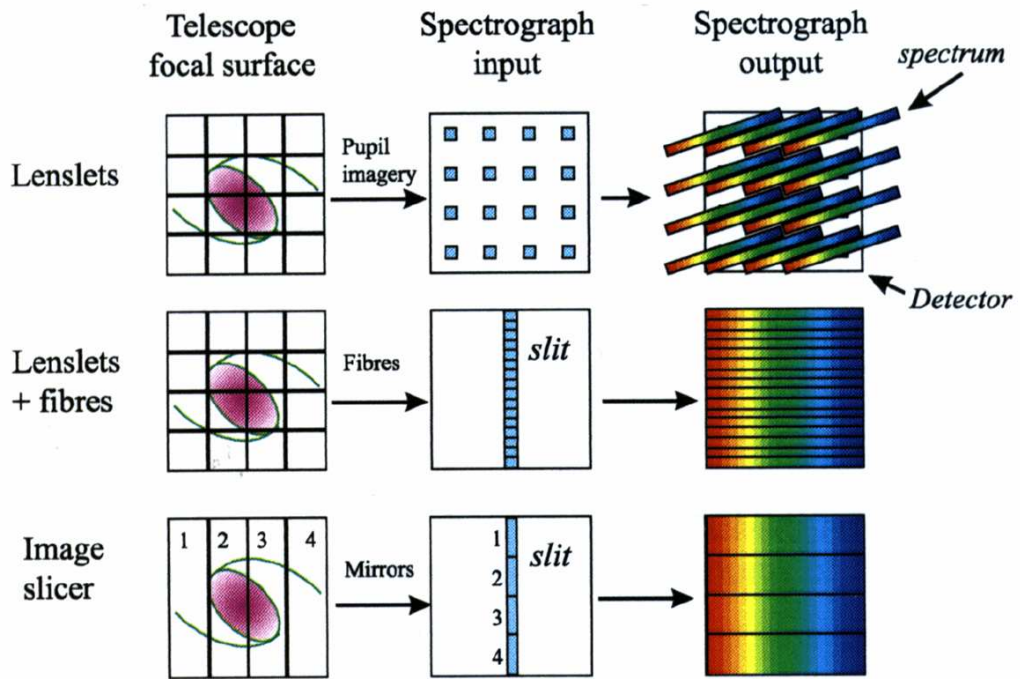


Figure 1.4: Schematic of IFU types (from Content 1997).

can be selected such that it fits one complete dimension of the detector. The major drawbacks of the fiber bundles are low covering efficiency at the focal plane, due to the fiber's cladding, and light losses due to Focal Ratio Degradation. However, these two problems can be overcome by adding microlenses in front of the fibers. Each microlens then forms an image of the telescope pupil (micropupil) at the entrance of each fiber in the bundle. At the output, a linear pseudoslit can be formed and fed to the spectrograph. Working examples are the SPIRAL at the 4 m Anglo-Australian telescope (Kenworthy et al 1998), GMOS for GEMINI north and south (Allington-Smith et al. 2002), and CIRPASS for GEMINI south (Parry et al. 2004).

- **Image slicer:** The slicer IFU uses mirrors in the focal plane to cut the field of view into a number of strips, which are then aligned one-by-one to form a long pseudo-slit which is fed into the spectrograph. The slicer is composed of two sets of mirrors: the first set slices the field in a number of strips and reflects them into different directions, while the second set rearranges the strips and aligns them into one continuous long strip. This solution is the most efficient in terms of spectral coverage and packing efficiency. The first working slicer IFU in the near infrared (H - and K -bands) was the 3D instrument built at MPE (Weitzel et al 1996). It was successfully used on a number of 4 m class telescopes. A very good example of a working slicer IFU is SINFONI at the VLT (Eisenhauer et al. 2003b). It was based on the original design of the slicer in 3D. Due to the length of the pseudo-slit, these IFUs normally occupy a lot of space in the cryostat. A variation of this principle which minimizes the size of the pseudoslit has been proposed by Content et al. (1997); the mirrors have curved surfaces to allow the pupil-relay mirrors to be reduced in size. These types of IFUs are known as advanced image slicers. Another possibility for an advanced image slicer is to place lenses in front of the second mirror which perform the reduction of the individual strips (Tecza et al. 2006).

1.3.1 The SINFONI Instrument

SINFONI comprises an adaptive optics facility (AO-Module), developed by ESO (Bonnet et al. 2004) and SPIFFI, a near-IR integral field spectrograph developed by MPE (Eisenhauer et al. 2003b). The AO-module consists of an optical relay from the telescopes Cassegrain focus to the SPIFFI entrance focal plane, which includes a deformable mirror conjugated to the telescope pupil. The curvature is updated on the 60 actuators at 420 Hz, with a closed-loop bandwidth of 30–60 Hz, to compensate for the aberrations produced by the turbulent atmosphere. Under good atmospheric conditions an adequate correction can be obtained with stars up to $R = 17$ mag. The SPIFFI integral field spectrometer records simultaneously the spectra of all image points in a two-dimensional field of view. The image scale of SPIFFI allows sampled imaging at the diffraction limit of the telescope ($0.0125'' \times 0.025''/\text{pix}$), seeing limited

observations ($0.125'' \times 0.25''/\text{pix}$) and an intermediate image scale ($0.05'' \times 0.1''/\text{pix}$), over a FOV of $0.8'' \times 0.8''$, $8'' \times 8''$, and $3.2'' \times 3.2''$ respectively. The spectral resolution of the spectrometer ranges between 2000 and 4000 for the three covered atmospheric bands: J ($1.1 - 1.4 \mu\text{m}$), H ($1.45 - 1.85 \mu\text{m}$) and K ($1.95 - 2.45 \mu\text{m}$). The instrument is fully cryogenic, and it is equipped with a Rockwell $2\text{k} \times 2\text{k}$ HAWAII-2RG array. Figure 1.5 shows an inside view of the main components of SPIFFI. The light enters from the top. The pre-optics with a filter wheel re-image the object plane from the AO module onto the image slicer, providing the three different image scales. The image slicer rearranges the two dimensional field onto a one-dimensional pseudo longslit. A grating wheel disperses the light and a short focal length camera then images the spectra on the detector. After some processing of the raw data, the outcome is a data cube with two spatial and one spectral dimensions.

1.4 The nearby AGN SINFONI sample

In order to study the characteristics of a class of galaxies such as Seyferts, ideally one would observe all members of that class. As this is impractical for many reasons, such studies rely on the analysis of a sample of sources that are chosen to be representative of the class as a whole. However, depending on the selection criteria for a sample, slight biases may be introduced. The nearby AGN SINFONI sample includes Type 1 and Type 2 Seyfert galaxies. Source selection was driven principally by technical considerations, being the primary criteria for selecting AGN that:

1. the nucleus should be bright enough for adaptive optics correction,
2. the galaxy should be close enough that small spatial scales can be resolved at the near-infrared diffraction limit of an 8-m telescope, and
3. the galaxies should be “well known” so that complementary data can be found in the literature

The resulting sample of 7 AGN is listed in Table 1.1. Thus, while the sample cannot be considered complete, it provides a representative cross-section of AGN. As an incomplete sample of Seyferts, a bias is introduced towards Type 1 objects. However, this bias can itself be considered a strength for the nuclear star formation studies, since it is exactly broad line AGN for which little is known about this issue, because as mentioned in Section 1.2.3, the glare of the AGN overshines any surrounding stellar light in the central arcsec.

This dissertation presents results of the observations of two AGN (the Circinus galaxy and NGC 1068). Remarkably but unintentionally, they are the only two Seyfert 2 galaxies in our sample. They were selected for detailed individual analysis due to their importance in the research field of AGN. It is important to point out that NGC3227 has already been studied by Davies et al. (2006), and the rest of the objects

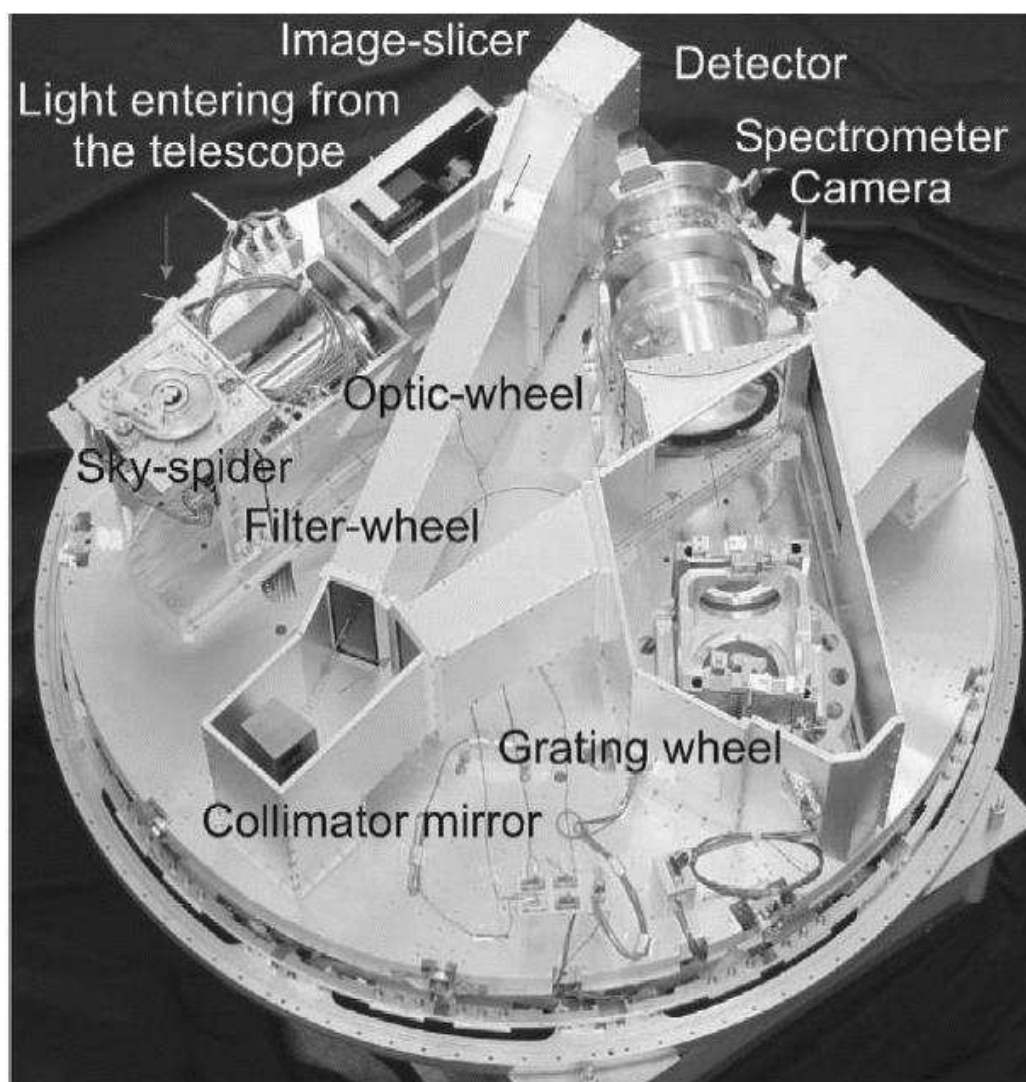


Figure 1.5: An inside view of SPIFFI (read text for the description of the elements).

Object	Classification	Distance (Mpc)	Observed Band	Resolution (")	Date of observation
Circinus	Sy2	4	K	0.22	July 2004
NGC1068	Sy2	14	H+K	0.075	October 2005
NGC3227	Sy1	17	K	0.085	December 2004
NGC1097	LINER, Sy1	18	H+K	0.245	October 2005
NGC2992	Sy1	33	K	0.3	March 2005
NGC3783	Sy1	42	H+K	0.17	March 2005
NGC7469	Sy1	66	K	0.15	July 2004

Table 1.1: The Nearby AGN SINFONI Sample.

in the sample are currently being analysed. On the other hand, following a different analysis strategy, Davies et al. (2007) have studied the issue of star formation in the nuclei of these 7 Seyfert galaxies (including the results from the Circinus galaxy and NGC1068) and two more for which we have already published adaptive optics near infrared spectra (Davies et al. 2004a, Davies et al. 2004b).

Chapter 2

Case study: The Circinus Galaxy

This chapter is an almost exact reproduction of the publication:

- “SINFONI adaptive optics integral-field spectroscopy of the Circinus Galaxy”
Müller Sánchez, F., Davies, R. I., Eisenhauer, F., Tacconi, L. J., Genzel, R., & Sternberg, A. 2006, *A&A*, 454, 481

2.1 Introduction

In the context of active galactic nuclei, star formation activity and the gas and stellar dynamics on scales of a few parsecs to a few tens of parsecs can be counted among the main debated issues. The unified model of active galaxies (see Lawrence 1987 for a review) assumes that the inner region of Seyfert 2 galaxies is comprised of a dense circumnuclear torus that hides the nucleus and the broad-line region from our line of sight at near-infrared and optical wavelengths. The size scales on which models predict the canonical torus vary from an inner edge at 1 pc out to several tens of parsecs (Pier & Krolik 1992; Nenkova et al. 2002; Schartmann et al. 2005). These crucial size scales are exactly those that can be resolved with SINFONI in the nearest AGN.

The Circinus galaxy, at a distance of 4.2 ± 0.8 Mpc (Freeman et al. 1977), is an ideal subject to study because of its proximity ($1'' = 20$ pc). It is a large, highly inclined ($i = 65^\circ$ Freeman et al. 1977), spiral galaxy that hosts both a typical Seyfert 2 nucleus and a circumnuclear starburst on scales of 100–200 pc (Maiolino et al. 1998). Evidence for an obscured Seyfert 1 nucleus is provided by the finding of a broad (FWHM = 3300 km s^{-1}) $H\alpha$ line component in polarized light (Oliva et al. 1998). Their picture is also supported by recent X-ray observations. Those above 10 keV suggest direct X-ray detection of the nucleus through a column density of $4 \times 10^{24} \text{ cm}^{-2}$ (Matt et al. 1999). The X-ray spectrum below 10 keV exhibits a flat continuum and a very prominent iron line, indicative of Compton scattering and fluorescent emission from gas illuminated by an obscured X-ray continuum source (Matt et al. 1996). Circinus shows highly ionized gas extending along the minor axis of the galaxy, with a morphology that is reminiscent of the ionization cones seen in other Seyfert galaxies (Marconi et al. 1994a). H_2O maser emission has been detected, and the masing gas traces a thin accretion disk about 0.4 pc in radius, and so does the inner $10 \mu\text{m}$ dust emission from the VLTI (Tristram et al. 2007). In addition, a fraction of the masers originates outside the disk, in what appears to be an outflow within ~ 1 pc of the nucleus and aligned with the ionization cone (Greenhill et al. 2003). Optical and near-infrared spectrophotometry of the nucleus show a typical Seyfert spectrum, including strong coronal lines (Oliva et al. 1994; Prieto et al. 2004). There are also lines from H_2 and low-excitation ionic species, both believed to be associated with starforming regions. The distribution and kinematics of the $\text{Br}\gamma$ line have been interpreted in terms of ongoing star formation activity within a few tens of parsecs of the active nucleus (Maiolino et al. 1998). A young stellar population with an age between 4×10^7 and 1.5×10^8 was found between these scales. Recent observations of the Circinus Galaxy in the range between $1 - 10 \mu\text{m}$ (Prieto et al. 2004), resolve a K_s -band source with a FWHM of ~ 2 pc and a spectral energy distribution compatible with a dust temperature of 300 K.

This chapter presents high-resolution, nearly diffraction-limited integral-field spectroscopic data of the Circinus galaxy in the K -band observed with the adaptive optics

(AO) assisted imaging spectrograph SINFONI (2004; Eisenhauer et al. 2003b). The physical scale associated with our spatial resolution is 4 pc, allowing us to investigate the properties of the nucleus and its interaction with the circumnuclear environment, highlighting the relationship between star formation and galactic nuclear activity.

We describe our observations and the data reduction procedure in Section 2.2. Section 2.3 describes the features observed in the spectrum of the galaxy and the methods we used to estimate the spatial resolution of our observations. In Section 2.4 we analyze the morphology of the nuclear source and the origin of the observed K -band continuum. Section 2.5 discusses the morphologies of the emission and the absorption, and the age of the starburst at the nucleus. Then, in Section 2.6 we discuss the kinematics of the emission and the mass distribution in the galaxy. Following these results, Section 2.7 deals with the gas density at the nucleus and the physical characteristics of the torus. A study of the detected coronal lines is presented in Section 2.8, and we present our conclusions in Section 2.9.

2.2 Observations and data reduction

The data presented here were obtained on 15 Jul 2004 during commissioning of SINFONI (Bonnet et al. 2004, Eisenhauer et al. 2003b) on the VLT UT4. The instrument consists of a cryogenic near-infrared integral-field spectrometer SPIFFI (Eisenhauer et al. 2003a) coupled to a visible curvature adaptive optics (AO) system (Bonnet et al. 2003). SINFONI performs imaging spectroscopy by cutting the two-dimensional field of view into 32 slices and then rearranging each of the slices (slitlets) onto a one-dimensional pseudo longslit, which is dispersed by a grating wheel and at last the spectra are imaged on the detector.

The AO module was able to correct on the nucleus of Circinus (for which it measured $R=14.1$ mag) in seeing of $\sim 0.5''$, to reach a resolution of $0.2''$ in the K -band (see Section 2.4). This performance is good considering that the optical nucleus of Circinus is rather extended rather than point-like. With the appropriate pixel scale selected, the spectrograph was able, in a single shot, to obtain spectra covering the whole of the K -band (approximately $1.95\text{--}2.45 \mu\text{m}$) at a spectral resolution of $R\sim 4200$ for each $0.0125'' \times 0.025''$ pixel in a $0.80'' \times 0.80''$ field of view. A total of 6 sky and 6 on-source exposures of 300 sec each were combined to make the final data cube with a total integration time of 1800 sec.

The data were reduced using the SINFONI custom reduction package SPRED (Abuter et al. 2005). This performs all the usual steps needed to reduce near-infrared spectra, but with the additional routines for reconstructing the data cube. Following subtraction of the sky frames from the on-source frames, the data were flatfielded and corrected for dead/hot pixels. The data were then interpolated to linear wavelength and spatial scales, after which the slitlets were aligned and stacked up to create a cube. Finally the atmospheric absorption was compensated using the A0V star HD 190285. Flux calibration was performed by comparison to the high spatial resolution broad

Line	λ^a (μm)	Flux ^b (10^{-18} Wm^{-2})
H ₂ 1–0 S(3)	1.9576	6.0
[SiVI]	1.9634	53.9
H ₂ 1–0 S(2)	2.0338	3.8
[AlIX]	2.040	10.0
[HeI]	2.0587	5.0
H ₂ 1–0 S(1)	2.1218	9.0
Br γ	2.1661	14.1
H ₂ 1–0 S(0)	2.2233	3.4
[CaVIII]	2.3213	36.9
H ₂ 1–0 Q(1)	2.4066	3.4

^a Wavelengths are in the rest frame

^b Uncertainties are approximately $3.2 \times 10^{-20} \text{ Wm}^{-2}$

Table 2.1: Measured nuclear emission line fluxes for Circinus. All measurements are given for a $0.8''$ circular aperture centered on the continuum peak.

band K_s image and photometry obtained with NAOS-CONICA of 11.4 mag in a $0.38''$ aperture (Prieto et al. 2004), which was also cross-checked with 2MASS photometry.

No additional point-spread function (PSF) calibration frames using stars were taken. This is primarily because, although in principle one can match the brightness of a calibration star on the wavefront sensor to the AGN, it is not possible to replicate either the spatial extent of the AGN or the background galaxy light associated with it – resulting in a potentially considerable mismatch between the science and calibration PSFs (Davies et al. 2004c). The spatial resolution has instead been measured using the methods described in Section 2.3.1.

2.3 Spectroscopic features and spatial resolution

The purpose of this section is to present general results extracted from the data to provide an overview of the features observed in the nuclear region of Circinus. A more detailed analysis is given in subsequent sections.

2.3.1 Spatial Resolution

A good way to estimate the spatial resolution is by using a broad line in the spectrum, such as a potential observation of Br γ emission from the BLR, which at the distance of Circinus is expected to be spatially unresolved. This has the advantage

of measuring the spatial resolution directly from the science frames, and includes all effects associated with shifting and combining the cube. Nevertheless, as can be seen in Figure 2.1, we have detected only narrow lines, which are spatially resolved in our observations. As a result, and due to the lack of other point sources in the field, we used indirect means to derive our spatial resolution, making use of a NACO image of the galaxy from Prieto et al. (2004) which contains unresolved star clusters over a field of view of $27'' \times 27''$. Two approaches were used to estimate the PSF of our observations by means of the NACO image. One method of estimating the SINFONI PSF effectively consists of deconvolving the SINFONI continuum image with the intrinsic image of the galaxy, since:

$$\text{IM}_S = \text{PSF}_S \otimes \text{IM}_{\text{intr}} \quad (2.1)$$

where IM_S is the Circinus image from SINFONI, PSF_S is the point spread function, and IM_{intr} is the intrinsic image of the galaxy. We obtained the intrinsic image in a similar way, by first deconvolving the NACO image with the NACO PSF. In the NACO image, the smooth underlying galaxy profile was approximated by isophotal analysis using the isophote package from IRAF. This was then subtracted, leaving only the compact sources in the field. The narrowest point in this subtracted image was used as the NACO PSF, which was measured directly to have $0.14''$ FWHM. The deconvolution of the NACO image with its PSF was performed using the Lucy algorithm (Lucy 1974) also implemented in IRAF. This deconvolved image was rebinned to our pixel scale of $0.0125''/\text{pix}$. For the final stage, instead of deconvolving IM_S with IM_{intr} , we fit the SINFONI image with the intrinsic image convolved with the parameterized PSF_S . This avoids the noise amplification which is an inherent feature of deconvolution. The PSF_S could be well matched by a symmetrical moffat function. Mismatches were minimized by varying the parameters (center, scale, α and β) of a moffat function defined as $I(r) = \left(1 + \left(\frac{r}{\alpha}\right)^2\right)^{-\beta}$ and then performing a χ^2 minimization test, resulting in a FWHM spatial resolution of $0.20''$ (~ 3.9 pc) with $\alpha = 0.148''$ and $\beta = 1.8$ for this method. An elliptical moffat function was also tested as a possible PSF for our observations. However, this did not improve significantly the fit and so was discarded.

In order to avoid the first deconvolution of the method described above, the second approach to derive the SINFONI PSF consists of convolving the NACO PSF with a parameterized degradation function, the latter being obtained by fitting the SINFONI image with the NACO image convolved with the same function. A symmetrical moffat function was used as degradation function. Once again, mismatches were minimized by varying the parameters of the moffat function and then performing a χ^2 minimization. The SINFONI PSF was obtained by convolving the NACO PSF with the degradation function. The final FWHM resolution estimated in this way was $0.22''$ (~ 4.2 pc) with $\alpha = 0.219''$ and $\beta = 3.2$.

The confidence on the resulting PSF for both cases was evaluated by the residual of the fitting the following function which considers the difference between the data and model, weighted according the flux in each pixel, and normalised by the total

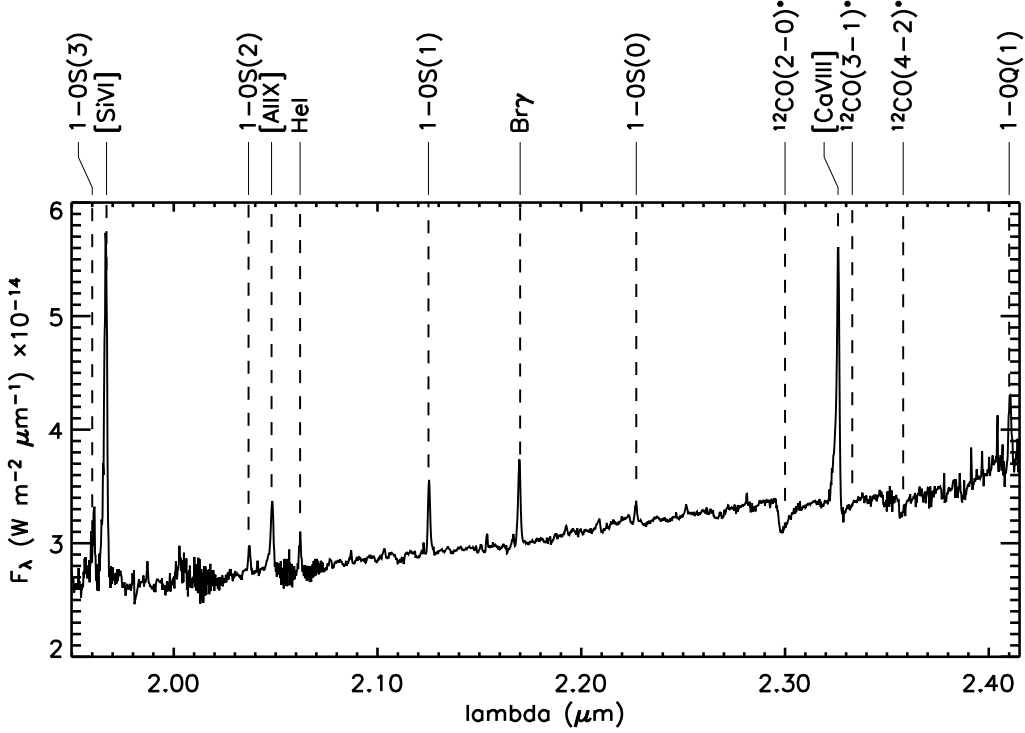


Figure 2.1: Nuclear spectrum of Circinus, extracted from the SINFONI datacube in a $0.8''$ square aperture. Labels marked with an asterisk represent stellar CO absorption bandheads. The effect of dilution on these bandheads is clearly seen.

flux in the frame:

$$\text{Residual} = \frac{\sqrt{\sum((IM_S - Model)^2 \cdot IM_S)}}{(\sum(IM_S))^{1.5}} \cdot 100 \quad (2.2)$$

where IM_S is the SINFONI continuum image as above and $Model$ is our constructed image – either the intrinsic galaxy profile convolved with the SINFONI PSF, or the NACO image convolved with the degradation function. The numerator is the quantity minimized during the fit, which was then normalized using the integrated image of the continuum. The residual of the fit in both cases was evaluated as 0.1%, indicating that both methods performed equally well in estimating the PSF. We chose to adopt the PSF obtained by the second approach because no deconvolution is performed.

2.3.2 Distribution of emission and absorption features

In Figure 2.1 we present a spectrum of Circinus at a spectral resolution of $R \sim 4200$, integrated over a $0.8''$ square aperture centered on the nucleus. The most prominent of the emission lines are the coronal lines [SiVI] at $1.96 \mu\text{m}$ and the [CaVIII] at $2.32 \mu\text{m}$. We also detect the [AlIX] $2.04 \mu\text{m}$ line, first mentioned by Maiolino et al. (1998). In addition to these high excitation lines, the H_2 1–0S(1) $2.12 \mu\text{m}$ and $\text{Br}\gamma$ $2.17 \mu\text{m}$ emission lines are clearly recognizable. The line fluxes, which are presented in Table 2.1, are comparable to previous measurements (Maiolino et al. 1998).

The K -band flux density, calculated from the continuum image shown in Figure 2.2 within an aperture of $0.8''$ is $3.1 \times 10^{-14} \text{ Wm}^{-2} \mu\text{m}^{-1}$ (approximately 50 mJy). The stellar features, traced by the CO bandheads, are also distinguishable in the spectrum. However, not all of the stellar features are diagnostically useful. For example, the ^{12}CO (3-1) band is partially filled by the [CaVIII] emission line, and the rest of the bandheads with wavelengths longer than $2.34 \mu\text{m}$ are affected by residual atmospheric features or other emission lines. Therefore, only the ^{12}CO (2-0) band was useful to extract information about the fraction of the nuclear flux that is indeed stellar.

Images of the $2.2\text{-}\mu\text{m}$ continuum and the $\text{Br}\gamma$, H_2 (1–0)S(1), [Ca VIII], and [SiVI] line emission, as well as the ^{12}CO (2-0) bandhead flux are presented in Figure 2.2. The location of the nucleus, as defined by the centroid of the continuum emission, has been marked with an encircled cross in all maps. This source is offset by $\sim 0.15''$ to the south-east of the peak of the $\text{Br}\gamma$ and H_2 1–0S(1) line emission as well as of the stellar light. Such an offset is consistent with the results of Prieto et al. (2004) who found that the center of the K -band radiation is located at $\sim 0.15''$ south-east of the brightest central emission seen in the J -band and HST F814W images. In contrast to these authors who argued that the K -band source is fully obscured at shorter wavelengths and that the emission at these shorter wavelengths is due to nuclear light scattered by the compact dusty structure surrounding the Circinus nucleus, our results suggest a different interpretation because the offset remains even in the K -band but only for particular components of the line and continuum emission. We argue that, at least for near-infrared emission, the offset arises because the star formation is centered $\sim 0.15''$ to the north west of the non-stellar continuum peak. The issue of extinction is addressed further in Section 2.7.

2.4 Nuclear dust emission

The observed equivalent width of the ^{12}CO (2-0) bandhead was used to obtain the fraction of the nuclear flux from the stars in this region, by assuming that the intrinsic (i.e. purely stellar) equivalent width in the nuclear region must be consistent with values predicted by the models created with the stellar population synthesis code STARS (Sternberg 1998; Thornley et al. 2000; Davies et al. 2003). We used the measured flux of the ^{12}CO (2-0) band to estimate the amount of non-stellar continuum

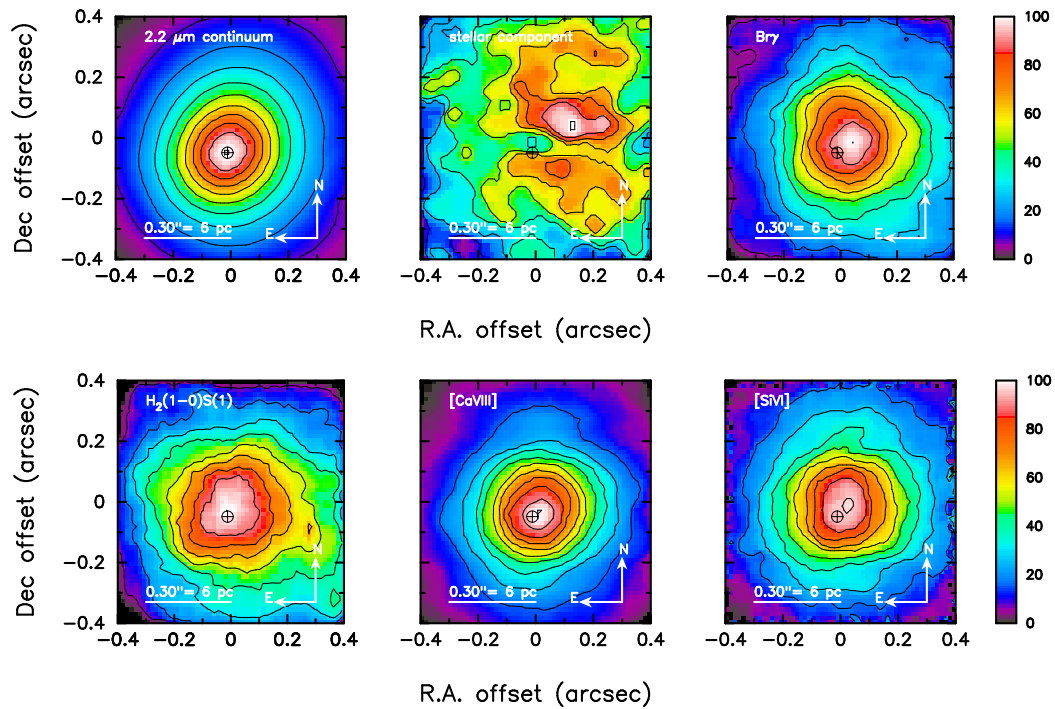


Figure 2.2: Intensity images extracted from the SINFONI data cube in the central arcsec of Circinus. In each case, the colour scale extends from 0-100% of the peak flux, and contours are spaced equally between 20% and 90% of the peak flux. An encircled cross indicates in each case the peak of the continuum emission. The maps show, starting from the left corner, *Top left*: $2.2\mu\text{m}$ continuum, *Top center*: stellar component (flux contained in the stellar absorption bandhead $^{12}\text{CO}(2-0)$), *Top right*: $\text{Br}\gamma$, *Bottom left*: H_2 1-0S(1), *Bottom center*: [Ca VIII], and *Bottom right*: [Si VI].

using the equation:

$$1 - D = \frac{EW_{\text{obs}}}{EW_{\text{intr}}} \quad (2.3)$$

where D is the dilution factor, that is the ratio of stellar to total continuum, and EW_{obs} and EW_{intr} are the observed and intrinsic stellar equivalent widths respectively. The intrinsic equivalent width is nearly independent of star formation history for any ensemble of stars as predicted by the STARS models, having an almost constant value of $\sim 12 \text{ \AA}$ assuming solar metallicity (Davies et al. 2006). The observed stellar equivalent width in the central $0.8''$ was found to be $\sim 1.8 \text{ \AA}$, implying that $\sim 85\%$ of the total nuclear K -band luminosity in this region originates from the non-stellar component, a fraction that increases on smaller scales. In Figure 2.3, the K -band continuum azimuthally averaged radial surface brightness profile is plotted along with those of the PSF and stellar and non-stellar components. The stellar component represents the radial profile of the stellar absorption bandhead $^{12}\text{CO}(2-0)$ image in Figure 2.2. All profiles are normalized to their respective peak values; and the stellar profile is centered $0.15''$ north west of the non-stellar profile. The predominance of the non-stellar component on these scales is vividly demonstrated by the similarity of the non-stellar and total K -band profiles, as well as by the red spectral slope in Figure 2.1.

Such nuclear K -band emission is interpreted as thermal radiation from hot dust which is heated by the intense UV and X-ray radiation emitted by the Seyfert nucleus. It is often assumed that the dust is close to the sublimation limit ($\sim 1600 \text{ K}$) since it is the hottest emission which will have the greatest impact in the near infrared. However, the slope of the nuclear spectrum in the K -band indicates a temperature (unreddened) closer to 740 K , similar to that found for NGC 1068 by Thatte et al. (1997), but significantly more than the 300 K derived by Prieto et al. (2004) from modelling the broad band colours. Since the spectral range of the K -band is smaller than the $1\text{--}10\mu\text{m}$ interval used by Prieto et al. (2004), the spectral slopes in these ranges are different, but nevertheless compatible. The estimated temperature of $\sim 700 \text{ K}$ from the K -band continuum characterizes only the hottest dust, while 300 K dust would dominate the mid-infrared SED.

As can be seen from Figure 2.3, the non-stellar K -band source is marginally resolved. Indeed, a quadrature correction of its FWHM ($\sim 0.3''$) with that of the PSF yields an intrinsic size of $\sim 0.2''$ (3.9 pc). The factor of 2 discrepancy with the size reported by Prieto et al. (2004) arises primarily from the spatial resolution estimated in the NACO data. Compared to their $0.16''$ our estimate is $0.14''$, which would give a source size of $\sim 0.15''$. This emphasises the difficulty of estimating the intrinsic size of only marginally resolved sources. Within the uncertainty of about $0.05''$, the sizes are consistent with each other and with those predicted by the torus models (Pier & Krolik 1992, Pier & Krolik 1993; Nenkova et al. 2002) in which the inner edge of the dust torus lies $\sim 1 \text{ pc}$ away from the AGN.

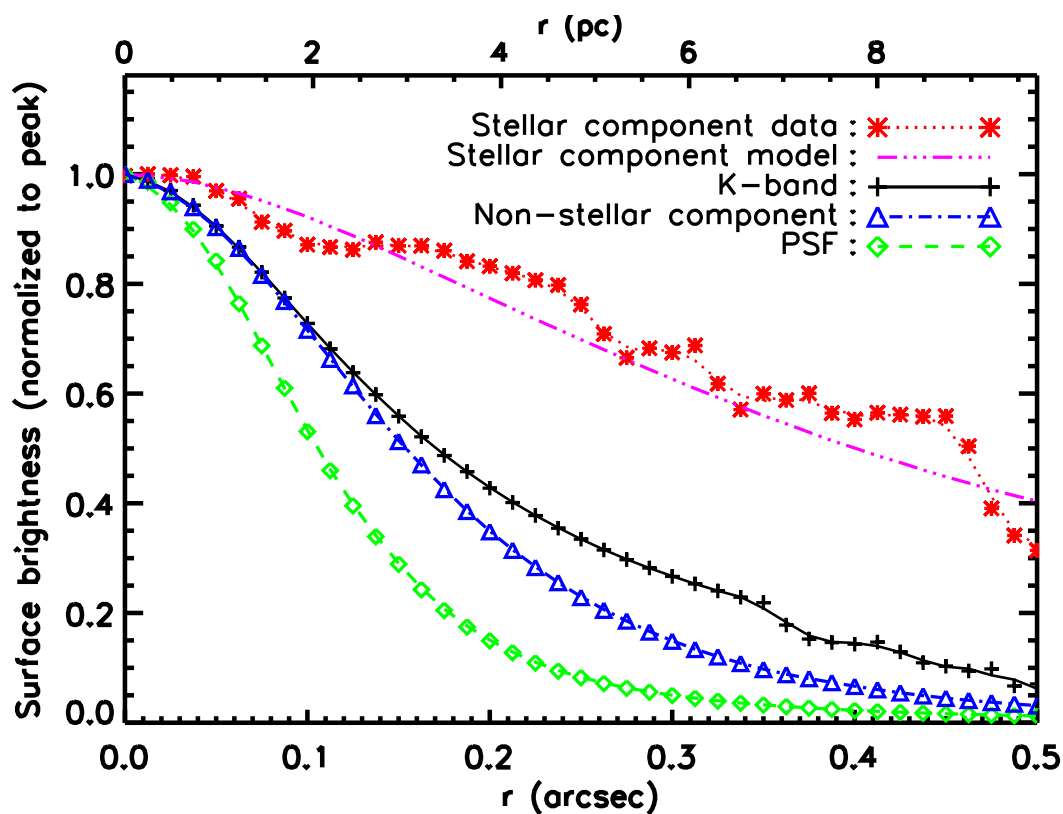


Figure 2.3: Radial profile of the nuclear K -band surface brightness obtained from an integrated image of the SINFONI datacube (crosses connected by a solid line). The SINFONI K -band stellar component (same as stellar continuum) is represented by asterisks connected by a dotted line. The triple-dotted-dashed line represents a model fitted to the stellar component data, which is the exponential profile convolved with the PSF. Open triangles connected by a dotted-dashed line indicate the fraction of the K -band radiation which does not come from stars. The open diamonds connected by a short-dashed line indicate the PSF profile.

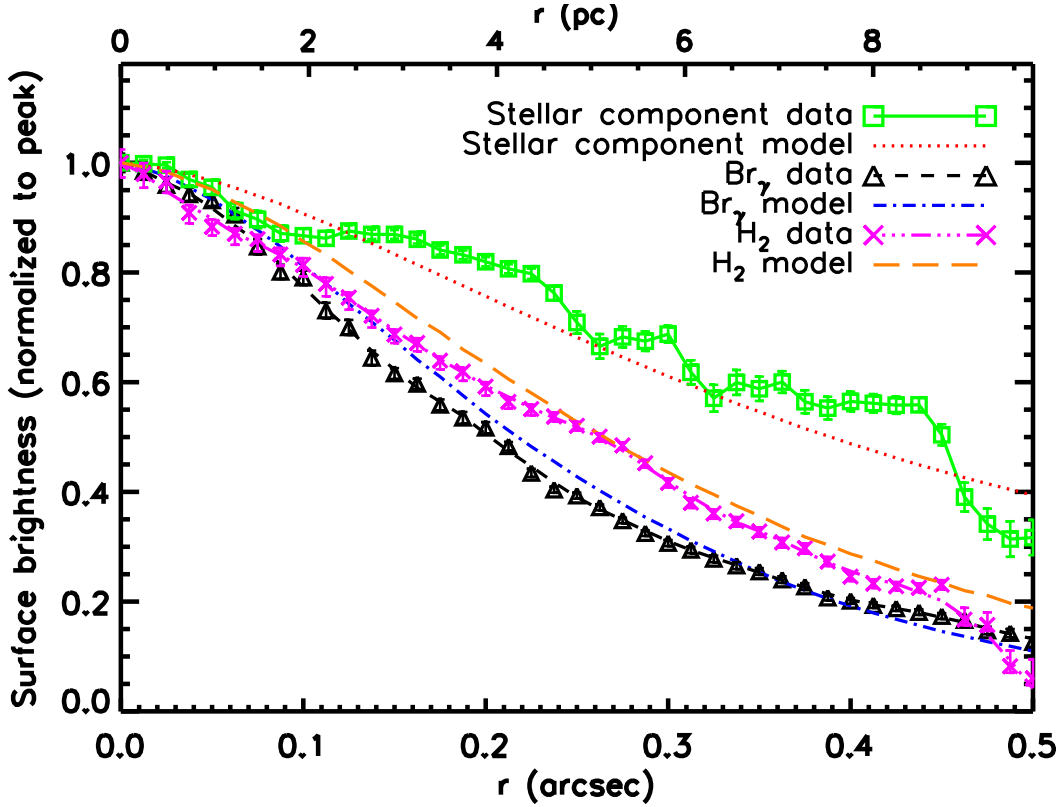


Figure 2.4: Radial profile of the surface brightness of the H₂ 1–0S(1) (crosses connected by a triple-dotted-dashed line) emission line. The long-dashed line represents a model fitted to the linemap, which is the exponential profile convolved with the PSF. The narrow Br γ radial profile is represented by open triangles connected by a short-dashed line and its model by the dotted-dashed line. Open squares connected by a solid line indicate the nuclear stellar profile, whereas its model is represented by the dotted line.

2.5 Nuclear star formation

Images of the Br γ and H₂ 1–0S(1) line emission, which are often associated with star formation, are presented in Figure 2.2. As the AGN is highly obscured (see Oliva et al. 1998 and Matt et al. 1996, 1999), no broad line region is visible. Several lines of evidence suggest that the Br γ emission is associated with star formation activity surrounding the Seyfert nucleus rather than the narrow line region and ionisation cone. These are the similarity of the morphologies of the Br γ , ¹²CO (2–0), and H₂ 1–0S(1) emission: the ¹²CO (2–0) is only slightly more extended than the two lines, and all three are offset to the north west. Additional support is provided by the consistency and uniformity of the Br γ and H₂1–0S(1) velocity fields and dispersion maps (see Section 2.6 and Figure 2.7). In particular, the velocity field of the Br γ

has a gradient matching that of the galaxy's major axis rather than showing signs of outflow along the minor axis. We note in fact that the H_2 1–0S(1) appears to be slightly more extended than the $\text{Br}\gamma$, particularly at weaker levels westwards in the direction of the ionization cone (Maiolino et al. 1998); and it is only in this region that there are significant differences between their velocity fields, with the 1–0S(1) showing signs of outflow. Figure 2.4 shows the azimuthally averaged surface brightness radial profiles of the H_2 1–0S(1) and narrow $\text{Br}\gamma$ emission lines and the ^{12}CO (2–0) stellar absorption bandhead.

Both an exponential profile and $r^{1/4}$ de Vaucouleurs profile provide good matches to each of these. We prefer to parameterise the profile with the former, because of the clear evidence of a circumnuclear disk from the existence of certain features (namely a bar, Maiolino et al. 2000; and a ring, Marconi et al. 1994b). At these scales, less than 20 pc, the $\text{Br}\gamma$, and H_2 1–0S(1) data are characterised by a disk-scale length $r_d = 4_{-0.2}^{+0.1}$ pc. Due to the symmetry in the morphology of the $\text{Br}\gamma$, and H_2 1–0S(1) profiles, the profiles were not corrected for inclination. This would perhaps be a surprising result for an inclined disk, but indeed the kinematics and simulations suggest that the thickness of the disk plays an important part in the observed morphology: a disk inclined at 65° with a thickness of only 4 pc FWHM – equivalent to an exponential scale height of 1.7 pc – is consistent with the symmetrical morphology. We return to this point in Section 2.6 where we discuss the kinematics in more detail.

The complex morphology of the stellar component was analyzed in more detail by several simulations. Since the observed stellar luminosity is expected to be produced by several clusters, simulations were carried out in order to study the way the clusters superpose to create the observed complex morphology. In the simulations each cluster was defined by two parameters: its position inside the field, and its mass. The positions were assigned randomly following the radial distribution of the stellar component in Figure 2.4, so that the probability of finding a cluster in any position depends on an exponential profile slightly more extended than the line emission. For the mass distribution, systems of young clusters, including super star clusters which are preferentially found at the very heart of starbursts, appear to be well represented by a power law mass and luminosity function with $\alpha = -2$. The range of masses was from 1×10^3 to $3 \times 10^5 M_\odot$ which are typical values for star clusters (Meurer et al. 1995). Each cluster was characterized by a two dimensional Gaussian function with $\text{FWHM} = 0.2''$, our spatial resolution. The clusters were generated randomly over a circular field of $0.5''$ radius. According to the mass distribution, a mass was assigned to each of them until the observed stellar mass in the region was reached, namely $1 \times 10^6 M_\odot$ (see below). Each cluster had the same mass-to-light ratio. The summation of all clusters over the whole field yields the overall morphology of the stellar component. Figure 2.5 shows the results of the simulations. It can be seen from Figure 2.5 that when massive star clusters are present in the field, the clumpiness of the whole set increases. On the other hand, for a low mass distribution the field remains uniform and symmetric, and therefore the clumpiness decreases.

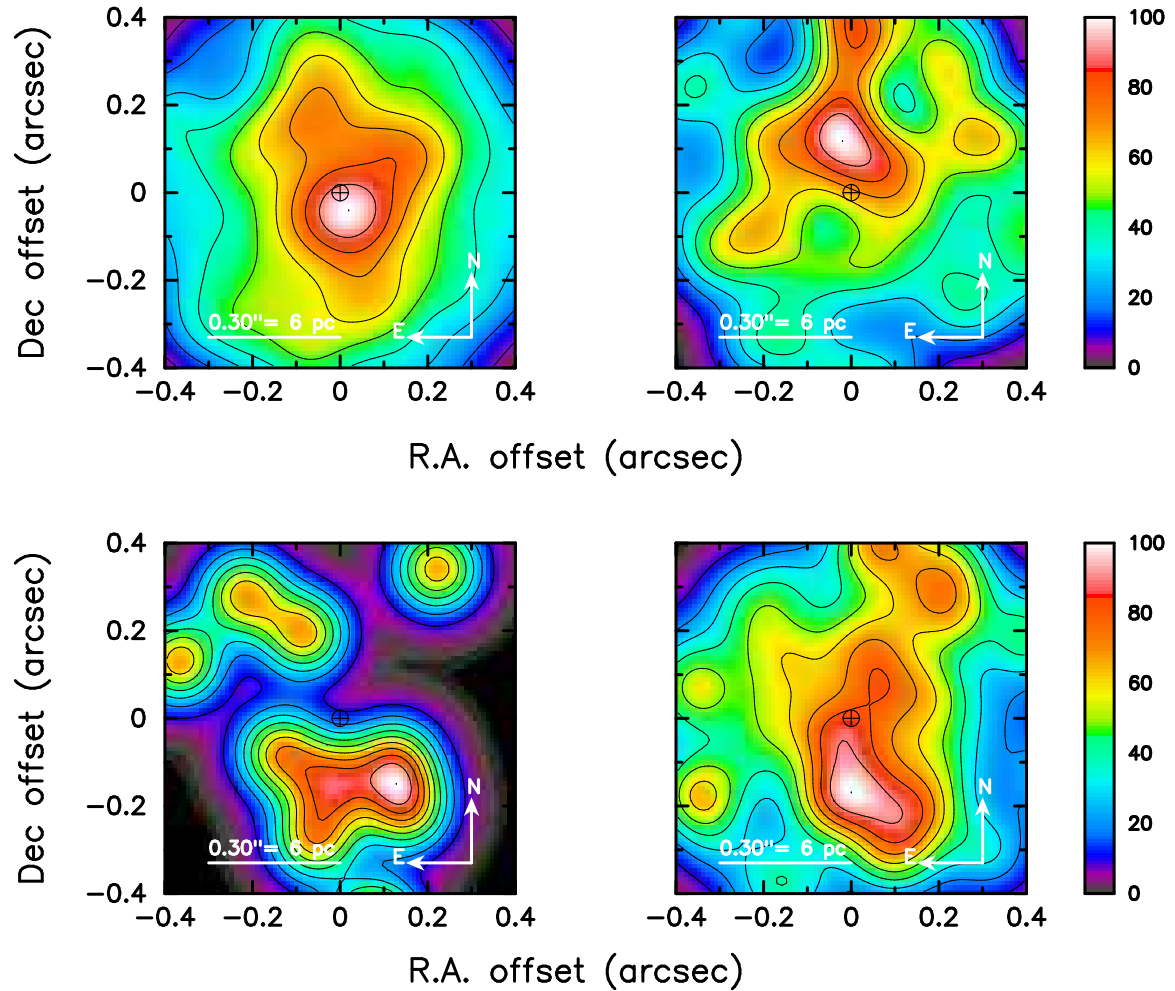


Figure 2.5: Intensity images of the star clusters simulations in the central arcsec of Circinus. In each case, the colour scale extends from 0-100% of the peak flux, and contours are spaced equally between 10% and 90% of the peak flux. An encircled cross indicates in each case the center of the region. The maps show, starting from the left corner, *Top left*: 1000 star clusters with constant mass $1 \times 10^3 M_{\odot}$, *Top right*: 100 star clusters with constant mass $1 \times 10^4 M_{\odot}$, *Bottom left*: 10 star clusters with constant mass $1 \times 10^5 M_{\odot}$, and *Bottom right*: 300 star clusters with masses varying from $1 \times 10^3 M_{\odot}$ to $5 \times 10^4 M_{\odot}$.

The observed morphology in Figure 2.2 can be best reproduced by a set of star clusters with a mass distribution ranging from 1×10^3 to $5 \times 10^4 M_\odot$, or alternatively a constant mass with value of $1 \times 10^4 M_\odot$, although other scenarios cannot be excluded. Our simulations indicate that the observed complexity and asymmetry of the morphology of the stellar component could easily arise from the superposition of a number of star clusters with typical mass $10^4 M_\odot$.

We determine the age of the star formation by means of two diagnostics: the intrinsic equivalent width of the Br γ line and the supernova rate to stellar K -band luminosity ratio (ν_{SN}/L_K^*) in the nuclear region. These provide independent information on the star formation history, the former representing the number of hot young blue supergiant stars and the latter the number of supernova remnants, both normalised to the number of later type red giant and supergiant stars. By comparing the two diagnostics to models, the age of the starburst can be satisfactorily constrained. The $EW(\text{Br}\gamma)$ was estimated from the observed Br γ flux and the stellar continuum (i.e. corrected for dilution by subtracting the continuum contribution from hot dust), resulting in $EW(\text{Br}\gamma) = 30 \text{ \AA}$ in a $0.8''$ aperture. The supernova rate ν_{SN} was obtained using the empirical relation presented in Condon (1992) with a spectral index $\alpha = 0.1$ (as measured between 5 and 8.64 GHz), and a flux density at 8.64 GHz of $S_{10} = 12 \text{ mJy}$, resulting in a value of $\nu_{\text{SN}} = 2.21 \times 10^{-4} \text{ yr}^{-1}$. The radio flux density was calculated by means of the $1''$ resolution radio image from Davies et al. (1998). The flux density at 8.64 GHz was summed over an aperture of $0.8''$, to be consistent with our fluxes, giving 14 mJy. Then the thermal contribution was calculated as given in Condon (1992) for a standard electron temperature of $1 \times 10^4 \text{ K}$. The resulting 2 mJy was subtracted from the total flux density at 8.64 GHz. Dividing ν_{SN} found in this way by the stellar K -band luminosity L_K^* of $1.5 \times 10^6 L_\odot$ found after multiplying the observed K -band luminosity L_K by the dilution factor D , yielded a ratio of $1.5 \times 10^{-10} L_\odot^{-1} \text{ yr}^{-1}$.

We have used the evolutionary synthesis code STARS (1998; 2000, Davies et al. 2003) to determine the star formation history assuming an exponentially decaying star formation rate of the form $\exp(-t/t_{\text{scl}})$, where t_{scl} is the burst decay time scale and t is the age of the star cluster. We make the standard assumptions of solar metallicity, and a Salpeter IMF of slope $\alpha = -2.35$ in the range 1–120 M_\odot . An important advantage of this model is that it allows us to study not only instantaneous and continuous scenarios, but also finite star formation timescales.

We obtain different ages for the starburst depending on the timescale of the star formation. We consider 4 timescales: continuous star formation with $t_{\text{scl}} = 10^9 \text{ yr}$, an instantaneous burst with $t_{\text{scl}} = 10^6 \text{ yr}$, and two intermediate scenarios with $t_{\text{scl}} = 10^7$ and 10^8 yr . First, we compared the calculated intrinsic Br γ equivalent width with that from STARS. Figure 2.6 shows the evolution of $EW(\text{Br}\gamma)$, ν_{SN}/L_K^* , M_*/L_K^* and L_{bol}^*/L_K^* as functions of cluster age for each model. It can be seen from this figure that $EW(\text{Br}\gamma)$ alone cannot constrain the age since all scenarios are plausible.

Using the ratio ν_{SN}/L_K^* together with $EW(\text{Br}\gamma)$, we note that within the central

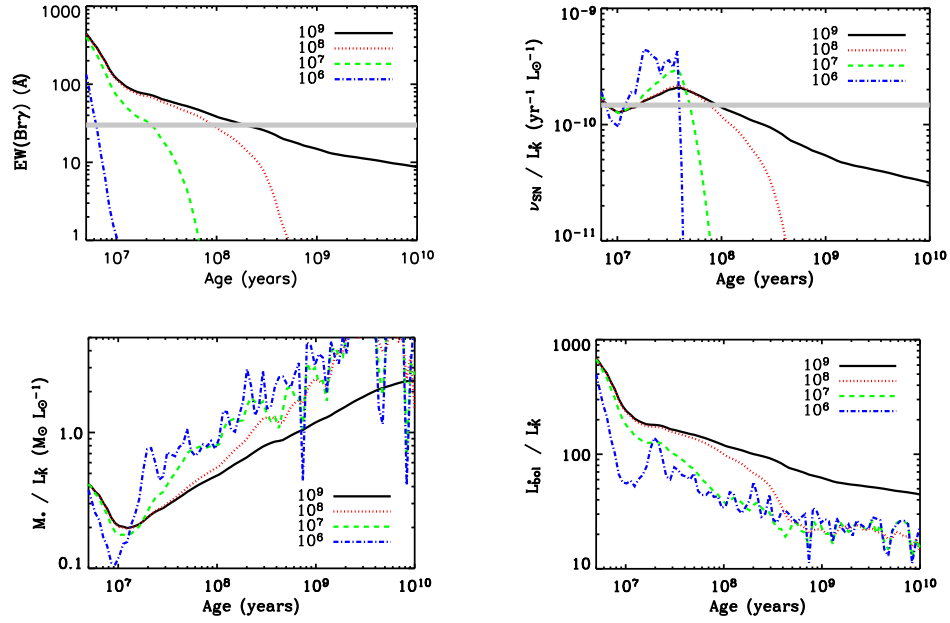


Figure 2.6: Evolution of $EW(\text{Br}\gamma)$ (*Top left*), $\nu_{\text{SN}}/L_{\text{K}}^*$ (*Top right*), M_*/L_{K}^* (*Bottom left*) and $L_{\text{bol}}^*/L_{\text{K}}^*$ (*Bottom right*) with age for a stellar cluster with four star formation histories. The gray bands indicate the range of the observed ratios. An asterisk indicates that the parameter refers to its stellar component.

$R < 8$ pc, the constant and the instantaneous star formation models do not fit completely both of the observational constraints ($EW(\text{Br}\gamma) = 30 \text{ \AA}$ and $\nu_{\text{SN}}/L_{\text{K}}^* = 1.47 \times 10^{-10} L_{\odot}^{-1} \text{ yr}^{-1}$).

The star formation timescales $t_{\text{scl}} = 10^7$ and $t_{\text{scl}} = 10^8$ yr do fit these constraints from the intersections points at 2×10^7 and 8×10^7 yr respectively. While the data are consistent with these two scenarios, the shorter timescale would require a degree of fine-tuning, particularly since the supernovae responsible for the radio continuum are only just beginning to appear and $EW(\text{Br}\gamma)$ is decaying relatively quickly. Thus there is only a small range of possible ages for this timescale. At an age of 80 Myr, the constraints give rise to a wider range of allowed ages, suggesting this is the more likely scenario. Crucially, in either case the data indicate the presence of a young stellar population within a few parsecs of the active nucleus which is now less than half as intense as when it began.

For the preferred star formation scenario given above we find a current mass to K -band luminosity ratio of $\sim 0.6 M_{\odot}/L_{\odot}$, yielding a stellar mass of $M_* \approx 1 \times 10^6 M_{\odot}$. Another important parameter to analyze is the bolometric luminosity attributable to the nuclear star formation. Figure 2.6 shows the evolution of the bolometric luminosity to K -band luminosity ratio for an ensemble of stars. From this Figure we obtain $L_{\text{bol}}^*/L_{\text{K}}^* \approx 150$. By multiplying this ratio by the observed stellar K -band luminosity of $L_{\text{K}}^* = 1.5 \times 10^6 L_{\odot}$, we find that the star formation in this region has $L_{\text{bol}}^* = 2.3 \times 10^8 L_{\odot}$ and accounts for 1.4% of the bolometric luminosity of the entire galaxy ($L_{\text{bol}} = 1.7 \times 10^{10} L_{\odot}$, Maiolino et al. 1998).

Let us now assume a screen extinction of $A_{\text{V}} = 9$ mag, as suggested by Maiolino et al. (1998) for the nuclear region. Since $A_{\text{K}} \approx A_{\text{V}}/10$ (Howarth 1983), L_{K}^* is ~ 2 times that observed. This consideration has no effect on the $EW(\text{Br}\gamma)$, but it reduces the $\nu_{\text{SN}}/L_{\text{K}}^*$ by a factor of two. This new constraint does not change the preferred star formation scenario, still suggesting that the star formation is very young. The bolometric luminosity attributable to the nuclear star formation in this case would be $L_{\text{bol}}^* = 4.5 \times 10^8 L_{\odot}$.

A perhaps more physical model than screen extinction is mixed extinction, where the dust and gas are uniformly mixed with the stars. In either case, the near-infrared color excess is defined as

$$E_{H-K} = -2.5 \log \left[\frac{I_H/I_{0H}}{I_K/I_{0K}} \right] \quad (2.4)$$

where, I_H and I_K are the observed intensities in the two bands, and I_{0H} and I_{0K} are the intrinsic intensities. One can then use either $I_{\lambda}/I_{0\lambda} = e^{-\tau_{\lambda}}$ for the screen model or $I_{\lambda}/I_{0\lambda} = (1 - e^{-\tau_{\lambda}})/\tau_{\lambda}$ for the mixed model to derive the optical depth. With the usual wavelength scaling that $\tau_{\text{V}} = 5.5\tau_{\text{H}} = 9.7\tau_{\text{K}}$ one can then estimate the optical depth in the visual. The near-infrared excess $E_{H-K} = 0.45\text{--}0.60$ reported by Maiolino et al. (1998) then implies an extinction, after accounting for the galactic foreground, of $\tau_{\text{V}} = 4.4\text{--}6.2$ for the screen model, and $\tau_{\text{V}} = 12\text{--}25$ for the mixed model, similar

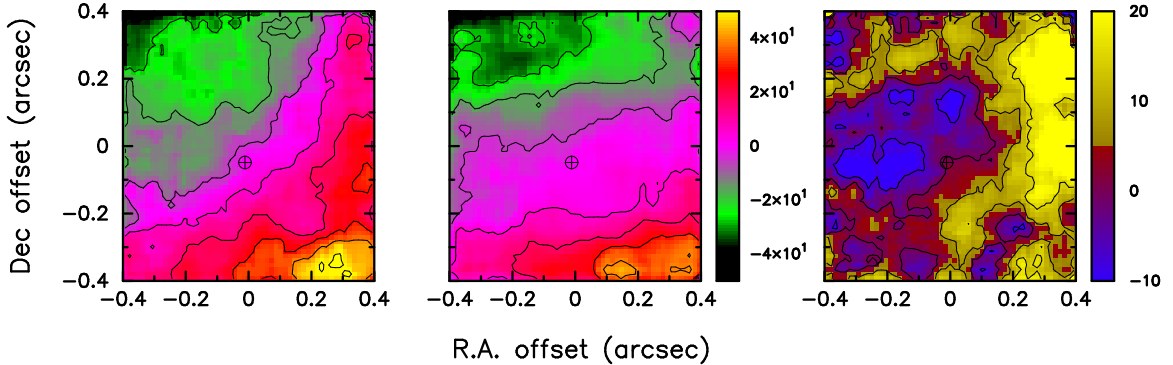


Figure 2.7: Velocity maps extracted from the SINFONI data cube in the central $0.8'' \times 0.8''$ of Circinus. The maps show, from left to right: H₂ 1-0S(1), Br γ and difference in the velocity fields of the two lines. For the case of H₂ 1-0S(1) and Br γ velocity maps, the colour scale extends from $[-50, 50]$ km s⁻¹, and contours are spaced equally every 10 km s⁻¹. For the difference in the velocity fields, the colour scale extends from $[-10, 20]$ km s⁻¹, and contours are spaced equally every 5 km s⁻¹. The difference in the velocity maps ranges between $[-10, 10]$ km s⁻¹, except for the western edge of the map, where a difference of ~ 25 km s⁻¹ is observed. An encircled cross indicates in each case the peak of the continuum emission.

to the estimate of Prieto et al. (2004). We note also that for the mixed model, the colour excess will saturate because if τ_λ is greater than a few, $I_\lambda/I_{0\lambda} \sim 1/\tau_\lambda$ so that the excess becomes $E_{H-K} \sim -2.5 \log \tau_K/\tau_H$. The limiting value of $E_{H-K} = 0.6$ is consistent with the upper end of the measured range, suggesting that greater extinctions cannot be ruled out. We can, nevertheless, impose a very strong limit on the maximum possible extinction: the intrinsic luminosity from this nuclear star formation cannot exceed the galaxy's bolometric luminosity ($L_{\text{bol}}^{*,nuc} < L_{\text{bol}}$). The lower limit, that $L_{\text{bol}}^{*,nuc} > L_{\text{bol}}/75$, comes from the starburst model under the assumption of no extinction. The actual value of $L_{\text{bol}}^{*,nuc}$ is governed by the scaling of the starburst model. And this scaling depends directly on the ratio between the intrinsic and observed fluxes in the waveband where it is determined. Since the ratio between the intrinsic K -band and bolometric luminosities of the nuclear stellar component is fixed by the starburst model, it follows that the intrinsic K -band stellar luminosity must be less than 75 times the observed K -band stellar luminosity. Assuming a mixed model, one has $I_K/I_{0K} \sim 1/\tau_K$, implying that $\tau_K \sim 75$, equivalent to $\tau_V \sim 750$. A more meaningful, although less robust, limit is found if one excludes the circumnuclear star formation which Maiolino et al. (1998) estimated to account for $\sim 10^{10} L_\odot$. In this case $L_{\text{bol}}/L_{\text{bol}}^{*,nuc} < 30$ and the maximum optical depth would be of order $\tau_V \sim 300$. Although these limits are large, they are important and further discussion on the extinction will be presented in Section 2.7.

Galaxy	$\log \frac{L_{(1-0)S(1)}}{L_{\odot}}^a$	$\log \frac{M_{\text{gas}}}{M_{\odot}}$	$\log \frac{L_{\text{IR}}}{L_{\odot}}$	$\log \frac{L_{(1-0)S(1)}}{L_{\text{IR}}}$	$\log \frac{L_{(1-0)S(1)}}{M_{\text{gas}}}$	References ^b
(1)	(2)	(3)	(4)	(5)	(6)	(7)
IR 01364-1042	6.7	10.2	11.8	-5.0	-3.4	1
IR 05189-2524	7.0	10.4	12.1	-5.1	-3.4	1
IR 09111-1007	6.9	10.4	11.9	-5.0	-3.4	1
IR 14378-3651	6.8	10.2	12.1	-5.3	-3.3	1
IR 17208-0014	7.3	10.6	12.3	-5.1	-3.4	1
NGC1614	6.2	9.7	11.6	-5.3	-3.5	2
NGC2623	6.5	10.0	11.5	-5.0	-3.5	2
IR 10173-0828	5.8	9.9	11.8	-5.9	-4.1	2
NGC6090	6.7	10.5	11.5	-5.0	-4.0	2
NGC6240	8.0	10.6	11.8	-3.9	-2.6	2
NGC7469	6.4	10.2	11.6	-5.2	-3.8	2
Mrk231	7.2	10.3	12.5	-5.3	-3.1	2
Mrk273	7.3	10.6	12.1	-4.8	-3.3	2
Arp220	7.0	10.5	12.2	-5.2	-3.5	2
NGC695	6.4	10.6	11.7	-5.2	-4.2	3
NGC1068	6.0	10.0	11.5	-5.5	-4.0	3
NGC5135	6.2	10.2	11.1	-4.9	-4.0	3

^a Reference for $L_{(1-0)S(1)}$ data: Goldader et al. (1997), except for NGC 6090 Sugai et al. (2000)

^b References for M_{gas} data: (1) Mirabel et al. (1990); (2) Bryant & Scoville (1999); (3) Gao & Solomon (2004)

Table 2.2: Properties of the sample of luminous and ultraluminous infrared galaxies used to estimate $L_{(1-0)S(1)}/M_{\text{gas}}$.

2.6 Gas kinematics and mass in the nuclear region

In Figure 2.7 the projected velocity maps of the H_2 and the $\text{Br}\gamma$ lines are presented, as well as the difference in the velocity fields of the two lines. The maps for both emission lines are broadly consistent, exhibiting a gradual increase in velocity from north to south along a position angle (P.A.) of $\sim 18^\circ$ for the $\text{Br}\gamma$ and $\sim 25^\circ$ (excluding the righthand side, see below) for the 1-0S(1). Given the typical uncertainty of 5-10° in each of these, they are consistent. They are the same as the galaxy's major axis (Freeman et al. 1977), a strong indication of pure galaxy rotation, and suggesting that there are no warps in the galaxy down to scales at least as small as a few parsecs. At smaller scales (from 0.1 to ~ 0.4 pc), the maser emission traces a warped, edge-on accretion disk, which changes the P.A. from $\sim 29^\circ$ at 0.1 pc to $\sim 56^\circ$ at 0.4 pc

(Greenhill et al. 2003). Our results suggest that at larger scales (~ 1 pc), possibly at the starting point of the torus, the galaxy's position angle has reverted back to $\sim 25^\circ$.

The fact that the P.A. for the H_2 1–0S(1) velocity field appears to be greater is due primarily to the change in velocity gradient in a $0.3''$ strip along the western edge of the map; excluding this region, the difference between the maps is statistically insignificant (see Figure 2.7 right image). The western region coincides with the extension of emission in the H_2 1–0S(1) flux map and seems likely to be associated with a molecular outflow in (or at the edge of) the ionisation cone, perhaps radiatively driven by the AGN. It is important to notice that the observed velocity field of the $\text{Br}\gamma$ line is clearly different to the one expected if it was associated with the NLR of the AGN, which would exhibit an increase in velocity in the western direction along the minor axis of the galaxy, as an outflow in the ionisation cone.

By correcting the velocity maps for inclination ($i = 65^\circ$), we find a rotation velocity of 75 km s^{-1} at 8 pc from the nucleus. The velocity dispersion of the stars in the nuclear region is almost constant with a value of $\sigma_{\text{obs}} \approx 80 \text{ km s}^{-1}$. By correcting the measured dispersion for the instrumental resolution corresponding to $\sigma_{\text{inst}} \approx 32 \text{ km s}^{-1}$, we obtain an intrinsic dispersion of $\sigma_z \approx 70 \text{ km s}^{-1}$, yielding a velocity to dispersion ratio of $V_{\text{rot}}/\sigma_z \approx 1.1$. This ratio suggests that while there is significant rotation, random motions are also important – and on these scales perhaps dominant. Indeed, the kinetic energy in random motions is of order $3\sigma^2$ while that in the ordered rotation is V_{rot}^2 . This would imply that the distribution of gas is rather thick – consistent with our suggestion in Section 2.5 that the symmetry of the observed isophotes is due to the physical height of the nuclear region.

Further evidence that this is the case comes from the scale height derived if one assumes that the gas and stars are self gravitating, although this should only really be applied to a thin disk. In this case

$$\sigma_z^2 = 2\pi G \Sigma z_0 \quad (2.5)$$

where σ_z is the velocity dispersion of the stars, Σ is the surface density of the disk, and z_0 is a characteristic measure of the scale-height of the disk perpendicular to the plane. In the nuclear region at $R < 0.4''$ (8 pc), we estimate the mass of the gas and the stars residing in the disk to be $1.7 \times 10^7 M_\odot$ (see also Section 2.7), yielding a mean surface density of $\Sigma = 8.5 \times 10^4 M_\odot \text{ pc}^{-2}$. By considering an intrinsic $\sigma_z = 70 \text{ km/s}$, we obtain a height of $z_0 = 2 \text{ pc}$, consistent with our earlier estimate based on the isophotal symmetry.

We suggest that this thickness does not necessarily imply that there is a distinct spheroidal structure in the central few parsecs; but that we are only looking at the very inner region of a larger disk which extends out perhaps as far as circumnuclear ring. By measuring the rotation velocity within a truncated field of view – i.e. before V_{rot} reaches its asymptotic value – one would underestimate V_{rot}/σ . It is also possible that either dynamics associated with the black hole, or heating from the AGN or local intense star formation, have caused the inner region of the disk to thicken.

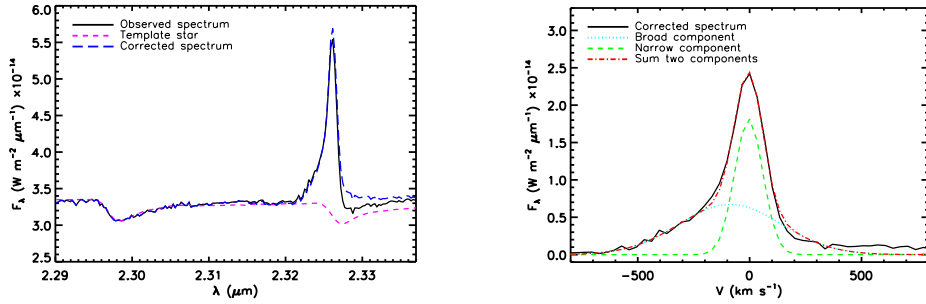


Figure 2.8: *Left panel* Nuclear spectrum around [CaVIII] to show how the stellar continuum was subtracted. *Right panel* [CaVIII] profile in velocity space, fitted by two gaussians.

For systems where the velocity dispersion is significant, estimating the mass from the rotational velocity alone leads to an underestimate. Accounting for random motions is not trivial, but can be approximated by $M_{\text{dyn}} = (V_{\text{rot}}^2 + 3\sigma^2)r/G$. Hence we obtain a dynamical mass for the nucleus within $\pm 0.4''$ of $M_{\text{dyn}} = 3.5 \times 10^7 M_{\odot}$.

2.7 Dimensioning the clumpy star forming torus in Circinus

The spatial scales on which we have traced the gas and stars are similar to those associated with standard torus models (e.g. Pier & Krolik 1992; Pier & Krolik 1993; Nenkova et al. 2002, Schartmann et al. 2005, Fritz et al. 2006). Indeed, the latter two authors have modelled Circinus specifically and find size scale for the torus of 30 pc and 12 pc respectively. However, to understand better the relation between the gas and the stars, we need, in addition to the stellar mass found in Section 2.5, to estimate the gas mass. Fortunately, as we discuss below, there is a way to do this from our data.

Table 2.2 lists 17 galaxies for which there are in the literature both measurements of the H_2 1–0S(1) line flux and estimates of the total gas mass from mm CO 1–0 or CO 2–1 luminosities. The H_2 1–0S(1) luminosities are primarily from Goldader et al. (1997), since these are taken in large ($3''$ or more) apertures and therefore are more likely to include all, or nearly all, the H_2 1–0S(1) flux. In addition, these galaxies are actively star forming – as evidenced by their classification as luminous or ultraluminous galaxies. As the table shows, nearly all of these have similar ratios of the 1–0S(1) luminosity with the infrared luminosity L_{IR} , and also with the molecular mass estimated from the CO luminosity L_{CO} . The former relation has previously been noted by Goldader et al. (1997), who suggested it could be explained in terms of supernova remnants if the H_2 originates in gas shocked by the expanding shells.

On the other hand, Davies et al. (2003) argued that in general the H_2 1–0S(1) line in such galaxies is excited by fluorescence by young stars of gas dense enough that the lower vibrational levels are thermalised. In either case, if the H_2 emission is primarily associated with star formation, it would not be unreasonable to find a correlation with L_{IR} .

Similarly, a correlation between L_{IR} and L_{CO} has been known for a long time (see Young & Scoville 1991 for a review). Recent work (Gao & Solomon 2004) shows that while L_{IR} and L_{CO} are correlated, the logarithmic relation is linear only over limited luminosity ranges and there is a clear trend of $L_{\text{IR}}/L_{\text{CO}}$ (i.e. star formation efficiency) with luminosity. They also showed that if one uses instead a tracer of dense gas such as HCN, the equivalent ratio $L_{\text{IR}}/L_{\text{HCN}}$ is constant; although for our application one then has the difficulty of estimating the gas mass from the L_{HCN} .

In both relations, NGC 6240 is a major exception, having by far the largest H_2 1–0S(1) luminosity. The reason is most probably that the H_2 and CO emission come from a large scale, global shock which is not virialized such that there is lots of H_2 and CO emission but relatively little underlying gas (Tacconi et al. 1999). For this reason, we have excluded NGC 6240 from the sample.

Given the correlations above, it would not be unreasonable also to expect a relation between 1–0S(1) luminosity and H_2 mass as traced by the CO luminosity (or even better would be HCN luminosity). In fact we find that the logarithmic ratio of these two quantities is $\log \frac{L_{(1-0)\text{S}(1)}}{M_{\text{gas}}} = -3.6 \pm 0.32$ which corresponds to $\sim 2.5 \times 10^{-4} L_{\odot}/M_{\odot}$ with a 1σ uncertainty of a factor 2. This is a quite remarkable result for such a diverse sample – that includes galaxies with powerful AGN for which X-ray irradiation of gas may be an important contributor to the 1–0S(1) luminosity. It gives us confidence that we can use the H_2 1–0S(1) line, without needing to know the details of how it is excited, to make at least an approximate estimate of the total (cold) molecular gas mass.

We apply this result to the nuclear region of Circinus because it has had recent vigorous star formation close to the AGN, and thus matches the sample. From the total H_2 1–0S(1) luminosity of $4.4 \times 10^3 L_{\odot}$ we estimate the total molecular mass to be $1.7 \times 10^7 M_{\odot}$ – fully consistent with the dynamical mass estimated in Section 2.6. The gas mass surface density is then $8 \times 10^4 M_{\odot} \text{pc}^{-2}$, yielding a column density of $n_{\text{H}} = 5.2 \times 10^{24} \text{cm}^{-2}$, which is very similar to that implied by X-ray observations (e.g. Matt et al. 1999). Since $n_{\text{H}} \approx 1.5 \times 10^{21} \tau_{\text{V}}$, the mean gas density implies an optical depth through the thickness of the disk of $\tau_{\text{V}} = 3000$. This is far larger than the most likely values estimated in Section 2.5, and also inconsistent with the maximum possible optical depth.

This discrepancy suggests that the canonical torus in the unified model of AGN is not only forming stars but is a clumpy medium – so that much of the star light is not obscured despite the presence of huge gas column densities.

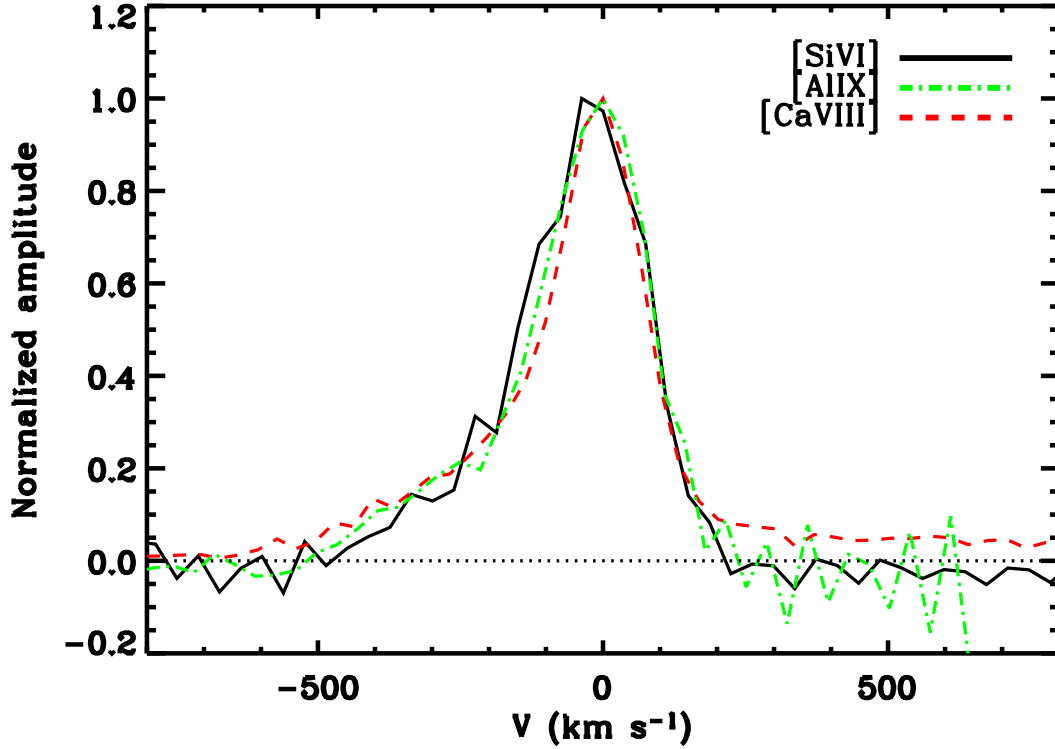


Figure 2.9: Comparison of coronal line profiles in velocity space.

2.8 Coronal lines

Because of the high ionization potential ($IP > 100$ eV) associated with Coronal Line Region (CLR) emission lines, highly energetic processes are required. The lines can be excited either by a hard UV to soft X-ray continuum, very hot collisionally ionized plasma, or a combination of both. If the excitation occurs via collisions, the gas temperature should be about $T = 10^6$ K. In the case of photoionization via the hard AGN continuum, temperatures of only a few $10^3 - 10^4$ K are needed.

In our observations of Circinus the [SiVI], and [CaVIII] lines are extremely strong and [AlIX] is also detected, as apparent in the spectrum in Figure 2.1. Due to the low signal to noise ratio of the K -band spectrum after $2.42 \mu\text{m}$, we exclude the [SiVII] line at $2.48 \mu\text{m}$ studied by Prieto et al. (2005). From this spectrum and also that in Figure 2.8, it can be seen that the [CaVIII] line sits on top of the stellar $^{12}\text{CO}(3-1)$ absorption bandhead. A template star (HD 179323, shifted to the redshift of Circinus) was used to correct the stellar features in the spectrum and hence reconstruct the full [CaVIII] line profile. As the deep CO bandheads are produced in the atmospheres of red (super)giant stars which dominate the emission around $2.3 \mu\text{m}$, HD 179323

(spectral type K0Iab) was chosen for this purpose. The correction was achieved by convolving the template with a Gaussian broadening function, and varying its parameters to minimise χ^2 , which was measured across the ^{12}CO (2-0) bandhead. The ^{12}CO (3-1) bandhead of the template was then convolved with the broadening function and subtracted from the galaxy's spectrum.

Figure 2.9 shows that in all three coronal line profiles we observe asymmetric and broadened lines, indicating the presence of two or more components within the coronal line region. In order to quantify the profile, we have fitted a superposition of two Gaussians to each line, as is summarised in Table 2.3. As can be seen in Figure 2.8 for the case of [CavIII], there is a strong narrow component and a weaker blueshifted broad component. These also have different spatial extents. Figure 2.10 shows azimuthally averaged radial profiles of the broad and narrow components of this line, as well as the PSF. It is clear that the broad component is resolved and spatially more extended. The flux peaks at about 1.5 pc from the nucleus. On the other hand, the narrow component is unresolved and most of its flux comes from a region of less than 1 pc across and coincident with the non-stellar K -band continuum peak (rather than the peak in $\text{Br}\gamma$, H_2 1-0S(1), and stellar continuum). These characteristics suggest that they originate in different regions around the AGN, and perhaps are even excited by different mechanisms.

In the case of the narrow component, the fact that it is compact and centered on the nucleus suggests that it originates physically close to the AGN. Since the lines are narrow and at systemic velocity, these clouds of ionized material are not out-flowing which is also an indication that they are excited by photoionization (Oliva et al. 1994; 1999).

In the case of the broad component, the fact that it is blue shifted indicates that part of the gas must arise in outflows around the AGN, as has been suggested by Rodríguez-Ardilla et al. (2004). Previous work on the coronal line emission in Circinus (Oliva et al. 1994) had ascribed the excitation to photoionisation. This was in part due to the narrow width of the most prominent component (typically 175 km s^{-1} , from Table 2.3). However, the considerable broadening associated with the blue wing ($\text{FWHM} > 300 \text{ km s}^{-1}$) opens the possibility that some fraction of it might in fact be excited by fast shocks. The picture of a shock-excited blue component is supported by the results of Prieto et al. (2005), who suggested that in addition to photoionization, shocks must contribute to the coronal emission. They proposed shock excitation as an additional energy source to explain the extended coronal line emission, as traced by [SivII], in a sample of 4 nearby Seyfert 2 galaxies. Although it could be a single broad component, we consider a more likely scenario to involve many narrow components arising from different clouds moving at different velocities whose emission combines to produce the observed morphology and profile. A mechanism by which broad coronal lines are created in out-flowing cloudlets which have been eroded from the main clouds is an interpretation which has been proposed for the detailed morphological and kinematic data available for NGC 1068 (Cecil et al. 2002).

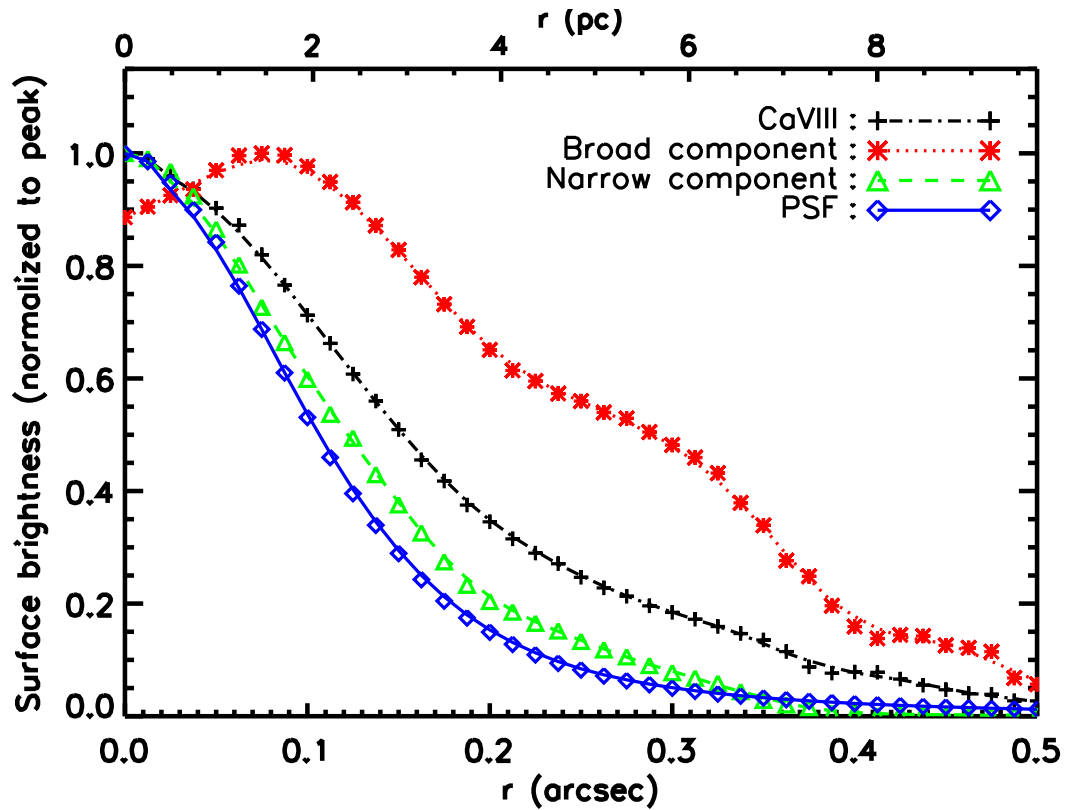


Figure 2.10: Radial profile of the surface brightness of the [CaVIII] broad component (asterisks connected by a dotted line), and [CaVIII] narrow component (open triangles connected by a dashed line), compared to the [CaVIII] profile (crosses connected by a dotted-dashed line) and the PSF profile (open diamonds connected by a solid line).

Line	IP (eV)	Component	Flux ($\text{W m}^{-2} \times 10^{-18}$)	$F_{\text{broad}}/F_{\text{narrow}}^a$	Velocity ^b (km s^{-1})	FWHM Line Width (km s^{-1})
(1)	(2)	(3)	(4)	(5)	(6)	(7)
[SiVI]	167	Broad	26.8		-103	300
[SiVI]	167	Narrow	24.7	1.1	~ 0	175
[AlIX]	285	Broad	2.6		-228	300
[AlIX]	285	Narrow	8.2	0.3	~ 0	200
[CaVIII]	127	Broad	28.0		-87	540
[CaVIII]	127	Narrow	20.0	1.4	~ 0	150

^a The ratio for each line is written in the row of the narrow component.

^b Velocity shift from the systemic velocity.

Table 2.3: Properties of the broad and narrow components of the detected coronal lines.

It is interesting that we observe a correlation between the IP and the blueshift, as well as the $F_{\text{broad}}/F_{\text{narrow}}$, of the forbidden lines. As the ionization potential increases, the blueshift also increases and the $F_{\text{broad}}/F_{\text{narrow}}$ decreases. This can be understood if the acceleration of cloudlets away from the AGN is driven impulsively (which one might expect given the enormous variability of hard X-ray luminosity in many AGN) so that the cloudlets with the highest velocities will also be closest to the AGN – and as they travel further out, they will be decelerated by drag against the interstellar medium (probably small in the ionisation cone) and by the increasing gravitational pull. The gravitational pull is significant since it depends not only on the black hole mass, as assumed by Maiolino et al. (2000), but also on the gas and stars in the nuclear region which we have shown provide an order of magnitude more mass than the black hole alone on scales of 10 pc. Additionally, those lines which required the hardest ionising continuum will arise preferentially closer to the AGN. Thus although the strength of the narrow component which originates close to the AGN will depend on IP since there are fewer photons energetic enough to ionise species with higher IP; it will be even harder to create these lines in outflowing cloudlets, since they are already further from the AGN: they will arise only in the fastest clouds closest to the AGN. Lines with less extreme IP will be generated also in slower clouds further from the AGN and hence the mean blueshifted velocity will be less. Although we do not find a clear correlation between the IP and the width of the fit to the broad component, that of the [CaVIII] line exhibits the highest dispersion for the lowest IP, providing further support for this hypothesis that lines with the lower IP can arise in regions which are further from the AGN and hence moving outward slower.

2.9 Conclusions

We have presented near-infrared adaptive optics integral-field spectroscopy of the nuclear region of the Circinus galaxy with an angular resolution of $0.2''$ and spectral resolution $R \sim 4200$, which we use to probe the gas and stellar morphologies and kinematics on scales of a few parsecs.

In the central $0.8''$, the non-stellar continuum dominates the K -band, contributing 85% of the total flux density. Offset by $\sim 0.15''$ from its peak are the H_2 1–0S(1) and $\text{Br}\gamma$ lines and stellar continuum. The similarity of their morphologies and kinematics lead us to conclude that they all originate predominantly with recent vigorous star formation. Analysis of these diagnostics together with the radio continuum suggest that within 8 pc of the AGN there is a starburst which is exponentially decaying on a timescale of 100 Myr and began only 80 Myr ago, and currently has a bolometric luminosity of $\sim 1.4\%$ that of the entire galaxy.

Adopting a conversion factor of $L_{(1-0)\text{S}(1)}/M_{\text{gas}}$ derived from measurements of actively star-forming galaxies on scales of $\sim 3''$ to the circum-nuclear region of Circinus, we have found that the total gas mass is an order of magnitude more than the young stars, and also consistent with the column densities to the AGN implied by X-ray

observations. Since the scales on which the gas and stars exist are similar, we suggest that the torus is forming stars; and because of the limits on extinction to the stars, that the torus must be a clumpy medium rather than uniform.

The coronal lines comprise two components: a prominent narrow (FWHM $\sim 175 \text{ km s}^{-1}$) part which is at systemic velocity, spatially unresolved (at our 4 pc FWHM resolution), and centered on the non-stellar continuum; and a broad (FWHM $> 300 \text{ km s}^{-1}$) blue shifted part which is spatially extended. We argue that the narrow part arises in clouds physically close to the AGN; and that the blue wing originates, as appears to be the case in some other Seyfert galaxies, from cloudlets that have been eroded from the main clouds and are accelerated outward.

Chapter 3

A molecular gas streamer feeding and obscuring the active nucleus of NGC1068

This chapter is an almost exact reproduction of the following publication:

- “Molecular gas streamers feeding and obscuring the active nucleus of NGC1068”
Müller Sánchez, F., Davies, R. I., Genzel, R., Tacconi, L.J., Eisenhauer, F.,
Hicks, E., Friedrich, S., & Sternberg, A. 2008a, ApJ, submitted

3.1 Introduction

A detailed description of the distribution and kinematics of the molecular gas in the central region of Seyfert galaxies is crucial for understanding the fueling of the nucleus and the role of gas in obscuring the active galactic nucleus (AGN). NGC1068, at a distance of 14.4 Mpc (Bland–Hawthorn et al. 1997), is the brightest Seyfert 2 galaxy and therefore one of the best candidates for direct investigations of the morphology and dynamics of the molecular gas neighboring an active nucleus. The idea of a rotating molecular/dusty torus surrounding a supermassive black hole emerged from the interpretation given by Miller & Antonucci (1983) of optical spectropolarimetry of precisely this galaxy, which revealed scattered type–I emission from the obscured broad-line region (BLR). Since then, several near- and mid-IR observations have in fact found and begun to elucidate the physical conditions of the concentration of molecular gas and dust in the nucleus of NGC1068 (near-IR: Young et al. 1996; Marco et al. 1997; Rouan et al. 1998, 2004; Alloin et al. 2001; Galliano & Alloin 2002; Galliano et al. 2003; Weigelt et al. 2004; Wittkowski et al. 2004; Gratadour et al. 2005, 2006; mid-IR: Bock et al. 2000, Tomono et al. 2001, 2006; Jaffe et al. 2004; Galliano et al. 2005; Mason et al. 2006; Poncelet et al. 2006, 2007), all favouring indirectly the existence of a compact molecular/dusty torus but failing to obtain a clear image of it. Alternatively, by means of mid-IR observations over the central 140 pc ($2''$), Cameron et al. (1993) proposed a model in which the bulk of the molecular gas and dust is located at large distances (several tens of parsecs) from the AGN. Line-of-sight attenuation of the BLR in this case would be a mere consequence of one or more intervening molecular clouds. More recently, Jaffe et al. (2007) have analyzed new interferometric mid-IR observations of NGC1068 and found that the fitted Gaussian components to the (u, v) plane of the central $10 \mu\text{m}$ source resemble a disk similar to the H_2O masers (Greenhill et al. 1996). Both, the dust and H_2O maser disks, appear to be oriented neither perpendicular to nor aligned with the radio jet. However, one needs to be cautious when interpreting all of these observations. As they are measurements of the continuum emission, the inferred gas/dust distributions are strongly dependent on temperature, tracing in fact radiation of matter at a given temperature rather than spatial gas/dust distributions.

The $2.122 \mu\text{m}$ H_2 rovibrational $\nu = 1-0\text{S}(1)$ emission line probes hot ($\geq 10^3$ K) and moderately dense ($\geq 10^3 \text{ cm}^{-3}$) molecular gas and as such, may be an excellent tracer of gas in the nuclear region. Its spatial distribution can expose the potential presence of a molecular/dusty torus, and also provide physical information on fueling or feedback mechanisms. Imaging spectroscopy of this line (Rotaciuc et al. 1991; Blietz et al. 1994) has indicated the presence of significant amounts of hot, dense, circumnuclear molecular gas extending over the central 4 arcseconds which is associated with the narrow-line clouds. The nuclear region shows a strong peak almost $1''$ east of the nucleus and a weaker one $\sim 1''$ to the west. Furthermore, the H_2 emission at a few arcseconds from the nucleus is more extended along the major axis of

the bar (Davies et al. 1998). More recently, Galliano & Alloin (2002) obtained 2D spectroscopic observations of the warm molecular gas in the central $4'' \times 4''$ of the galaxy. They did not detect H_2 emission at the location of the K -band continuum core (which is known already to be coincident with the central engine at these scales), but instead they confirmed the two main regions of H_2 emission at about $1''$ east and west of the nucleus along a $\text{PA}=90^\circ$, and a region with complex line profiles at ~ 50 pc north of the AGN. They interpreted the observed H_2 emission at these scales in terms of a warped disk consistent with the interpretation given by Schinnerer et al. (2000) to the millimeter interferometer maps of $^{12}\text{CO}(2-1)$ emission. It is now apparent from recent SINFONI H_2 1-0S(1) data at these scales that simple warped disk models of the molecular gas (Schinnerer et al. 2000; Baker 2000) cannot account for the fantastic variety and detail in the morphological and kinematical structure (see Davies et al. 2006), in particular since there is a considerable amount of gas inside the inner edge of the 100 pc ring.

In order to analyze in detail the physical conditions of the warm molecular gas in the central region of an active nucleus, we have obtained adaptive optics assisted SINFONI integral field spectroscopic data to peer deeply into the energetic core of NGC1068. In this paper we focus on the observations of the molecular gas emission in the central arcsecond of the galaxy done with the smallest spatial scale of the instrument, resulting in a resolution of 75 milli-arcseconds, approximately 7 times better than previous observations. We refer to Müller Sánchez et al. 2008b for the analysis of the stars, molecular and ionized gas in the central $3''$ of the galaxy corresponding to the rest of the results from the SINFONI observations of NGC1068.

3.2 Observations

The data presented here were obtained during 2005–2006 using the adaptive optics assisted near-infrared integral field spectrograph SINFONI (Bonnet et al. 2004, Eisenhauer et al. 2003b) on the VLT UT4. SINFONI delivers spectra simultaneously over a contiguous two-dimensional field of 64×32 pixels. The data were taken in the $H + K$ -bands using two of the three possible spatial pixel scales of the instrument: $0.0125'' \times 0.025''$ and $0.05'' \times 0.1''$

The $0.0125'' \times 0.025''$ SINFONI data were taken in two sets of 2 and 1.5h integrations on the nights of 21 October 2005 and 27 November 2006, both using the galaxy nucleus as reference for the MACAO adaptive optics system. In both nights the atmospheric conditions were excellent (optical seeing of the two nights was $\sim 0.7''$ and $\sim 0.5''$ respectively), which allows us to obtain a resolution of $0.075''$ FWHM as measured from the spatially marginally resolved non-stellar continuum in K -band. The $0.05'' \times 0.1''$ data were obtained on 6 October 2005. Once more, the AO module was able to correct on the nucleus of NGC1068 in seeing of $0.63''$, to reach $\sim 0.1''$ spatial resolution. In this case, a total of 4 sky and 8 on-source exposures of 50 sec each, were combined to make the final data cube. For the $0.0125'' \times 0.025''$ and

0.05" \times 0.1" datasets, the spectrograph was able, in a single shot, to obtain spectra covering the whole H and K -bands (approximately 1.45 – 2.45 μm) at a spectral resolution FWHM of 125 km s $^{-1}$ (R \sim 2400) for each pixel in the 0.8" \times 0.8" and 3.2" \times 3.2" field of view.

The data were reduced using the SINFONI custom reduction package SPRED (Abuter et al. 2005). This performs all the usual steps needed to reduce near infrared spectra, but with the additional routines for reconstructing the data cube. Flux calibration was performed simultaneously in H and K -bands using a G2V star HD20339 ($H = 6.45$, $K=6.41$), which yielded in a 1" aperture a K -band magnitude for NGC1068 of 7.73 and H -band magnitude of 10.18. The values we deduced are consistent, at similar and smaller apertures, with values found in previous studies (Rouan et al. 1998; Gratadour et al. 2006; Prieto et al. 2005). In addition, flux calibration was cross-checked with VLT NACO data in 2 – 4" apertures (Müller Sánchez et al. 2008b). The NACO data was further cross-checked in larger 5 – 10" apertures using 2MASS data. Agreement between the different data sources was consistent to 15%.

3.3 Distribution, kinematics and physical properties of the molecular gas

3.3.1 Molecular gas morphology

The molecular hydrogen emission at scales of a few arcseconds from the nucleus has been mapped previously reaching spatial resolutions down to $\approx 0.5''$ (Galliano & Alloin 2002). Our SINFONI data at these scales reach $\sim 0.1''$ resolution and reveal a complex distribution of the gas which has not been entirely observed before (Figure 3.1). The new data resolve the previously studied H $_2$ knots and show the presence of an off-center ($\Delta r = 0.6''$ SW from the AGN) ring of molecular gas (see Fig. 3.9), as well as apparently linear gas streamers leading from the ring NNW and SSE to the center. In addition, the overlay of our H $_2$ flux map and the $^{12}\text{CO}(2-1)$ map from Schinnerer et al. (2000) at these scales (Figure 3.1) shows a very good correlation, confirming that gas distributions can be traced either by the 2.122 μm H $_2$ 1-0S(1) emission line (hot gas) or the $^{12}\text{CO}(2-1)$ emission (cold gas). We discuss briefly the morphology of the ring in Section 3.3.6 but refer to Müller Sánchez et al. (2008b) for more analysis and discussion of these results. In the following we will concentrate on the central arcsecond (white box in Figure 3.1) and provide a few remarks on the connection of the linear streamers to the circumnuclear environment.

The morphology of the H $_2$ 1-0S(1) emission in the central 0.8" \times 0.8" of NGC1068 with a resolution of 0.075" (~ 5 pc) is presented in Figure 3.2. The peak of the 2.1 μm non-stellar continuum is located at the origin of the image and is represented by a crossed circle. At these scales this can be identified as the position of the central

engine (Galliano et al. 2003). At larger scales, a linear structure leading to the AGN from the NNW and SSE is the only noticeable feature in this whole region (see Figure 3.1). On sub-arcsecond scales near the AGN, this linear structure exhibits two prominent regions of H₂ emission, one overlapping the center of the non-stellar continuum, and another one located $\sim 0.35''$ north of this point.

Thanks to improved spatial resolution and sensitivity, molecular gas is now detected closer and closer to the AGN, in contrast to previous observations (Galliano & Alloin 2002). In Figure 3.3, we show a spectrum of NGC1068 at a spectral resolution of $R \sim 2400$, integrated over a $0.3'' \times 0.1''$ rectangular aperture centered at the position of the nucleus; although the continuum is quite strong in this region, the H₂ 1–0S(1) line is clearly seen. We will refer to this nuclear concentration of gas as the *southern tongue*. It has a major axis of ~ 17 pc and a minor axis of ~ 7 pc and is elongated to the south following the SSE extension of the linear structure. Its major axis has a position angle of about 120° , similar to that of the H₂O maser disk (Greenhill et al. 1996) and the $10 \mu\text{m}$ dust emission (Jaffe et al. 2004; Poncelet et al. 2007) on a scale of 20 mas. These three features exhibit the same misalignment with the major axis of the nuclear 5 GHz radio continuum (Gallimore et al. 2004). The H₂ 1–0S(1) luminosity of the southern tongue is $1.5 \times 10^{-18} \text{ W m}^{-2}$ ($\sim 1 \times 10^4 L_\odot$).

In addition to the nuclear component designated as the southern tongue, we found another area of high luminosity in the northern part of the H₂ intensity map (see Figure 3.2). In fact, this is the brightest region of the linear structure ($\sim 1.6 \times 10^4 L_\odot$) which extends up to $0.7''$ NNW of the central engine along a PA of -14° and connects to a prominent knot in the circumnuclear ring (Figure 3.1). We will designate this extension of the linear structure as the *northern tongue*. The region north of the AGN where apparently the northern tongue and the circum-nuclear ring merge is characterised by double-peaked line profiles (Galliano & Alloin 2002). As this region is out of the central arcsecond, we postpone the quantitative analysis of it to a subsequent publication (Müller Sánchez et al. 2008b). The H₂ line profiles of the small scale data studied here do not show complex morphologies and thus they were fitted by one Gaussian component as described in Sect. 3.3.2.

Dust emission at $12 \mu\text{m}$ from the northern tongue is present in previous mid-IR observations by Bock et al. (2000), Tomono et al. (2006) and Poncelet et al. (2007). Overlays of our two H₂ flux maps at different spatial scales and the $12.5 \mu\text{m}$ deconvolved image of Bock et al. (2000) are shown in Figure 3.4. The image taken at $12.5 \mu\text{m}$ has the highest angular resolution and highest signal to noise ratio of the mid-IR images from Bock et al. (2000). For these reasons we have chosen to compare this image with our flux maps, in a similar way as these authors did with other datasets. We want to emphasize, however, that all mid-IR images, show qualitatively the same features. In both panels of Figure 3.4 we assumed that the mid-IR peak is located at the position of the nucleus as defined by the near-IR peak. As can be seen in the two overlays, along the northern tongue there exists good correlation between the molecular gas emission and the $12.5 \mu\text{m}$ continuum. In the

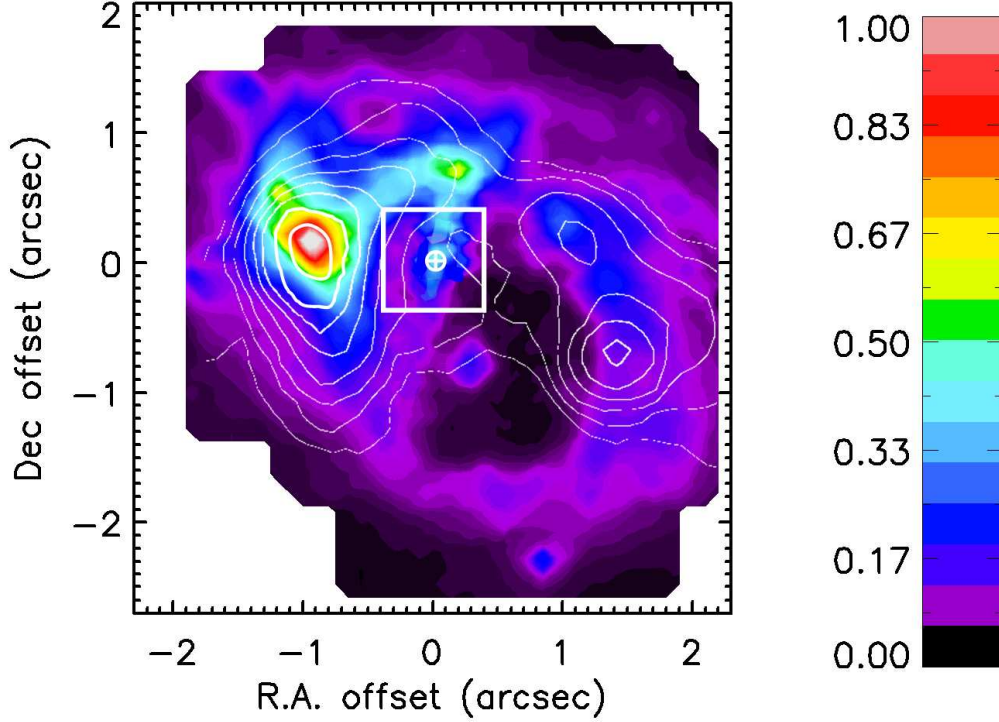


Figure 3.1: SINFONI H_2 1–0S(1) flux map of the central region of NGC1068 at a resolution of $0.1''$. A contour plot of the $^{12}\text{CO}(2-1)$ emission map from Schinnerer et al. (2000) is overlaid on the H_2 flux map. The scale is given in arcsec ($1'' = 70$ pc). The position of the nucleus as defined by the near-IR non-stellar peak is represented by a crossed circle. In addition to the previously known prominent gas concentrations $\sim 1''$ east and west of the nucleus, the morphology reveals several new distinct structures. One of them is a complete ring centered $\sim 0.6''$ SW of the nucleus. The other is a linear structure apparently emanating from the expanding ring and connecting to the AGN along a PA of $\sim -14^\circ$. This new linear streamer is the focus of the discussion in this paper. The central square emphasize the location of this linear structure and denotes the field of the small scale observations shown in Figures 3.2 – 3.8.

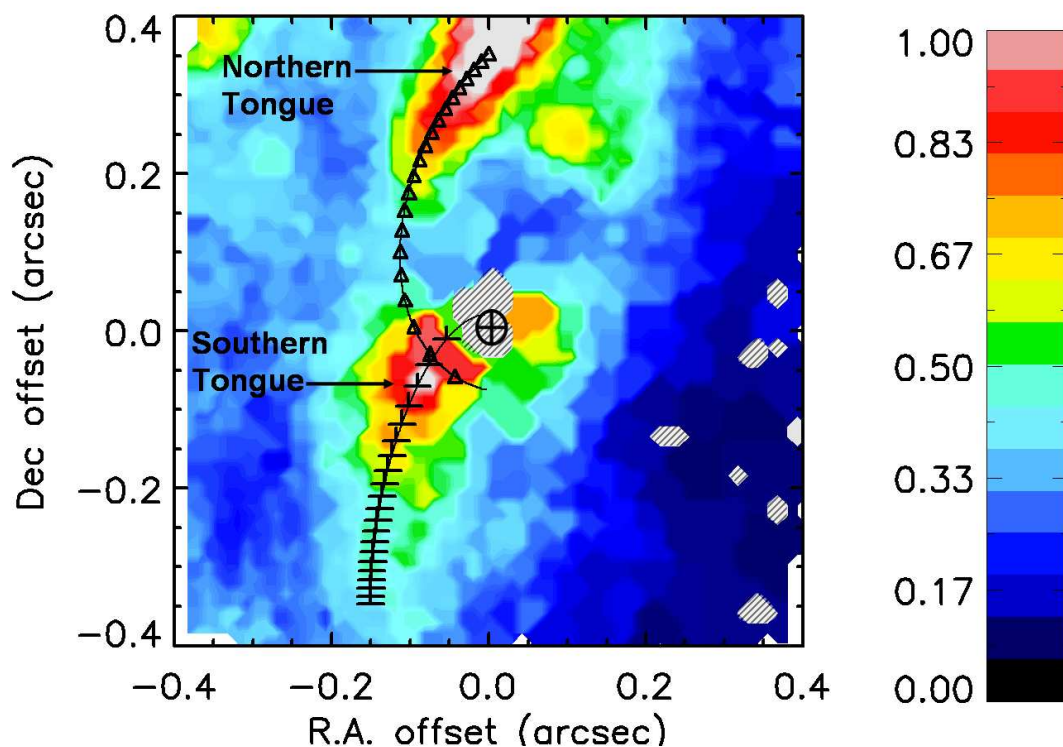


Figure 3.2: Flux map of the H₂ 1-0S(1) emission in the central $\pm 0.4''$ of NGC1068 with a resolution of $0.075''$ (~ 5 pc). The peak of the non-stellar continuum is represented by a crossed circle. The image is binned using Voronoi tessellations (Capellari & Copin 2003). The line properties could not be extracted in the very central region around the AGN due to the strong continuum emission. The bins where the line properties could not be extracted were masked out and correspond to the diagonal patterned regions. The open triangles show the projected trajectory of the northern concentration of gas (the northern tongue, Orbit NT2). The half-crosses show the past trajectory of the gas which is currently located in front of the AGN (the southern tongue, Orbit ST2).

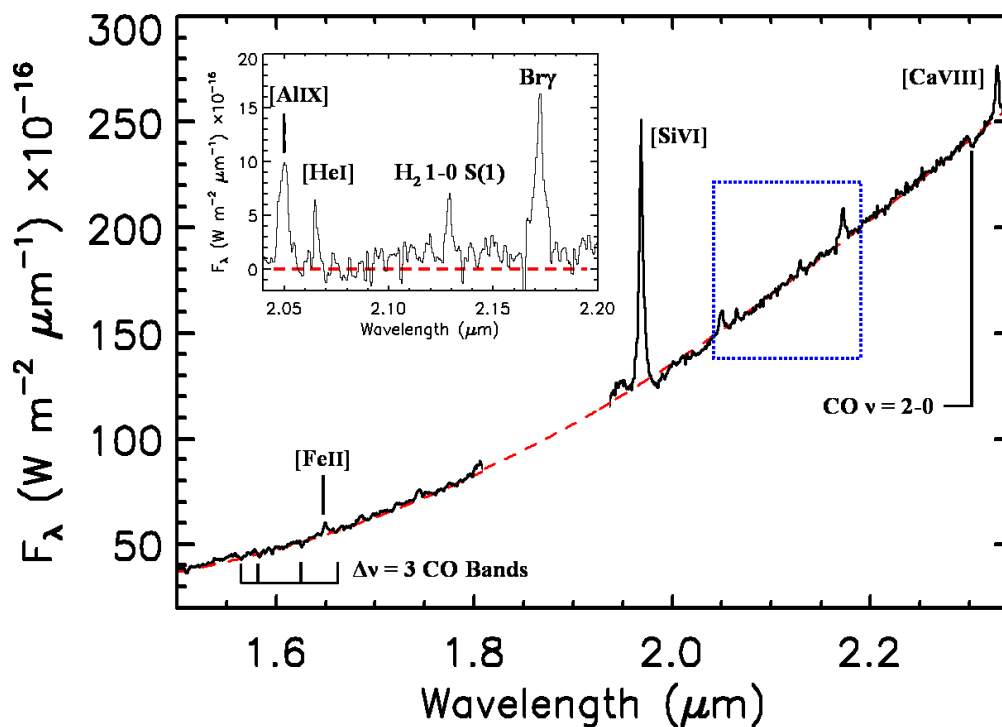


Figure 3.3: Integrated spectrum of the nucleus of NGC1068 in the wavelength range between 1.5 and 2.35 μm ($H + K$ -bands). The individual spectra were added over a $0.3'' \times 0.1''$ rectangular aperture centered at the position of the nucleus. The dashed line represents the best fitting curve to the continuum emission which corresponds to a black body radiating at 700 K. The dotted square emphasises the region between 2.05 and 2.20 μm , the wavelength range where the H_2 1-0S(1) emission line can be found. This region of the electromagnetic spectrum is plotted in the small panel top left. The continuum has been subtracted in this panel. The H_2 1-0S(1) emission line is clearly seen. Other relevant emission lines are indicated in the figure.

lower panel, a dashed line indicates the boundary of the northern tongue emphasising this correlation. Also, the alignment gives a fair correlation between the east-west unresolved mid-IR core and the H₂ southern tongue. The two overlays show a bend to the east, although the mid-IR bend is more pronounced. The qualitative agreement of the two images indicates that in the central arcsecond the molecular gas and the dust have a similar spatial distribution which is predominantly a north-south linear structure about 1'' (70 pc) long which contains two bright components: the southern and northern tongues. Our observations support the interpretation given by Tomono et al. (2006) suggesting that the northern tongue could be a passage that transports material to the central engine. We show for the first time, direct evidence from the gas kinematics that this is indeed what is occurring (see Section 3.3.2).

Finally, a comparison of the H₂ and 5 GHz flux maps is shown in Figure 3.5. Radio continuum imaging at 5 GHz with a resolution of 0.065'' revealed a number of structures along the inner part of the radio jet (Gallimore et al. 1996). Associating component S1 with the inner edge of the torus, these authors developed a scenario in which component C arises from a shock interaction between the jet and a dense molecular cloud. Supporting this hypothesis was the bend in the radio jet, the slightly flatter spectral index, and the presence of maser emission. Figure 3.5 shows that component C does in fact coincide spatially with the northern tongue of H₂ 1–0S(1) emission. Moreover, the $\nu = 1$ levels are thermalised, indicating that the gas is likely to be rather dense ($> 10^4 \text{ cm}^{-3}$). Thus the SINFONI data provide direct evidence for the molecular cloud and hence strongly support the jet-cloud interaction hypothesis.

3.3.2 Kinematic evidence for inflow

3.3.2.1 Detection of non-circular motions around the nucleus

We have extracted gas kinematics in the nuclear region of the galaxy from our integral field data, allowing for the first time a study of the gas motions on scales connecting the outer gas $r \sim 1''$ (~ 70 pc) ring to the maser disk at $r = 0.015''$ (~ 1 pc). Figure 3.6 shows the velocity and dispersion maps of the molecular gas in the central $0.8'' \times 0.8''$ of the galaxy. We have extracted the 2D kinematics by fitting a Gaussian convolved with a spectrally unresolved template profile (an OH sky emission line) to the continuum-subtracted H₂ 1–0S(1) spectral profile at each spatial pixel in the data cube. We performed a minimisation of the reduced χ^2 in which the parameters of the Gaussian (amplitude, center and width in velocity space) were adjusted until the convolved profile best matched the data. The uncertainties were boot-strapped using Monte Carlo techniques, assuming that the noise is uncorrelated and the intrinsic profile is well represented by a Gaussian (Davies et al. 2007). This method allowed us to obtain uncertainties for the velocity and dispersion in the range of $\pm(5 - 15) \text{ km s}^{-1}$. The dispersion extracted by this fitting procedure is already corrected for instrumental broadening.

The velocity field shown in Figure 3.6 is quite complex. There is no evidence of a

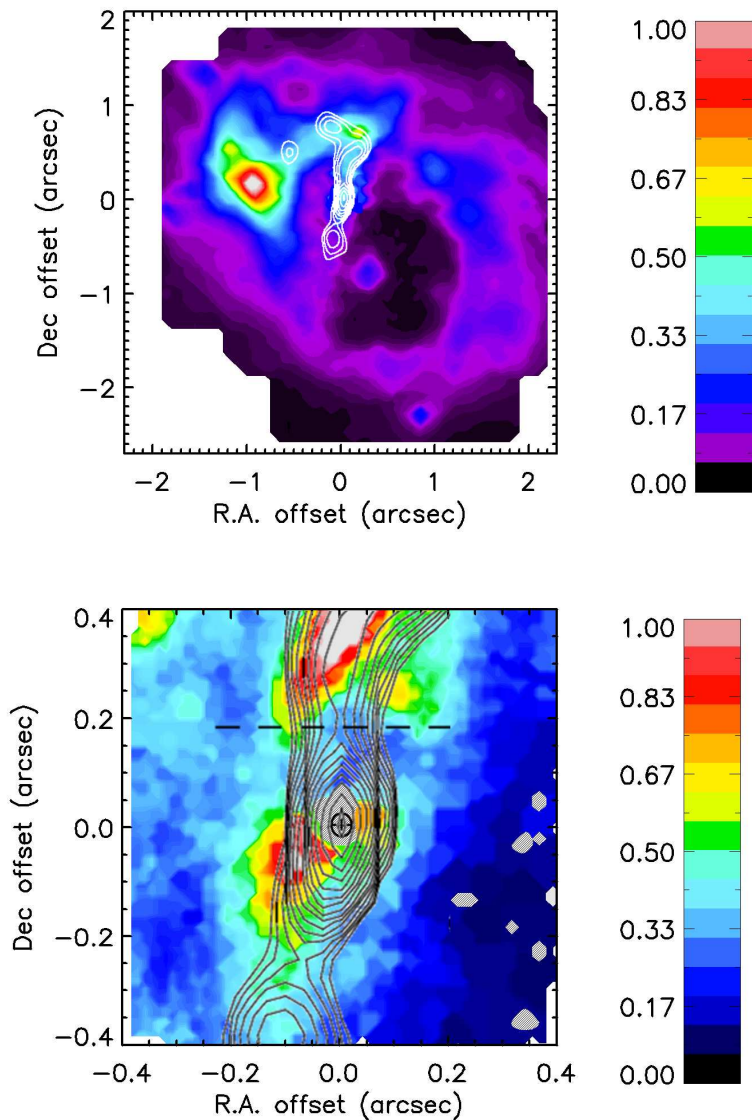


Figure 3.4: Contour plot of the $12.5\ \mu\text{m}$ deconvolved image of Bock et al. (2000) overlaid on the SINFONI H_2 1–0S(1) flux maps. The upper panel shows the overlay in the central $4'' \times 4''$ (mid-IR image in white contours) and the lower panel in the central $0.8'' \times 0.8''$ of NGC1068. The mid-IR centre is located at the position of the nucleus as defined by the near-IR peak. In the right panel the boundary of the northern tongue is denoted by dashed lines emphasising the good correlation between the two images.

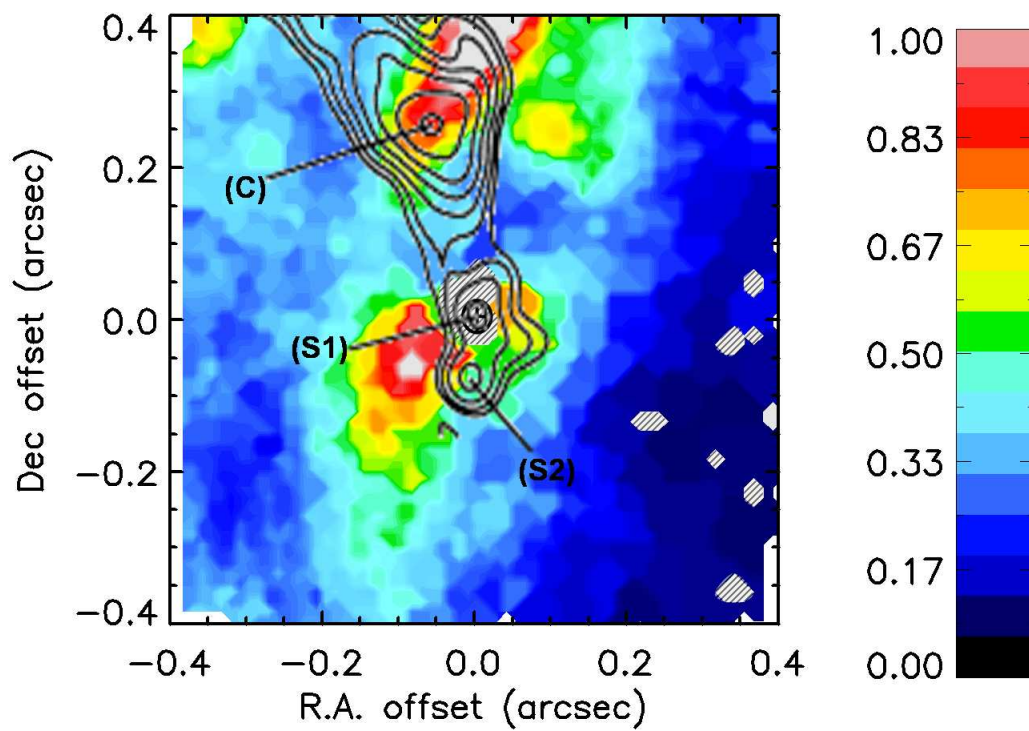


Figure 3.5: Morphology of the H₂ 1-0S(1) emission with the 5 GHz radio continuum overlotted in contours showing the position of the nucleus S1 and the jet-cloud interaction at the position of component C.

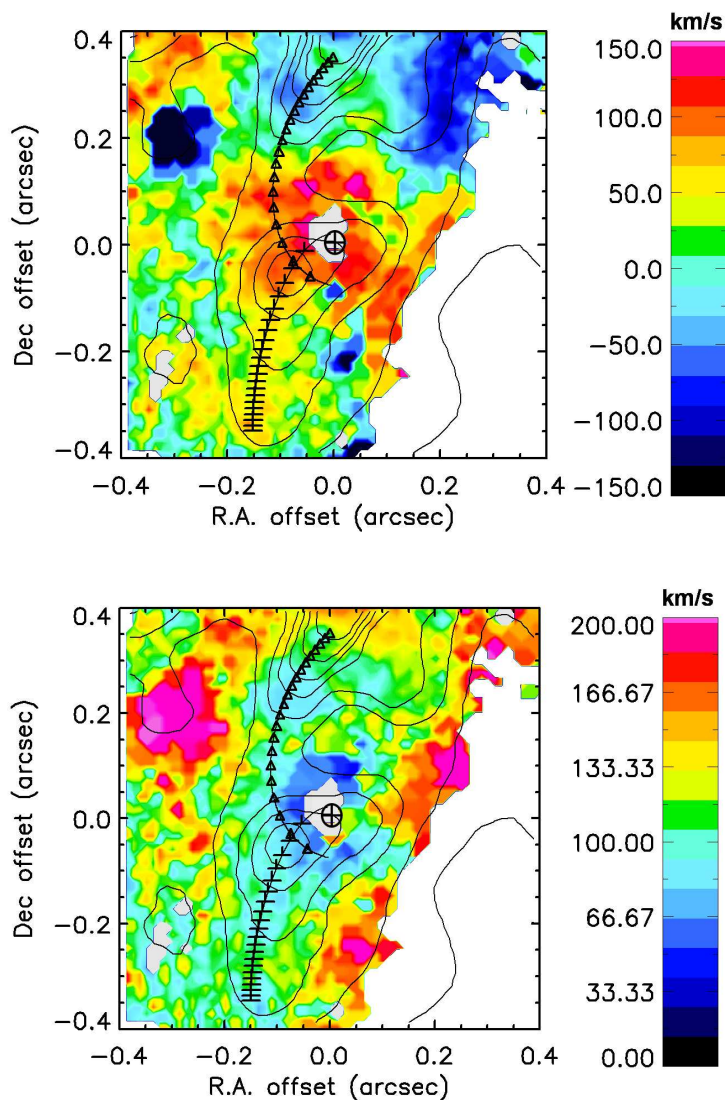


Figure 3.6: Velocity (up) and dispersion (down) maps of the molecular gas extracted from the SINFONI datacube in the central $\pm 0.4''$ of NGC1068. The dispersion has been corrected for instrumental broadening. A crossed circle indicates in each case the peak of the continuum emission. The maps are binned using Voronoi tessellations (Capellari & Copin 2003). The bins where the line properties could not be extracted were masked out and correspond to the white regions. The rejected pixels in both maps are those with a flux density lower than 10% of the peak of the central emission shown in Figure 3.2 and are shown in white in the right part of the fields. The open triangles show the projected trajectory of the northern concentration of gas (the northern tongue, Orbit NT2). The half-crosses show the past trajectory of the gas which is currently located in front of the AGN (the southern tongue, Orbit ST2).

rotating disk around the nucleus. Instead, one can distinguish three main kinematical components: blue-shifted material with almost constant projected velocity v_z of -25 km s^{-1} in the north, red-shifted projected velocities between $20 - 40 \text{ km s}^{-1}$ in the south-east, and a nuclear red-shifted component ($v_z \sim 90 \text{ km s}^{-1}$) associated with the southern tongue in Figure 3.2. Outside these regions the kinematics are not reliable due to the low strength of the line ($\leq 10\%$ of the flux as can be seen in Figure 3.2) and therefore they were masked out in the velocity and dispersion maps. The nuclear red-shifted kinematical component appears to be connected to the south-eastern kinematical component by a ridge of emission that gradually changes its projected velocity from $\sim 30 \text{ km s}^{-1}$ at $r = 0.4''$ to $\sim 90 \text{ km s}^{-1}$ at $r = 0.04''$ along a PA of -20° . This and the lack of a signature of rotation indicate that the gas must be streaming almost directly towards or outwards the nucleus rather than orbiting it on circular paths. Thus, any approach to reproduce the observed kinematics by a rotating or warped disk model can be excluded.

3.3.2.2 Quantitative modelling

To quantify the kinematics of the region we have modeled the observed velocities as motions of test particles under a gravitational potential comprising a central mass and an extended stellar component.

We define a three-dimensional cartesian coordinate system in the nuclear region of the galaxy with x -, y - and z -axes representing the Right Ascension, Declination and Line-of-Sight directions respectively. The gravitational potential well of the system is determined by a circum-nuclear mass distribution formed by the sum of a supermassive black hole of $M_{\text{BH}} = 1 \times 10^7 M_\odot$ (Greenhill et al. 1996) located at the origin of the system, and a stellar mass density $M_*(r) = 1 \times 10^6 r M_\odot \text{ pc}^{-1}$ (Davies et al. 2007; Müller Sánchez et al. 2008b). The gas clouds were modelled as test particles – i.e. they do not have any impact on the potential – with some initial conditions $x_0, y_0, z_0, v_{x0}, v_{y0}$ and v_{z0} . The initial x_0, y_0 and v_{z0} components of a test particle are obtained directly from the SINFONI data. Thus, the kinematic model contains three degrees of freedom corresponding to the other three Cartesian components z_0, v_{x0} and v_{y0} . Notice that v_{z0} can be considered also a variable due to the uncertainty in the observed projected velocities of $\pm 10 \text{ km s}^{-1}$. Once the phase space conditions of a cloud are given, the position and velocity of the cloud moving according to the Newtonian laws of motion under the influence of the assumed potential were determined at every time interval $\Delta t = 10 \text{ yr}$ over a period of 5 Myr. Therefore, this method creates free unperturbed Keplerian orbits fully defined by the initial values of the Cartesian components of the particle’s position and velocity.

We followed a systematic approach for the determination of the Keplerian orbits of the gas particles. First, an initial position vector r_0 was located inside a volume defined by the field of view and several z_0 components ranging from -60 pc to 60 pc . This interval was defined as two times the x - or y - range. It is important to point

out that this volume delineates the boundaries of the initial position vectors. The resulting orbits are actually contained in a spherical volume of indefinite radius. For each r_0 numerous sets of velocity vectors were investigated. The initial v_{z0} component of a particle at any given position in space corresponds basically to the observed projected velocity at that particular spot. The tested values for v_{x0} and v_{y0} at each point in space were dependent on r_0 and ranged from $-\sqrt{2GM_{\text{BH}}/r_0}$ to $\sqrt{2GM_{\text{BH}}/r_0}$. This interval was established based on the universal expression for the tangential velocity v_{tan} of any point on the orbit. If the magnitude of the initial tangential velocity vector is smaller than this factor, the motion will be elliptic, if it is larger, the motion will be hyperbolic, and if it is precisely this value, a parabolic orbit will be delineated. In consequence, by considering that the magnitude of its v_{x0} and v_{y0} components range from 0 km s^{-1} to the value given by this factor, all types of orbits are included. Thus, the initial conditions are just a point in the parameter space of any type of orbits of arbitrary eccentricity, size and orientation.

The final step in the modeling consists of an iterative fitting of orbits to the observed spatial points (x_{RL}, y_{RL}) in the ridge-line of the intensity map (Figure 3.2) and the projected velocities (v_z) . We evaluate the goodness of fit by means of an hybrid reduced χ^2 obtained by averaging the reduced χ^2 of each fitted parameter (x_{RL}, y_{RL}, v_z) . We weighted the χ^2 calculation by the square of the uncertainties – 1/4 of the spatial resolution for the x and y location, and for v_z the errors calculated during the extraction of the line properties as discussed in Section 3.3.2.1. If the model is a good approximation to the data, $\chi^2 \sim 1$. However, the hybrid nature of our χ^2 and the somewhat large uncertainties in the velocity values, could influence the scaling of the reduced χ^2 making its exact value unimportant. In this case, the best-fit will correspond to the orbit presenting the minimum χ^2 .

The first attempts to model the kinematics showed that a single Keplerian orbit cannot reproduce the totality of v_z vectors of the observed velocity field. Therefore, we decided to investigate two types of sets of initial conditions as suggested by the observed blue-shifted and red-shifted kinematical components: one for the northern region with $x_0 = 0 \pm 5 \text{ pc}$, $y_0 = 25 \pm 5 \text{ pc}$ and $v_{z0} = -25 \pm 10 \text{ km s}^{-1}$; and one for the southern part with $x_0 = -10 \pm 5 \text{ pc}$, $y_0 = -25 \pm 5 \text{ pc}$ and $v_{z0} = 30 \pm 10 \text{ km s}^{-1}$. The initial spatial coordinates (x_0, y_0) of the two sets were selected based on the morphology and kinematics. First, any good fit to the data should follow the ridge-line. Therefore it is reasonable to have the north and south starting points located on it. Particularly for the northern region, the initial coordinates correspond to the peak of H_2 emission in Figure 3.2. Furthermore, they are located in regions where the velocity uncertainties are low. This is once more particularly important for the northern region where the blue-shifted velocities associated morphologically with the northern tongue are well recognizable. Finally, a visual inspection of the velocity field suggests that the motions closer to the nucleus are probably perturbed by other physical processes and could possibly mislead the modeling.

Approximately 5×10^4 Keplerian orbits of arbitrary eccentricity, size and orien-

tation were modeled for each region and compared to the observations to determine a best fit. The orbits providing the best approximations to the data at these scales can be further compared with the large scale intensity map shown in Figure 3.1 in order to study the connection between the gas in the central arcsecond and the circumnuclear environment. Particularly, we will be able to test the hypothesis of gas streaming from the circumnuclear ring along the linear structure. This hypothesis could motivate a different approach for the determination of the initial conditions (x_0, y_0, v_{z0}) . The implicit assumption here is that the gas observed in the central arcsecond (basically the southern and northern tongue) originates from the ring and thus the initial conditions are determined by the crossing points of the linear structure with the ring. However, we decided not to follow this approach because the crossing points of the linear structure with the ring are not clearly determined, especially for the southeastern region where several filaments and knots of gas are connecting the ring to the linear structure (Figure 3.1). In addition, the complex velocity field at these scales contains several kinematical components (Müller Sánchez et al. 2008b). This complicates greatly the determination of the initial v_z vectors. Therefore, the approach based on the two sets of initial conditions mentioned in the last paragraph provides a reasonable more general methodology, which could not only test the hypothesis of gas streaming from the ring along the linear structure, but also determine the exact crossing points of the linear structure with the ring.

3.3.2.3 Gas is on highly elliptical/parabolic orbits

Based on the reduced χ^2 goodness of fit analysis described in Section 3.3.2.2, we found for the northern and southern regions that among the complete set of tested orbits, only highly elliptical/parabolic orbits provide good approximations to the datapoints (x_{RL}, y_{RL}, v_z) . These orbits are contained in planes that are rotated through an axis coinciding with the x -axis (PA of the rotation axis is 90°) and have inclinations between $30 - 60^\circ$. These results confirm the presence of gas streamers in the nucleus of NGC1068. The initial conditions and other parameters of three representative orbits of the southern region are shown in Table 3.1. The same information for three orbits of the northern region is presented in Table 3.2. The trajectories of the six orbits in the projected plane of the galaxy are shown in Figure 3.7 plotted over the intensity map. As can be seen in the upper panel of this Figure, the southern orbits are spatially associated with the southern tongue, and thus they are identified in Table 3.1 as orbits/streamers ST1, ST2 and ST3. The northern orbits are clearly associated with the northern tongue (down panel of Figure 3.7), and therefore they are designated as orbits/streamers NT1, NT2 and NT3.

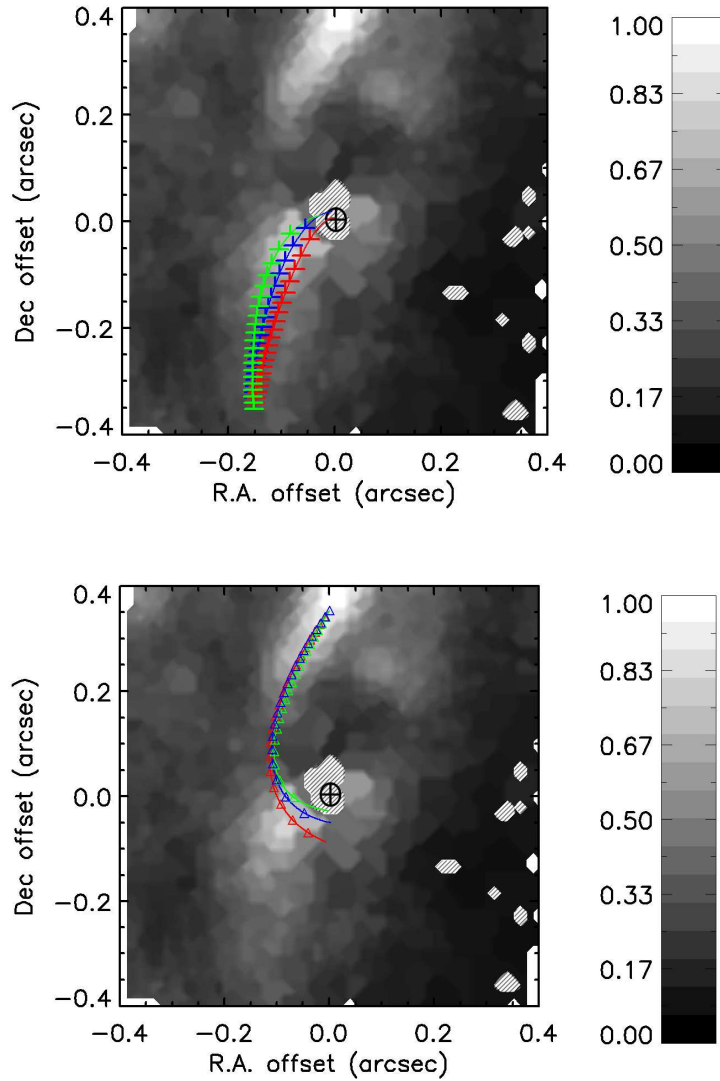


Figure 3.7: *Up:* Trajectories of orbits ST1 (red curve), ST2 (blue curve) and ST3 (green curve) plotted over the intensity map in black-white colour scale. *Down:* Trajectories of orbits NT1 (red curve), NT2 (blue curve) and NT3 (green curve) plotted over the intensity map in black-white colour scale. The peak of the non-stellar continuum is represented by a crossed circle in both panels. The bins where the line properties could not be extracted were masked out and correspond to the diagonal patterned regions in both images.

Orbit	i^a	PA ^a	x_0^b	y_0^b	z_0^b	v_{x0}^c	v_{y0}^c	v_{z0}^c	x_p^d	y_p^d	z_p^d	x_a^e	y_a^e	z_a^e	t^f	χ^2
ST1	30	90	-11	-25	-14	6	35	20	0.1	0.42	0.24	-25	-121	-70	0.9	0.87
ST2	45	90	-11	-25	-25	-1	25	25	-0.01	1.24	1.24	5	-70	-70	1	0.18
ST3	60	90	-11	-25	-42	-1	17	30	-0.3	1.07	1.85	28	-98	-169	1.1	0.71

^a Inclination and position angles are given in ($^\circ$)

^b Initial spatial coordinates in (pc)

^c Initial velocity vectors in (km s^{-1})

^d Spatial coordinates of the pericenter in (pc)

^e Spatial coordinates of the apocenter in (pc)

^f Infalling time scale in (Myr). This is defined as the time a gas cloud takes to travel from the initial coordinates to the pericenter

Table 3.1: Orbital parameters of the southern gas streamers.

Orbit	i^a	PA ^a	x_0^b	y_0^b	z_0^b	v_{x0}^c	v_{y0}^c	v_{z0}^c	x_p^d	y_p^d	z_p^d	x_a^e	y_a^e	z_a^e	t^f	χ^2
NT1	30	90	0.0	25	14	-25	-35	-20	-5	-3.7	-2.1	82	61	35	1.3	1.1
NT2	45	90	0.0	25	25	-18	-25	-25	-2.9	-2.9	-2.9	56	54	54	1.3	0.51
NT3	60	90	0.0	25	42	-12	-20	-35	-2.4	-1.8	-3	-	-	-	1.1	2

^a Inclination and position angles are given in ($^\circ$)

^b Initial spatial coordinates in (pc)

^c Initial velocity vectors in (km s^{-1})

^d Spatial coordinates of the pericenter in (pc)

^e Spatial coordinates of the apocenter in (pc)

^f Infalling time scale in (Myr). This is defined as the time a gas cloud takes to travel from the initial coordinates to the pericenter

Table 3.2: Orbital parameters of the northern gas streamers.

The v_z components of the six orbits are presented in Figure 3.8. For comparison, velocity curves of the data were extracted along the trajectories of the streamers. As these velocity curves are all similar, only the ones corresponding to orbits ST2 and NT2 are plotted in the upper and lower panels of Figure 3.8 respectively. As can be seen in the two panels of this Figure, there is good agreement between the models and the data within the error bars. The velocity of the gas that is now lying in front of the nucleus corresponds to that of the southern streamer. This is demonstrated in both panels of Figure 3.8 and in the upper panel of Figure 3.6 which shows the trajectories of orbits ST2 and NT2 plotted over the velocity map. It can be seen in this Figure that the southern red-shifted component is connected to the nuclear kinematic component along the streamer trajectory. For the northern region, the projected velocities of the models fit well the data until $r \sim 0.17''$. Within this radius the velocities of the streamer are not recognizable as they are being hidden by the nuclear redshifted kinematical component formed basically by the southern streamer and motions resulting from cloud-cloud collisions at few parsecs from the nucleus.

We evaluate the goodness of fit to the ridge-line and the projected velocities by means of the reduced χ^2 analysis discussed in Section 3.3.2.2. The results are shown in Tables 3.1 and 3.2. During the fitting process, it became clear that the somewhat large uncertainties in the velocity values influence the calculation of the reduced χ^2 . In consequence, the best-fit corresponds to the orbits presenting the minimum χ^2 . This was found for orbits ST2 and NT2 for the southern and northern regions, respectively. The conclusion arising from the orbital fits is that in the central arcsecond of NGC1068 there exist gas streamers flowing inwards/outwards along the southern and northern tongues in a plane which is rotated around an axis with a PA= 90° and has an inclination of 45° .

3.3.2.4 Streamers flow inwards in the plane of the galaxy

The orientation of the planes of the orbits discussed in Section 3.3.2.3 is so that the top half is on the far side and the bottom half towards us. However, the same fits to (x_{RL}, y_{RL}, v_z) are obtained for orbits located in planes that have the opposite orientation to the one presented in Tables 3.1 and 3.2 (negative inclinations). In other words, based only on the kinematic modeling, there are two sets of orbits that we cannot distinguish: those in which the gas is heading towards the nucleus, i.e. the gas is streaming inwards (positive inclinations), and those in which the gas is flowing away from it, i.e. the gas is streaming outwards (negative inclinations). Luckily, our data combined with previous observations provide enough evidence to break this degeneracy.

As demonstrated by several authors, the NE radio jet falls on the near side and its SW counterpart on the far side of the galaxy disk (e.g. Gallimore et al. 1996). The NE jet exhibits a bending point in its way out of the galactic plane caused by a shock interaction between the jet and a dense molecular cloud (Gallimore et al. 1996;

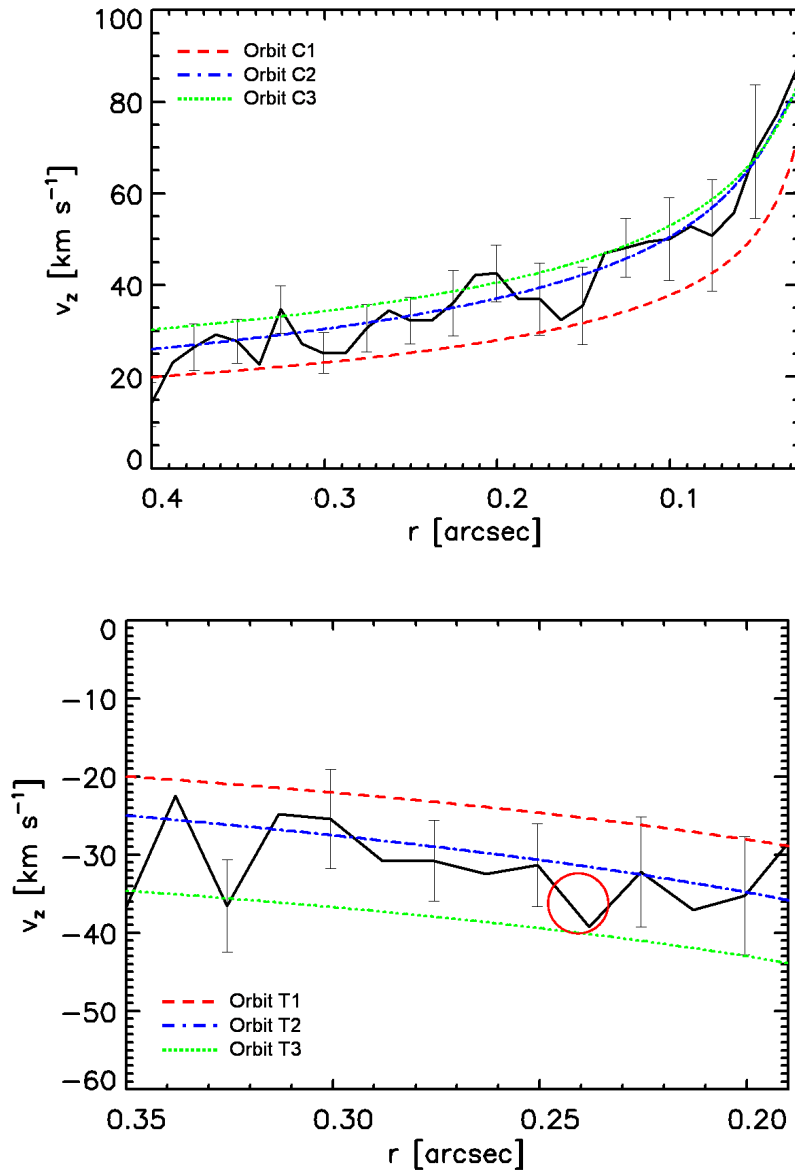


Figure 3.8: Line-of-sight velocities (v_z) of the streamers. The upper panel shows orbits ST1 (red dashed line), ST2 (blue dashed-dotted line), and ST3 (green dotted line). The lower panel shows orbits NT1 (red dashed line), NT2 (blue dashed-dotted line) and NT3 (green dotted line). In the upper panel, the black solid line corresponds to the velocity curve extracted from the data along the trajectory of orbit ST2 starting at $r = 0.4''$ until $r = 0.015''$ (1 pc). In the lower panel, the black solid line corresponds to the velocity curve extracted from the data along the trajectory of orbit NT2 starting at $r = 0.35''$ until $r = 0.2''$ (14 pc). The jet/cloud interaction in the north takes place at $r \sim 0.25''$, and is indicated by a red circle in the lower panel.

Tecza et al. 2001; Cecil et al. 2002; Poncelet et al. 2007). The direct evidence for the molecular cloud obstructing the way of the jet in our SINFONI data (Figure 3.5) indicates that the orientation of the plane containing the cloud must be compatible with that of the galaxy plane, i.e. the top half is on the far side and the bottom half towards us. In consequence, the gas transport is towards the nucleus, i.e. the gas is streaming inwards.

We can compare this scenario with previous observations of this galaxy. According to the “NGC1068 Ringberg standards” (Bland-Hawthorn et al. 1997), the galaxy disk has an inclination of $i = 40 \pm 3^\circ$ and a kinematic major axis close to 90° . A similar configuration was found from the kinematics of the stars observed at $r = 3''$ (~ 200 pc) with SINFONI (Davies et al. 2007; Müller Sánchez et al. 2008b). These authors found that a rotating disk model with a PA= $84 \pm 4^\circ$ and $i = 45 \pm 4^\circ$ reproduces the stellar kinematics well. At scales down to $r = 0.5''$, the stellar velocity field is compatible with the same kinematic major axis but the inclination is not well constrained. This situation is similar with what we have found for the gas, although our modeling favours an inclination of 45° .

The orientation is consistent with the strong evidence across the electromagnetic spectrum that the NE radio jet, ionization cones and the extended x-ray emission fall on the near side, and the SW counterparts of all these fall on the far side, and therefore hidden by the galaxy disk (Bland-Hawthorn et al. 1997). At last, the plane orientation of our model is also consistent with the recent H₂ observations of Galliano & Alloin (2002) who reproduced the observed changes in the line profiles across the 200 pc central region by a two-component kinematical model consisting of a rotating molecular disk inclined 65° with this orientation plus an outflow.

Thus, the resulting physical model consists of gas streamers located in the plane of the galaxy, and falling inwards from either side of the nucleus. The streamer in all cases approaches the centre (pericenters of a few pc), but as far as we can tell with the present spatial resolution, it does not actually reach the point source (see Tables 3.1 and 3.2). However, cloud-cloud collisions at few parsecs from the nucleus may provide a mechanism through which orbiting gas can lose angular momentum and remain in the inner region, falling eventually to the centre. Additionally, it can be seen in the lower panel of Figure 3.6, that the streamers constitute a σ -dip in the whole field and thus are cold, indicating that the gravity dominating the overall flow velocity is stronger than the internal dispersion. The tidal stretching of the material during infall produces the streamers now observed as a linear structure. These motions are strong evidence that we are seeing, on scales down to a few parsec, how gas is being driven toward the AGN in NGC1068, and hence how the AGN is being fuelled.

3.3.3 Mass of the infalling molecular material

We now discuss the molecular gas masses of the southern and northern tongues. The lack of robust direct probes of the gas mass complicates the analysis. To mitigate the

uncertainties, we have used several independent methods.

Our first estimate is based on the dynamical mass obtained by Davies et al. (2007) from the stellar kinematics in the central arcsecond of the galaxy. A dynamical mass of $M_{dyn} = 1.3 \times 10^8 M_{\odot}$ within $r = 0.5''$ (35 pc) is given by these authors. Assuming a conservative 10% gas fraction (Hicks et al. 2008) and that most of the gas mass within this radius is distributed in equal amounts inside the southern and northern tongues (see Figure 3.2), each of these components would have then a mass of $\sim 6 \times 10^6 M_{\odot}$. This value can be considered as a lower limit due to the small adopted gas fraction, which probably is higher in the nuclear regions of Seyfert 2 galaxies (Hicks et al. 2008).

On the other hand, assuming that the gas particles in each of the two tongues had initially a spheroidal geometry, we can estimate a dynamical mass directly from the dispersion velocity from the relation $M_{dyn} = 5\sigma^2 r/G$ (Bender et al. 1992). Considering a spheroid with radius $R = 0.1''$ (7 pc) based on the approximate FWHM of the southern tongue, and $\sigma = 70 \pm 15 \text{ km s}^{-1}$ as measured from the dispersion map along the trajectories of the streamers (Figure 3.6), we find a mass of $6.5 \pm 0.1 \times 10^7 M_{\odot}$ for each concentration of molecular gas. The obtained value represents an upper limit on the gas mass since this calculation implicitly assumes that the gas is gravitational bound and this may not be the case.

A third independent method to estimate the mass of the molecular gas in the region is from the H_2 1–0S(1) luminosity and an appropriate conversion factor between this quantity and M_{gas} . Müller Sánchez et al. (2006) found from large aperture ($3''$ or more) measurements of actively star-forming galaxies (including NGC1068) a ratio of $L_{1-0S(1)}/M_{\text{gas}} = 2.5 \times 10^{-4} L_{\odot}/M_{\odot}$. Although this ratio was obtained for conditions which are probably not met in the nuclear region of the galaxy and depends on fraction of gas on cloud surfaces that can be heated, we apply it simply because there is evidence for vigorous star formation close to the AGN (Thatte et al. 1997; Davies et al. 2007; Müller Sánchez et al. 2008b) and it can help us to make at least an approximate estimate of the total molecular gas mass. From the total H_2 1–0S(1) luminosity of the northern and the southern tongue we estimate the total gas mass of each component to be $6 \times 10^7 M_{\odot}$ and $4 \times 10^7 M_{\odot}$ respectively. The uncertainties in this approach correspond to the uncertainties in the conversion factor which has a 1σ statistical uncertainty from the 17 galaxies in their sample of a factor of 2. However, this factor has additionally a systematic uncertainty inherent to the probable overestimated gas masses of the galaxies in the table from Müller Sánchez et al. (2006) obtained using a standard CO– H_2 conversion factor (overestimation of factors 2–5). This would lead to masses for the northern and the southern tongue as little as $6 \times 10^6 M_{\odot}$ and $4 \times 10^6 M_{\odot}$ respectively. A similar conversion factor between cold and warm gas mass is proposed by Dale et al. (2005) for NGC1068 $M_{\text{H}_2}^{\text{warm}}/M_{\text{H}_2}^{\text{cold}} = 1 \times 10^{-6}$. After converting the H_2 1–0S(1) luminosities to warm gas masses (Dale et al. 2005), we obtain total gas masses which are very consistent to the values calculated by means of the ratio $L_{1-0S(1)}/M_{\text{gas}}$.

The X-ray irradiation of molecular clouds by the central X-ray source in NGC1068 has been discussed by Maloney et al. 1997 and Matt et al. 1997, see also Neufeld et al. 1994. Maloney et al. found that an attenuating column density of 10^{22} cm^{-2} between the central engine and the H_2 emitting molecular clouds in the central $r \sim 100 \text{ pc}$ accounts for the observed H_2 intensity. As the gas density is a function of radius, with higher densities the further in, it is probable that the column density is increased at our scales. Matt et al. (1997) have shown that the opaque material which obscures our direct view to the central engine of NGC1068 is Compton thick with an attenuating column density of at least $n_H = 10^{24} \text{ cm}^{-2}$. However, this does not imply that the H_2 clouds have precisely, or even approximately, this value. By assuming this and 10^{23} cm^{-2} as the upper and lower limits of the averaged column density in the central $r = 0.4''$, we find that the southern/northern tongue has a gas mass ranging from 2×10^6 to $2 \times 10^7 M_\odot$.

Our last method for determining the gas masses is based on the dust emissivity at mid-IR wavelengths. Recent mid-IR observations from Tomono et al. (2006) inferred a value of $4.6 \times 10^5 M_\odot$ for the dust mass in the northern tongue. As the total gas mass is expected to be ~ 100 times greater than the dust mass (Contini & Contini 2003; Draine 2003), a value of a $4.6 \times 10^7 M_\odot$ can be inferred for the gas mass in this component. Assuming once more that the two gas concentrations have basically the same mass, the southern tongue will have also a gas mass of $\sim 4.6 \times 10^7 M_\odot$.

We can compare the values derived from the five different methods with previous estimates of the gas mass in the nuclear region of NGC1068. From millimeter/sub-millimeter interferometry, Tacconi et al. (1994) estimated the total mass contained within $1''$ of the nucleus as $\sim 1.6 \times 10^8 M_\odot$. More recent interferometric observations of the $^{12}\text{CO}(1-0)$ and $^{12}\text{CO}(2-1)$ emission by Schinnerer et al. (2000) give a molecular mass of $\sim 5 \times 10^7 M_\odot$ contained in the central 100 pc of the galaxy. In addition, radiative transfer theoretical models from Schartmann et al. (2005) predict a dust mass of $8 \times 10^4 M_\odot$ in the central 70 pc, which converted to gas mass results in a value of $8 \times 10^6 M_\odot$.

All estimates are plausibly consistent with each other and with previous approximations suggesting that each molecular gas concentration (the southern or the northern tongue) has a mass within the range $6 \times 10^6 - 6 \times 10^7 M_\odot$ with a logarithmic mean of $2 \times 10^7 M_\odot$ and a statistical uncertainty of a factor of 3. We will adopt this value for the mass of each component. This is consistent with a 25% gas fraction of the dynamical mass in the central arcsecond of the galaxy (Tacconi et al. 1994; Thatte et al. 1997; Schinnerer et al. 2000; Davies et al. 2007; Müller Sánchez et al. 2008b). Furthermore, it is consistent with the molecular mass estimated from $^{12}\text{CO}(2-1)$ emission (Schinnerer et al. 2000) on slightly larger scales and an averaged column density in the central $\pm 0.4''$ of 10^{24} cm^{-2} .

3.3.4 Mass accretion rate

The morphology and kinematics of the gas are strong evidence that we are witnessing, on scales of a few parsecs, how gas is being driven toward the AGN in NGC1068, and hence how the nucleus is being fuelled.

The mass accretion rate down to a few parsecs from the AGN can be estimated assuming that material falls into the nucleus through the linear structure. The infalling time scale, defined as the time a gas cloud takes to travel from the initial position to the pericenter, is obtained directly from the modeling and has a value of 1.3 Myr for the northern streamer (see Table 3.2). This factor and the total gas mass yield a mass accretion rate at these scales of $\sim 15 M_{\odot} \text{ yr}^{-1}$ with a 1σ uncertainty of a factor of 3. This value is an upper limit since not all the gas flowing towards the nucleus will actually stay there. A similar value is found for the southern streamer assuming that its mass corresponds to the mass that currently is located in front of the nucleus. From millimeter interferometry, Tacconi et al. (1994) estimated this influx to be a few $M_{\odot} \text{ yr}^{-1}$ from the total mass contained within $1''$ of the nucleus ($\sim 1.6 \times 10^8 M_{\odot}$) and radial velocities ($\sim 50 \text{ km s}^{-1}$), which is of the same order as our data.

We can compare this inflow rate on scales of $\sim 10 \text{ pc}$ to that onto the black hole itself. The mass accretion rate at scales down to one Schwarzschild radius R_S can be estimated from the mass-to-luminosity conversion efficiency of a black hole $L = \eta c^2 dM/dt$, where η is the accretion efficiency with typical values $0.1 - 0.3$ (Eardley & Press 1975) and L is the bolometric luminosity of the AGN, which for NGC1068 is $\sim 8 \times 10^{44} \text{ ergs s}^{-1}$ (Telesco & Harper 1980). This yields a mass accretion rate of $0.03 - 0.09 M_{\odot} \text{ yr}^{-1}$, indicating that the dM/dt is reduced ≈ 1000 times from $r = 1 \text{ pc}$ to a few R_S . An analogous situation is observed at our own Galactic Center, for which mass accretion rates of $10^{-3...-4} M_{\odot} \text{ yr}^{-1}$ at $r = 1 \text{ pc}$ are observed (Genzel & Townes 1987), and $dM/dt \sim 10^{-7...-8} M_{\odot} \text{ yr}^{-1}$ at a few R_S from the point source SgrA* are estimated for a bolometric luminosity of the point source of a few $10^{38} \text{ ergs s}^{-1}$ (Ozernoy & Genzel 1996; Marrone et al. 2007). The apparent dM/dt is a strong function of radius, with much reduced dM/dt closer to the nucleus. Qualitatively this is a natural consequence of inefficient angular momentum transport. While this may be a coincidence, we speculate that the gas accretion mechanisms are similar for active and non-active supermassive black holes. Recent simulations of accretion of stellar winds on to Sgr A* (Cuadra et al. 2006) and supermassive black holes in Seyfert nuclei (Schartmann 2007), reveal that the cold gas streamed down to scales approximately ten times smaller and settled into a very turbulent disk. This suggests that indeed the processes both, helping and hindering gas inflow, are the same for Seyfert galaxies and the Galactic Center.

3.3.5 Obscuration by inflowing gas

We now discuss the implications of the presence of molecular gas in front of the nucleus to the obscuration of the AGN in NGC1068. First, we calculate the gas

mass surface density Σ of the southern tongue assuming once again a cloud radius of $R = 0.1''$. For a gas mass of $2 \times 10^7 M_{\odot}$ we obtain $\Sigma = 12 \times 10^4 M_{\odot} \text{ pc}^{-2}$, yielding a column density of $n_H = 8 \times 10^{24} \text{ cm}^{-2}$, which is comparable with the values predicted for highly absorbed objects ($n_H \geq 10^{24} \text{ cm}^{-2}$) and specifically for Compton thick sources such as NGC1068 (Bassani et al. 1999; Matt et al. 1997) and the column densities of clumpy torus models (Nenkova et al. 2002). This high column density suggests that the nuclear structure is optically thick in the near-IR and hence this gas concentration can be associated with the obscuring material that is hiding the broad line region. In addition, as this value represents an average on scales of $\sim 0.2''$, the true column density of individual smaller clouds must be larger. The fact that a considerably amount of the $2 \mu\text{m}$ and $10 \mu\text{m}$ emission from the innermost region ($\sim 1 - 2 \text{ pc}$) and the maser disk radiation is not obscured despite the presence of large gas column densities, implies that the structure must be a clumpy medium. Line-of-sight attenuation of all these in this case would be a mere consequence of one or more intervening molecular clouds.

Our observations therefore suggest that the southern tongue can be associated with the obscuring material that is hiding the nucleus but not in the classical picture of a rotating torus. This scenario is mainly ruled out by the kinematics which do not show any type of rotation near the AGN. However, there are several pieces of evidence that support this association. First, the size scale of the nuclear gas is remarkably similar to those of recent mid-IR observations (Bock et al. 2000; Tomono et al. 2001; Galliano et al. 2005; Tomono et al. 2006; Poncelet et al. 2007) and those of static torus models, in particular the latest clumpy model of Hönig et al. (2006), for which a size of $15 \times 7 \text{ pc}$ (diameter) is predicted for the H_2 distribution in this galaxy (Hönig personal communication). There is also a similarity between the PA of the major axis of the core $\sim 120^\circ$, which is consistent with that of the line of maser spots (Greenhill et al. 1996) and the 300K dust emission (Jaffe et al. 2007). Furthermore, the estimated gas mass and column density fully agree with previous observations and torus models (see Section 3.3.3). Hence we interpret this nuclear concentration of gas as a set of infalling clouds, that form the optically thick outerpart of an amorphous clumpy molecular/dusty structure. This large scale structure that we have observed will most probably enclose smaller clouds, qualitatively similar to a nested clouds scenario in which a distinct rotating molecular/dusty torus may or may not be present. In any case, based on the morphology and kinematics of the gas, we can state that if there is a rotating torus in NGC1068, its outer radius R_{out} must be smaller than 7 pc and it is encircled by this amorphous molecular/dust obscuration.

3.3.6 Connection of the streamers with the circumnuclear environment

The remaining subject to investigate is the origin of the infalling material. A detailed study of the physical conditions of the NLR and the molecular gas at larger scales is

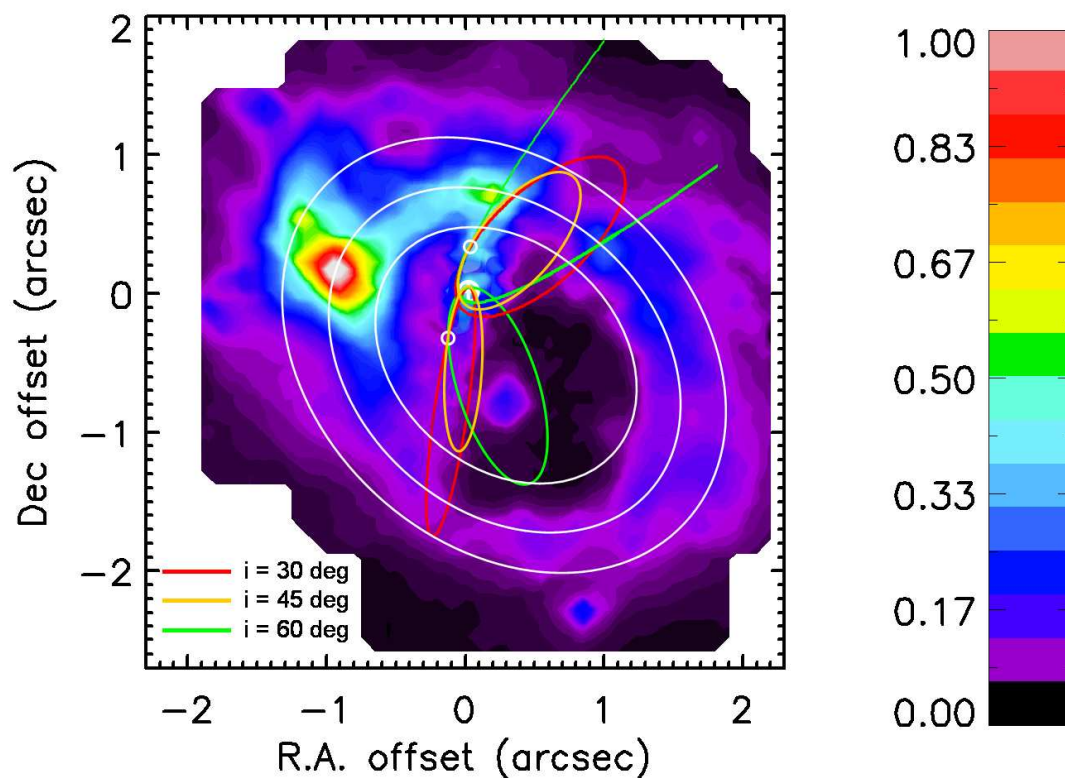


Figure 3.9: Complete trajectories of the six orbits described in Tables 3.1 and 3.2 plotted over the large scale H_2 intensity map. Orbits with 30° inclination (ST1 and NT1) are represented by red curves. Orbits with 45° inclination (ST2 and NT2) are shown in orange. Orbits with 60° inclination (ST3 and NT3) are represented by green curves. The location of the AGN as indicated by the peak of the non-stellar continuum is represented by a white crossed circle. The initial spatial coordinates (x_0 and y_0) of the orbits are indicated by small white circles. The white inner and outer concentric ellipses delineate the thickness of the molecular ring. The central white ellipse is only plotted for reference.

crucial for the understanding of this phenomenon. We postpone our analysis of these and other features in the central $3'' \times 3''$ of NGC1068 to a subsequent publication (Müller Sánchez et al. 2008b). Here, we provide a few remarks on the possible connection of the streamers with the circumnuclear environment.

In the central arcsecond, the orbital fit shows that highly elliptical/parabolic orbits in the plane of the galaxy reproduce the ridge and velocities of the gas quite well. A visual inspection of Figure 3.1 shows that apparently the central two streamers are part of a linear structure connecting the NNE and SSW to the circumnuclear ring. We can test this hypothesis by comparing the complete trajectories of the orbits with the larger scale H_2 emission map in Figure 3.1. A streamer is consistent with an origin in the ring if its apocenter lies inside the ring. If the apocenter of the orbit lies outside the ring, a ring origin of the streamer is uncertain. In order to have a reference of the width of the ring, we have superimposed on the intensity map several concentric thin rings of different sizes but having the same axis ratio and position angle as the observed ring in Fig. 3.1. Based on width of brightest H_2 emission around the ring, this overlay suggests that one can assign a characteristic thickness to the ring of $\sim 0.6''$ (~ 42 pc).

The results of this investigation for the six orbits described in Tables 3.1 and 3.2 are shown in Figure 3.9. In this Figure, we have plotted the complete trajectories of the orbits over the larger scale H_2 flux map presented in Figure 3.1. However, as the gas is streaming inwards, we observe only the part of each orbit which is transporting gas to the nucleus (the eastern part of each orbit). Based on the results from the χ^2 goodness of fit analysis, we considered primarily orbits with 45° inclination. As can be seen in Fig. 3.9, orbit NT2 follows the northern part of the linear structure until it apparently merges with the circumnuclear ring. The rest of the streamer's trajectory is fully contained in the ring implying that the streamer is consistent with an origin in the circumnuclear ring. In the southern region, orbit ST2 follows the nearly linear extension of the southern tongue until $r \sim 0.6''$. After this point, the linear structure is not distinguishable anymore from the several filaments and knots of gas which appear to be emanating from the ring. In this case, as the apocenter of the orbit is contained in the ring (note that the width of the ring can be slightly larger), streamer ST2 is also consistent with an origin in the circumnuclear ring.

The previous analysis has not only elucidated a plausible connection of the gas streamers with the circumnuclear environment, but also confirmed the results obtained from the χ^2 goodness of fit analysis. On one hand, the large scale study suggests that orbit ST3 is not a good fit to the data at these scales as most of its trajectory is actually observed in the empty cavity of the emission map where very little gas is detected. This and the fact that the origin of orbit NT3 is uncertain imply that the gas is with high probability not contained in orbits with inclination angles close to 60° . On the other hand, if one asserts that the gas originates in the ring, orbits with 30° inclination (ST1 and NT1) provide a moderate fit to the data at these scales. Notice that due to the uncertainty in the thickness of the ring, the origin of streamer

NT1 could be associated with the ring. In any case, if the streamers originate in the ring, the large scale study clearly favours orbits with inclination angles close to 45° , fully consistent with the results from previous χ^2 analysis (Section 3.3.2.3).

Whether the circumnuclear ring is contained in the plane of the galaxy as the streamers or in another configuration is presently uncertain. Assuming a ring origin for the streamers, and that the circumnuclear ring is contained in the plane of the galaxy as suggested by previous authors (Schinnerer et al. 2000; Galliano & Alloin 2002), then for material in the ring to approach the center, collisions must remove a significant fraction of the angular momentum. There is strong evidence that gas in the ring exhibits significant non-circular motions (Galliano & Alloin 2002; Davies et al. 2006; Müller Sánchez et al. 2008b). This could result in collisions that lead to loss of sufficient angular momentum. Such non-rotating clouds would likely collide with orbiting material in the ring at a stationary point in space, the gas torn off the ring would originate at this stationary point, and so should follow a time-independent path. The tidal stretching of the material during infall produces the streamers now observed as a linear structure.

However plausible this scenario may seem, it remains speculative at this point. A better understanding of the physical properties of the circumnuclear ring is required. Thus, as mentioned above, we postpone any interpretation of the ring to a subsequent paper (Müller Sánchez et al. 2008b).

3.4 Conclusions

We have presented in this paper high resolution SINFONI observations of the molecular gas in the nucleus of NGC1068. The distribution of the H_2 1–0S(1) emission at a resolution of $0.075''$ has been resolved. Two bright regions connected by a linear structure extending up to $0.7''$ north of the nucleus along a PA of $\sim -14^\circ$ are distinguished: one lying right in front of the nucleus (the southern tongue) and another one $0.35''$ north of the center (the northern tongue). The northern tongue correlates with the mid-IR emission and its tip coincides with a knot of radio continuum emission providing direct evidence of the shock interface between the jet and a molecular cloud that has caused the jet direction to change. The main results of our analysis on the kinematics of these components are summarized as follows:

- Dynamical modeling shows that material is streaming towards the nucleus. The infalling gas is contained on elliptical/parabolic orbits whose orientation is consistent with that of the plane of the galaxy. We interpret this as strong evidence of how gas, on scales of a few parsecs, is fueling the AGN.
- The gas transport is from ~ 70 pc to a few parsecs from the nucleus in the plane of the galaxy. The modeling reveals the existence of two streamers: a northern streamer associated with the northern tongue that passes very close

to the nucleus (pericenter of 5 pc), and a southern streamer which lies currently in front of the nucleus associated with the southern tongue, and has a pericenter of ~ 1 pc.

- The mass inflow rate dM/dt is $\sim 15 M_{\odot} \text{ yr}^{-1}$ from scales of 30 pc to a few pc. This is about 1000 times that from a few pc to a few times the Schwarzschild radius R_S . A similar change in the mass inflow rate with radius is observed in the Galactic Center. This may be a natural consequence of inefficient angular momentum transport.
- The geometry, kinematics and high column density of the nuclear concentration of molecular gas (the southern tongue) can be explained by a tidally disrupted streamer consisting of a set of infalling clouds that form the optically thick outerpart of an amorphous clumpy molecular/dusty structure.

Part II

Design of an interferometric integral-field spectrograph for the LBT

Chapter 4

Introduction to the design study SERPIL/LIINUS

The use of optical interferometry to make high resolution astronomical measurements was first suggested by Fizeau (1868). However, it was Albert Michelson who successfully measured the diameter of a star (α Ori) using interference fringes at the 100 inch telescope on Mt Wilson, California (Michelson & Pease 1921). Optical astronomy nowadays is confronted with the problem that current technology can not provide ever-increasing collecting area for telescopes. As a result, there has been significant interest and rapid growth in the field of optical interferometry in recent years, resulting in several state-of-the-art facilities, including Keck-I, VLTI, CHARA, PTI, and the Large Binocular Telescope (LBT).

The LBT is an innovative project which offers several interesting possibilities for interferometry. Currently two different beam combiners are being developed for this telescope: the LBTI (Large Binocular Telescope Interferometer - Hinz et al. 2003) performing nulling interferometry, and LINC-NIRVANA (the LBT INterferometric Camera, Near-IR / Visible Adaptive iNterferometer for Astronomy - Herbst et al. 2004), a Fizeau interferometric camera incorporating multiconjugate adaptive optics. As LBTI is a nulling interferometer, and LINC can be understood as a high resolution camera, a natural next step for exploiting the full configuration of the LBT would be the construction of an interferometric spectrograph. However, currently no high resolution spectroscopic capability is planned for the LBT.

This part of the thesis describes developments towards the design of an interferometric integral-field spectrometer for the LBT, baptized as the SERPIL/LIINUS project. While Chapter 4 describes the context, the scientific motivation and the characteristics of the SERPIL/LIINUS project, Chapter 5 explores the physical problem of coupling light from a double pupil into optical fibers, a vital issue to investigate for the design of a lenslet+fibers integral field unit for the LBT. The main physical principles of imaging interferometry and optical fibers are discussed in Section 5.2.

4.1 The Large Binocular telescope (LBT)

The Large Binocular Telescope (LBT - Hill & Salinari 2003), currently nearing completion on Mount Graham in Arizona at an altitude of about 3200 m, is a pioneering project being undertaken by European and US-American institutions. The structure of the telescope incorporates two 8.4-meter mirrors on a 14.4 meter center-to-center single common mount. Figure 4.1 shows the configuration of the Large Binocular Telescope. Having both mirrors on a single mount allows the LBT to operate basically in two modes: as two 8.4 meter telescopes with separate focal planes and instruments, and as an interferometer with light from the two mirrors combined coherently. This arrangement provides the equivalent collecting area of a 12 meter telescope, and when combined coherently, the equivalent angular resolution of a 28m telescope.

Essentially all current ground-based interferometers are of Michelson or pupil-plane configuration. In this type of instrument, the beam combiner superposes the two (or more) telescope pupils, and, by measuring the optical path difference in a small delay line, produces a modulated signal as the two paths pass back and forth through constructive (zero optical path difference) interference. The amount of fringe modulation, called the visibility, represents the amount of correlated flux with spatial frequency and orientation determined by the geometry of the observation – essentially one point in the spatial frequency spectrum of the object distribution. Note that LBTI, the Arizona nulling interferometer planned for the LBT is a special type of amplitude interferometer with a fixed, π phase shift between the pupils. Although widely implemented, visibility, or Michelson, interferometry suffers from a number of significant difficulties which limit its applicability for conventional astronomy. Perhaps the most severe of these is that pupil-plane interferometry does not directly produce images. Field of view (FoV) limitations are also severe for these interferometers. Depending on the type of observation, the FoV of ground-based pupil-plane interferometers ranges from a few tens of milli-arcseconds to approximately one arc-second.

A number of authors discuss Fizeau or image-plane interferometry in the context of the LBT (McCarthy et al. 2000; Herbst et al. 2000; Hege et al. 1995; Hill 1994). In a Fizeau interferometer, the wavefronts interfere in the focal plane, not in the pupil plane and therefore Fizeau interferometers are true imaging devices. Perhaps the simplest way to think of a Fizeau interferometer is as a very large telescope with diameter greater than or equal to the distance between the two end points in the component telescopes along the baseline direction, but with a mask corresponding to the configuration of single telescopes placed in the entrance pupil. The Fourier Transform of this pupil layout is the Point Spread Function (see Section 5.2). The Fizeau configuration overcomes the FoV restrictions of Michelson Interferometers. In fact, the field of view can be arcminutes in size, limited only by the ability of the adaptive optics (AO) system to deliver aberration-free wavefronts over large sky angles. Because they deliver true images, Fizeau interferometers do not suffer much

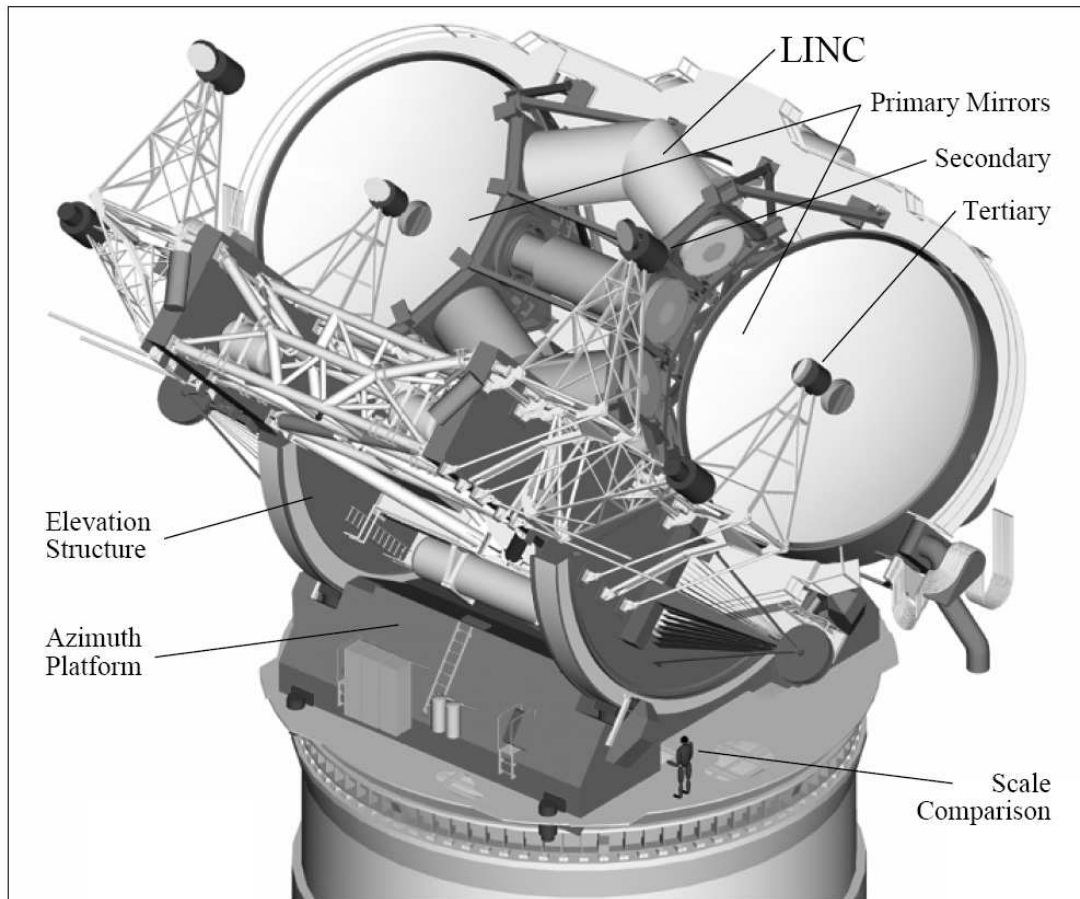


Figure 4.1: The Large Binocular Telescope (from Herbst et al. 2004). Note that the secondary mirror structures hold two sets of optics, the adaptive membrane secondaries and 45° mirrors for launching the laser guide stars. A person standing near the base gives the scale.

from ambiguities inherent in the interpretation of visibility measurements.

Fizeau interferometry provides high angular resolution over a wide field of view, but only if certain conditions are met. Fundamental among these is the requirement of geometrical similarity between the entrance and exit pupils of the optical system (this is the so-called “sine condition” or homothetic pupil constraint). The LBT has an enormous advantage over other telescope arrays in this regard: because the two mirrors share a common, steerable mount, the telescope always presents the same pupil configuration to the target. This drastically simplifies the task of maintaining constant pupil geometry. This translates directly to cost savings and increased sensitivity. For example, on the LBT, there will be only three warm mirrors before the radiation enters the beam combiner (the VLTI has more than ten).

The LBT supports a total of ten focal stations, including two prime, two “direct” Gregorian (below the primary mirrors) and a total of six “bent” Gregorian foci (on the central instrument platform). The two interferometric instruments, LBTI and LINC-NIRVANA, will occupy two pairs of these six, central, focal stations (Herbst et al. 2004).

4.2 The LBT Interferometric Camera (LINC/NIRVANA)

As part of their contribution to the Large Binocular Telescope project, the MPIA in Heidelberg and its collaborators have proposed to build the LINC-NIRVANA instrument, a near-infrared image-plane beam combiner with Multi-Conjugate Adaptive Optics (MCAO). It will combine the radiation from the two 8.4 m primary mirrors of the LBT in Fizeau mode. This configuration preserves phase information, and allows true imagery over a wide field of view. LINC-NIRVANA will deliver the sensitivity of a 12 m telescope and the spatial resolution of a 28 m telescope, over a field of view up to two arcminutes square. The main parameters of LINC-NIRVANA are shown in Table 4.2.

The instrument consists of three major components: an ambient temperature stiff mechanical bench with foreoptics, a cold cryostat with detector systems for science and fringe tracking, and an MCAO system consisting of two wavefront sensors (WFS) and two deformable mirrors (DM) per telescope. Herbst et al. (2004) describe the design and operating principles of LINC-NIRVANA in detail. Here a small description of the optical path based on Figure 4.2 will be provided. Light from the telescope tertiary mirrors comes to a focus inside the instrument enclosure. At this location, an annular mirror reflects the region of sky from 2 to 6 arcminutes in diameter into the Ground Layer Wavefront Sensors (GWS). These devices measure wavefront aberrations introduced by the lowest atmospheric layers, and send the corresponding correction signals to the adaptive secondary mirrors. The central 2' diameter field continues into the instrument and is redirected by two additional mirrors and a shared

Parameter	Value
Science wavelength range	0.9 – 2.4 μm
Science FoV	11 arcsec
Pixel scale	0.0057" /pixel
MCAO FoV	2'-6' annulus for GWS
FFTS FoV	2" with search area of 1' \times 1.5'
Science detector Pixel Size	2048 \times 2048
FFT detector Pixel Size	350 \times 350
RNO	< 5e ⁻
Strehl of optics	> 80%

Table 4.1: Important parameters of LINC/NIRVANA.

beam combiner mirror downward into the science channel cryostat. The first of these three mirrors is a Xinetics 349 actuator DM driven by signals from the Mid-High Layer Wavefront Sensor (MHWS). This WFS receives the visible light reflected from a dichroic mirror below the down-folding mirror and directly above the cryostat. The near-infrared radiation continues into the cryostat, where a relatively conventional reflective camera produces the science focus on a 2048 \times 2048 HAWAII-2 detector array. Just before the science sensor, an additional dichroic mirror separates some of the infrared radiation for fringe tracking. The differential atmospheric piston correction signal from the fringe tracker is applied to a piezo-electric linear stage, which drives the down-folding beam combination mirror back and forth, shortening one optical path while lengthening the other. Thus, there are three atmospheric correction loops: two for adaptive optics and one for differential piston.

Essentially LINC-NIRVANA is a general purpose instrument for the LBT. Key science programs being pursued by the LINC-NIRVANA team include pushing supernova cosmology studies to beyond redshift 3, following the evolution of complex structures in star-forming regions, and detecting Jupiter-mass planets around nearby stars.

4.3 Scientific Justification for an interferometric integral-field spectrograph at the LBT

Integral-field spectroscopy has demonstrated to be a very powerful observational technique in modern astronomy. An example of the great science that can be done using this technique is precisely shown in Part I of this thesis. By adding a high resolution integral-field spectroscopic capability to the LBT, we will be able not only to exploit efficiently the potential of the telescope, but also to bring several science programs to

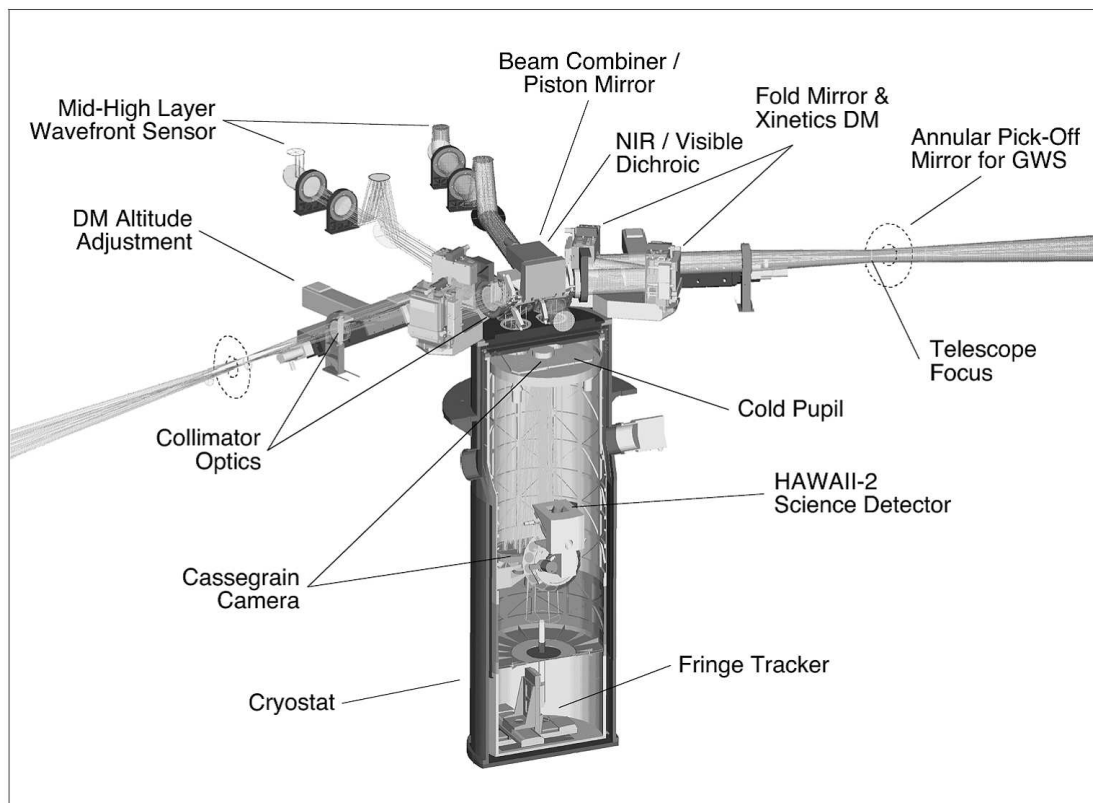


Figure 4.2: The LINC-NIRVANA optical path, including the Ground Layer Wavefront Sensors (GWS), ambient temperature collimator lenses, cold pupil stop, cryogenic camera, and Mid-High Layer Wavefront Sensors (MHWS).

the next level via interferometry - increased sensitivity, spatial and spectral resolution. One of the main motivations for such an instrument is to continue with the nearby AGN research program initiated with SINFONI and study at three times enhanced spatial resolution the distribution and kinematics of the stars and gas surrounding the AGN. In the following subsections, we summarize the most important science drivers of this instrument. We refer to it as SERPIL/LIINUS, the name adopted by the participants of the project (see Section 4.5).

4.3.1 Nearby Active Galactic Nuclei

The coexistence of an active galactic nucleus (AGN), presumably a black hole with an accretion disk, and a starburst region on scales of a few parsecs around the nucleus, is one of the key issues to investigate in the context of AGN. Increasing evidence that starbursts do occur in the vicinity of AGN (e.g. Davies et al. 2007), has revived the importance of disentangling how the gas is driven to the inner regions of AGN leading to star formation, and how AGN and star formation activity impact on each other. SERPIL/LIINUS will be ideally suited for studying the nuclear environments of active galaxies at near-infrared wavelengths (where extinction is a factor of 10 smaller than at optical wavelengths) and with adaptive optics assisted interferometric spatial resolution. At an angular resolution of ~ 16 mas in K -band, SERPIL/LIINUS will be able to resolve the central stellar cluster and the molecular torus on scales of one parsec at an object distance of 10 Mpc. Spectral synthesis models can then be used to infer the age and stellar mass function in individual star-forming regions. In addition, observations at this resolution will allow us to directly test the Unified Model of AGN by separating spatially and spectrally the narrow line clouds from the inner broad line clouds. Observing in K -band provides us with diagnostics e.g. for stellar content and dynamics (CO bandheads along $2.3 \mu\text{m}$), warm molecular gas (rotational-vibrational transitions of molecular hydrogen, e.g. H_2 1-0S(1) at $2.12 \mu\text{m}$), star formation rate (e.g. $\text{Br}\gamma$ emission at $2.17 \mu\text{m}$) and high excitation processes (coronal lines of [SiVI] at $1.96 \mu\text{m}$ or [CaVIII] at $2.32 \mu\text{m}$). Integral-field spectroscopy has already been used to characterize the stellar and gaseous components in the nucleus of several nearby AGN, providing very interesting results (Müller Sánchez et al. 2006; 2008b).

In addition, integral-field spectroscopy is extremely well suited for studying the inner dynamics in nearby AGN, and therefore for the determination of the nuclear mass, since it helps to avoid ambiguous interpretations from e.g. slit spectroscopy. The determination of black hole masses in AGN based on stellar dynamics is a crucial topic in modern astronomy, not only for the verification of the $M_{BH} - \sigma_*$ relation, but also to provide a comparison to reverberation masses which might then allow to constrain the size and geometry of the broad line region. The high spatial resolution and integral-field capability of SERPIL/LIINUS will provide an ideal combination to do this. Recently, by means of SINFONI at the VLT, Davies et al. (2006) have

Galaxy	RA J2000	Dec J2000	Type	Nuc	Dist Mpc	K mag
NGC1068	02:42:40.7	-00:00:48	SAb	Sy2	14.4	8
NGC2841	09:22:02.6	+50:58:35	SAb	L/Sy1	9.8	8.6
NGC3627	11:20:15.0	+12:59:30	SABb	Sy2	8.9	8.5
NGC4151	12:10:32.6	+39:24:21	SABab	Sy1.5	14	9.15
NGC4258	12:18:57.5	+47:18:14	SABbc	L/Sy1.9	6.95	9.74
NGC4579	12:37:43.6	+11:49:05	SABb	Sy2	20	8.6
NGC4594	12:39:59.4	-11:37:23	SAa	L/Sy2	13.7	8.52
NGC4725	12:50:26.6	+25:30:03	SABab	Sy2	17.1	9
NGC4826	12:56:43.7	+21:40:52	SAab	Sy2	5.6	8.34
NGC5033	13:13:27.5	+36:35:38	SAc	Sy2	13.3	9.1

Table 4.2: SERPIL/LIINUS AGN sample.

successfully derived the black hole mass in NGC3227 from stellar kinematics for the first time for a Seyfert 1 galaxy.

An initial nearby AGN sample is listed in Table 4.2. Source selection was driven by technical considerations, the primary criteria being:

1. the nucleus should be bright enough for fringe-tracking (K -band magnitude < 10 , LINC FDR),
2. the galaxy should be easily observable at LBT's latitude,
3. the galaxy should be close enough so that small nuclear structures can be resolved at the near-infrared diffraction limit of an equivalent 28-m telescope, and
4. the galaxies should be "well-known" so that complementary data can be found in the literature

4.3.2 Stellar content and supermassive black holes in nearby galaxies: the case of M31

Using the diffraction limited angular resolution of SERPIL/LIINUS, the spatially resolved near-IR properties of individual stars in the bulges of nearby galaxies can be investigated. Abundance studies can be carried out by analyzing stellar absorption lines blueward of the $2.3 \mu\text{m}$ CO bandheads, such as Mg, Si and Ca species, allowing the constraint of the formation history of galaxy bulges such as M31 or M32. There is now strong evidence for the presence of massive black holes in the nuclei of a number

of nearby galaxies. In these "normal" galaxies, the black hole is starving from the depletion of gas inflow. It seems now established that the Milky Way, NGC4258, and likely M31 each host a supermassive black hole (Bender et al. 2005). The mass of the black hole correlates with the bulge velocity dispersion, the so called $M_{\text{BH}} - \sigma_*$ relation (Ferrarese & Merrit 2000). SERPIL/LIINUS will help to test the $M_{\text{BH}} - \sigma_*$ relation in a variety of nearby galaxies. This requires sensitive spectroscopy of the stellar and gas kinematics at high spatial resolution to probe within the radius of influence of the central black hole. Radii of influence between 30 and 50 mas are expected, which can be probed by the interferometric diffraction limit of the LBT.

In addition, novel observation programs will become possible on M31 using SERPIL/LIINUS. The proper motions of the stars can be followed over several years, allowing for a direct measurement of the black hole mass, in much the same way as has been done for the center of our Galaxy. The far greater distance to M31 is compensated by the fact that the velocities in the disk around the supermassive black hole are much higher.

4.3.3 Galactic Center

The black hole in the center of the Milky Way is an ideal laboratory for studying supermassive black holes. Recent observations using SINFONI integral-field spectroscopy allowed the radial velocities of the stars near SgrA* to be measured and their 3-dimensional orbits to be determined (Eisenhauer et al. 2005). This provides the most accurate distance and mass estimate of the Galactic Center black hole.

Another interesting topic is the flare activity of SgrA*. Since these flares are weak and strongly blended with light from neighboring stars, the flare physics can only be disentangled using instruments offering spatial resolutions better than a few tens of milliarcseconds.

Imaging spectroscopy with SERPIL/LIINUS will allow the study of 3D-motions of the central stars at ~ 3 times better angular resolution compared to current 8–10 m telescopes, and probe the immediate vicinity of the central black hole at a distance of approximately 100 AU.

4.3.4 Extrasolar Planets

About 170 extrasolar planets have been detected so far, most of them indirectly, i.e. through periodic Doppler-shift of stellar absorption lines. However, these observations disclose hardly any detailed information about their atmosphere and formation. The angular resolution of present telescopes offers the opportunity to obtain direct observations of a limited number of extrasolar planets. The first direct detection of exoplanets was recently published (Deming & Seager 2005; Charbonneau 2005). Although photometrical measurements with high angular resolution are currently being carried out by masking out the star using diverse coronagraphic techniques, spec-

tral information is needed in order to study in detail the physical properties of the exoplanets. SERPIL/LIINUS will be the proper instrument for such observations, since it provides the necessary imaging and spectroscopic capabilities at an angular resolution of ~ 16 mas in K -band. This research programme with SERPIL/LIINUS at the LBT will be the precursor of a more exhaustive study of exoplanets with the next generation 30–100 m class telescopes.

4.4 Top level requirements

The following top-level requirements arise mainly from the science drivers discussed in Section 4.3 and the general LBT environment.

- Instrument type: near-IR integral field spectrometer in Fizeau interferometric imaging mode
- Field of view: $1'' \times 1''$ in interferometric mode
- Science wavelength range: $0.9 - 2.4\mu\text{m}$ with optimization to K -band
- Pixel resolution: better than Nyquist sampling (2-3 pixels per central fringe, $0.005''/\text{pix}$, maximum $0.01''/\text{pix}$ in K -band)
- Spectral resolution: $R > 3000$ for OH lines suppression
- Pixel size: $15 \mu\text{m}$
- Detector array: 4096×4096 pixels
- Throughput $> 25\%$

In addition, working at near-infrared wavelengths requires the spectrograph to be cooled down to about 77 K. However, depending on the instrument configuration (see Section 4.5.1), part of the instrument might work at ambient temperatures.

4.5 The SERPIL/LIINUS project

SERPIL/LIINUS is a design study for a high-resolution integral-field spectrometer performing Fizeau interferometry at near-infrared wavelengths. The goal of the project is to augment the scientific outcome of the LBT interferometric configuration with imaging spectroscopy.

The project was initiated at the Max-Planck-Institute for Extraterrestrial Physics (MPE) in Garching under the name of SERPIL (Spectrograph for Enhanced Resolution Performing Imaging interferometry on the LBT). A similar project LIINUS (LINC-NIRVANA Interferometric Imaging Near-infrared Upgrade Spectrograph) was

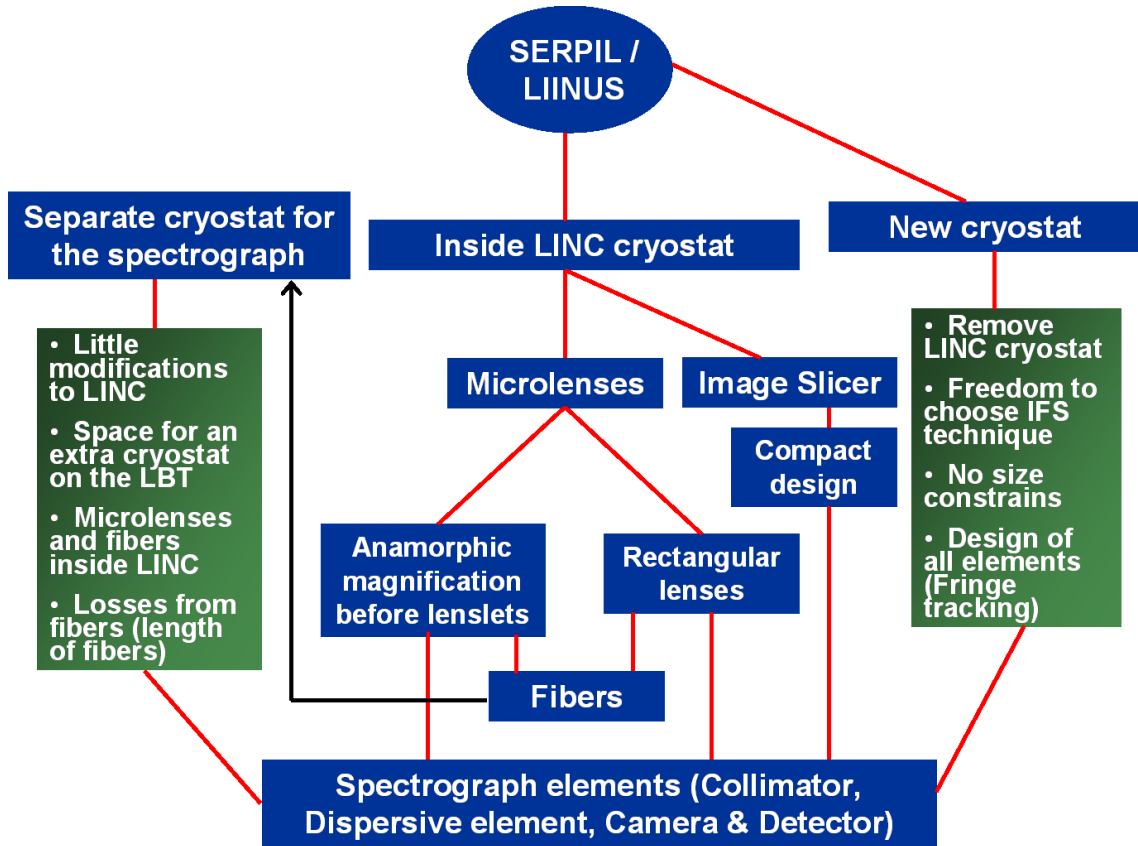


Figure 4.3: Technical solutions for SERPIL/LIINUS.

independently launched at the I. Physics Institute of the University of Cologne. The joint cooperation between both groups is reflected in the acronym SERPIL/LIINUS. The rest of this Section will be dedicated to introduce the main technical developments towards the final design of the instrument.

4.5.1 Technical options for SERPIL/LIINUS

As was mentioned in Section 1.3, the most critical part of every integral-field spectrograph is the IFU. For SERPIL/LIINUS, the three major types of IFUs are explored: microlenses, fiber bundles, and image slicers. The choice of the IFU will depend not only on the science drivers, but also on other physical and technical issues. The several possibilities are shown in Figure 4.3.

As can be seen in this Figure, LINC/NIRVANA plays a very important role in the SERPIL/LIINUS project. It turns out that the first decision to make is whether to build SERPIL/LIINUS within the LINC/NIRVANA hardware or in a separate cryostat. The main advantage of building the spectrograph inside LINC is the pos-

sibility of using existing subsystems to perform important and common tasks such as wavefront sensing and correction, and fringe & flexure tracking. However, strong size constraints are imposed, making the design of SERPIL/LIINUS very challenging. Indeed, a very compact design of the spectrograph (if any) is mandatory in order to fulfill the top level requirements (see Section 4.5.2). Furthermore, several modifications to the existing LINC design must be done to place the spectrograph in its cryostat. On the other hand, building a complete separate instrument would give us full freedom to choose the most appropriate IFU and other optical elements to better accomplish the scientific goals of the project. However, all the elements for common observing tasks mentioned above would have to be re-designed and constructed, resulting in higher costs and probably the requirement of more time for building the spectrograph. In addition, since LINC/NIRVANA and SERPIL/LIINUS would operate independently, each would need its own time for observations at the telescope, meaning that every time one goes on-line the other would need to be removed.

Luckily, there exists a third option which consists in placing only a focal plane unit inside LINC and transporting the light via optical fibers to a separate cryostat which contains the optical elements of a classical spectrograph. The focal plane unit consists of a lenslet+fibers IFU. This solution has several advantages over the others. Firstly, it alleviates the size constraints and therefore gives more flexibility to the project. In addition, few modifications to LINC need to be done, and SERPIL/LIINUS would still be able to benefit from the existing fringe tracking unit. However, there exist a physical and a technical problem in this approach: light coupling losses and the construction of the focal plane unit (coupling microlenses to thousands of fibers). Due to its importance, the physical problem of coupling light to optical fibers is the main topic of this part of the thesis and will be presented in Chapter 5. Regarding to the technical problem of building the complete unit, our baseline is the method described in Tecza et al. (1998). These authors achieved to position the fibers exactly centered on the optical axis of the microlenses by assembling a monolithic system consisting of flared fibers glued into the microlenses.

As can be seen in Figure 4.3, the lenslet+fibers approach will be only considered if the spectrograph is built in a separate cryostat. For the other two solutions (inside LINC or a completely new instrument) the main two IFUs considered are a microlens array unit and an image slicer.

Image slicer IFUs normally occupy a lot of space due to the long pseudo-slit formed (see Section 1.3). This solution for SERPIL/LIINUS would mean that the instrument could probably not be built inside the LINC cryostat, implying the construction of a separate cryostat for the whole instrument. A variation of this principle, the so-called “advanced image slicer”, could provide the necessary reduction in the size of the pseudo-slit to implement SERPIL/LIINUS inside LINC. On the other hand, the most compact IFUs are generally the lenslet units. For a spectrograph fully integrated to LINC, this solution is the baseline.

Based on all this, we have considered for further studies in the SERPIL/LIINUS

project the following two cases: the lenslet+fibers approach with an external spectrograph, and the whole integral-field spectrograph inside LINC approach based on a microlens array IFU. The advanced image slicer IFU could be an alternative for the second approach but it needs further investigations that have not been undertaken yet. We have not examined in detail the option of building a completely new instrument, because of the overload implied in the telescope operation for instrument changes.

4.5.2 Key components of SERPIL/LIINUS

The two design concepts (Section 4.5.1) of SERPIL/LIINUS have different potential show-stoppers: the physical problem of coupling light from a double pupil to optical fibers in the case of the lenslet+fibers approach, and the design of a very compact integral-field spectrograph for the “inside LINC spectrograph” approach. The issue of coupling light to optical fibers will be discussed in Chapter 5.

Regarding to the “inside LINC spectrograph” approach, our investigations suggest that there is space available for upgrades in the upper part of LINC (Gal et al. 2008). This space was initially considered as a cylinder of 30 cm diameter, and length of 70 cm. However, as the LINC/NIRVANA final design is not yet completed, the available size for the spectrograph is not yet a fixed parameter (see Section 5.4.2). In order to demonstrate that building a spectrograph inside this volume is feasible, a preliminary optical design employing a microlens array IFU was first developed and is discussed in the next Section.

4.5.2.1 Preliminary optical design using microlenses

In this Section, the key components of the integral-field spectrograph in the “inside LINC” approach are presented. They are part of a preliminary optical design using a rectangular microlens array which marginally fits the instrument inside LINC/NIRVANA (Gál et al. 2006). Notice that the optical elements in this design could be potentially used for the spectrograph in the lenslet+fibers approach.

The integral-field spectrograph will include three main units: pre-optics, IFU and spectrograph. The telescope field is first enlarged in order to match the microlens array dimensions, the microlenses then perform the field sampling and focus the incoming light on micropupils, and finally the micropupils are imaged and dispersed through a classical spectrograph with collimator, dispersing element and focusing optics (camera). For the design study, we assume that the dispersed micropupils will be focused onto a HAWAII-2 4096×4096 HgCdTe Detector Array with a pixel size of 15 μm (Hodapp et al. 2004). An all dioptric solution derived from the TIGER design (Bacon et al. 1995) has been selected (see Figure 4.4) because mirror solutions tend to result in larger instruments. The overall optics envelope is a cylinder of 16 cm diameter and 70 cm length. The advantage of this design is its small volume, but its performance depends on glass behavior at low temperature. As a reminder, the

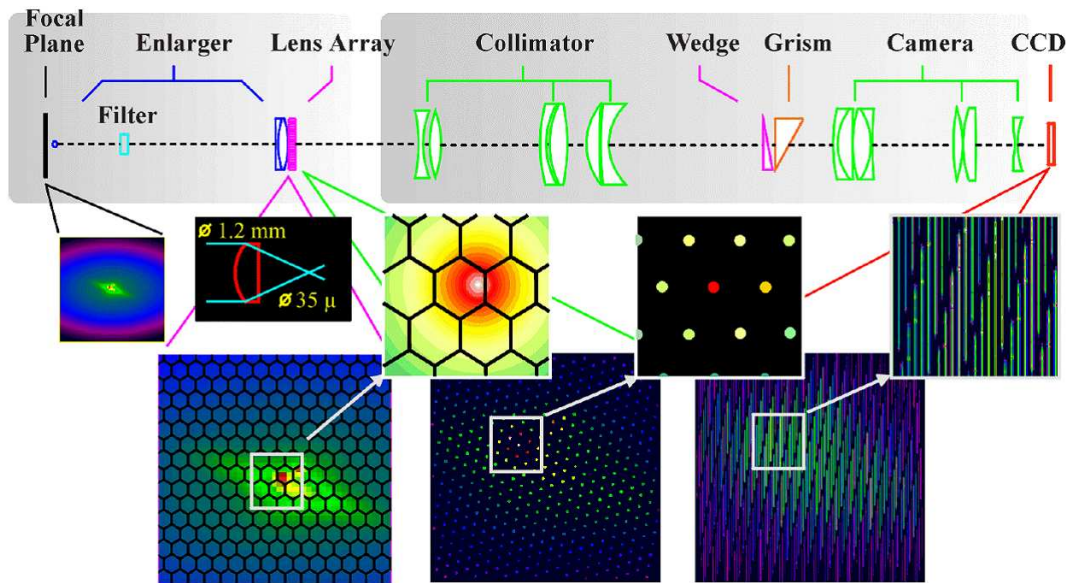


Figure 4.4: Example of a TIGER-type integral field spectrograph based on a microlens array. Sketch from Bacon et al. (2001).

requirements for the integral field spectrograph are a field of 1×1 arcsec², a sampling of about 30×10 mas in K -band and a spectral resolution $R \approx 4000$.

- **Pre-optics:** The field magnifier optics adapts the focal length of the telescope such that the 1.8×0.6 mm rectangular microlens pitch matches the field sampling at 0.03×0.01 arcsec. This requires an effective focal length of $\sim 1 \times 10^4$ mm, corresponding to a magnification of 16:1 over the LINC focal plane.
- **The IFU:** The sampling of the field is performed by an array of rectangular microlenses of $60 \text{ mm} \times 60 \text{ mm}$ size with a sampling of about $1.8 \text{ mm} \times 0.6 \text{ mm}$. The output of the microlenses is an array of micropupils. The microlens focal length is 7.6 mm and the micropupil size is equal to $\sim 15 \mu\text{m} \times 45 \mu\text{m}$. The micropupils have an elliptical shape (see Section 5.3.3.2, Figures 5.9 and 5.10).
- **The spectrograph:** The spectrograph section consists of a collimator, the dispersive element and a camera. These elements reimage and disperse the light from the micro-pupils on the detector. The pupil of the spectrograph section is determined by the shape of the microlenses. The spectrograph section has a magnification of 2 which results in a pupil image diameter in the low-resolution direction of $30 \mu\text{m}$ i.e. about 2 pixels of the detector. The spectrograph design is adjusted to get a beam diameter of 10 mm at the dispersing element. The

collimator has a focal length of 127 mm and an aperture of $f/12.7$. The microlens system provides telecentric beams. The camera has a focal length of 260 mm and $f/26$ aperture. Various types of dispersing elements (diffraction grating, grism, Volume Phase Holographic Grating) can be inserted in the intermediate pupil, between collimator and camera. The required high spectral resolution R of about 4000 can be obtained by a diffraction grating covering the 1.95-2.35 μm spectral range. It has 200 grooves/mm. The required incident angle, which is also the grating angle, is 26° .

It is important to point out that this design is based on a rectangular microlens array. The other possible solution is to place additional optics with an anamorphic magnification in front of square or hexagonal microlenses. The effects of anamorphic magnification in both of the selected approaches will be discussed in Chapter 5.

4.5.3 Status of the project

The SERPIL/LIINUS project was initiated in January 2006. Since then, a concept study phase - or equivalently a Phase A study - has been carried out by the member institutions (MPE, University of Cologne and the MPIA Heidelberg). Soon after the project was started, it became obvious, that SERPIL/LIINUS would not replace LINC at the telescope and therefore it will be built within the LINC/NIRVANA hardware. This focused our investigations on the lenslet+fibers approach and the compact spectrograph design inside LINC/NIRVANA cryostat. In order to demonstrate that building a spectrograph inside LINC is feasible, a preliminary optical design employing a microlens array IFU was first developed (Section 4.5.2). This could marginally succeed in fitting the spectrograph inside LINC and fulfilling the top level requirements. However, as the LINC/NIRVANA final design is not yet completed, the available size for the spectrograph is not yet a fixed parameter. The next step was to find out an optical path inside LINC that will bring the light from LINC's original focal plane at the bottom of the cryostat to the upper section where some empty space is available for upgrades such as SERPIL/LIINUS (Section 5.4.2). Once this path was found, the necessary modifications to LINC have been discussed, and currently the design of the relay optics is being carried out.

A parallel work has been the design using a lenslet+fibers IFU. Since July 2006 our efforts have been focused to investigate the coupling of the telescope's double pupil to optical fibers. Numerical simulations have been developed for that purpose using the Interactive Data Language (IDL) and the optical design software "Zemax". The results from the simulations are discussed in the next Chapter of this thesis. This theoretical work is being currently validated under non-ideal conditions in a laboratory at the MPE.

The concept study phase is expected to be finished in May 2008. A technical proposal will be written and presented to the LBT consortium during the third quarter of 2008. Independently of the chosen approach for the final design, SERPIL/LIINUS

could be built in relatively short timescales, suggesting that it could be installed at the telescope soon after LINC/NIRVANA starts operations in the beginning of 2011.

Chapter 5

Coupling light into optical fibers at focal- and pupil-planes: implications for the design of interferometric instruments at the LBT

This chapter is an almost exact reproduction of the following publication:

- “Coupling light into optical fibers at focal- and pupil-planes: implications for the design of interferometric instruments at the LBT”
Müller Sánchez, F., Eisenhauer, F., Genzel, R., Gál, C., Krabbe, A., & Herbst, T. 2008c, ApJS, to be submitted

5.1 Introduction

Novel and interesting observations can be achieved by combining optical interferometry and integral field spectroscopy (IFS). The Large Binocular Telescope (LBT) offers the possibility to directly apply both techniques simultaneously. While interferometry can be used to obtain high resolution images, integral field spectroscopy can be applied to produce a spectrum for every pixel in this high resolution field. A design study exploring technical solutions for diffraction limited interferometric integral-field spectroscopy at the LBT has been undertaken by the MPE, the University of Cologne and the MPIA under the name of SERPIL/LIINUS (Spectrograph for Enhanced Resolution Performing Imaging interferometry on the LBT / LINC-NIRVANA Interferometric Imaging Near-infrared Upgrade Spectrograph) (Gál et al. 2006). The goal of this project is to expand the capabilities of the present near-infrared imaging camera LINC (LBT Interferometric Camera) (Herbst et al. 2000) with spectroscopy by means of an integral field unit (IFU) located inside the LINC cryostat. The spectrometer could be then placed either inside the LINC hardware or in a new cryostat by transporting the light via optical fibres. The several possibilities for IFS in the context of SERPIL/LIINUS are analyzed in Gál et al. (2006). In this paper we concentrate on the Lenslets + Fibers solution as it represents the most flexible approach, and study in more detail the coupling of interferometric light to optical fibers.

The principle of the lenslet+fiber IFU for SERPIL/LIINUS is shown schematically in Figure 5.1. The telescope focal plane is imaged on the front curved surface of the microlenses. Each microlens forms a telescope pupil image on its back flat surface, where the fiber is attached. The input microlenses are arranged in a close-packed two-dimensional array to obtain a filling factor close to unity. Each micropupil is then transported by fibers from the LINC hardware to another cryostat, which contains the necessary elements of a conventional spectrograph. At the output of the fiber, a pseudoslit can be formed, which can be directly fed to the spectrograph.

In this approach, the fibers play a very important role in the performance of the whole instrument, and therefore special attention should be given to their physical properties. Optical fibers have been widely used in astronomy for integral field spectroscopy in several instruments – Hexaflex (Arribas et al. 1991), GMOS (Allington-Smith et al. 2002), VIMOS (Le Fevre et al. 2000), CIRPASS (Parry et al. 2004) – and in optical interferometers (Coudé du Foresto et al. 1998; Petrov et al. 2000; Perrin et al. 2004). The majority of fiber-fed instruments so far have been designed for operation under natural seeing conditions using multi-mode fibers. However, in the case of SERPIL/LIINUS, where light will be transported at ambient temperatures (see Figure 5.1) the background radiation should be as low as possible, and that can only be achieved by employing single-mode fibers. However, feeding an instrument with single-mode fibers has other difficulties. Coudé du Foresto et al. (2000) have shown that the theoretical maximum efficiency with which a stellar image can be coupled

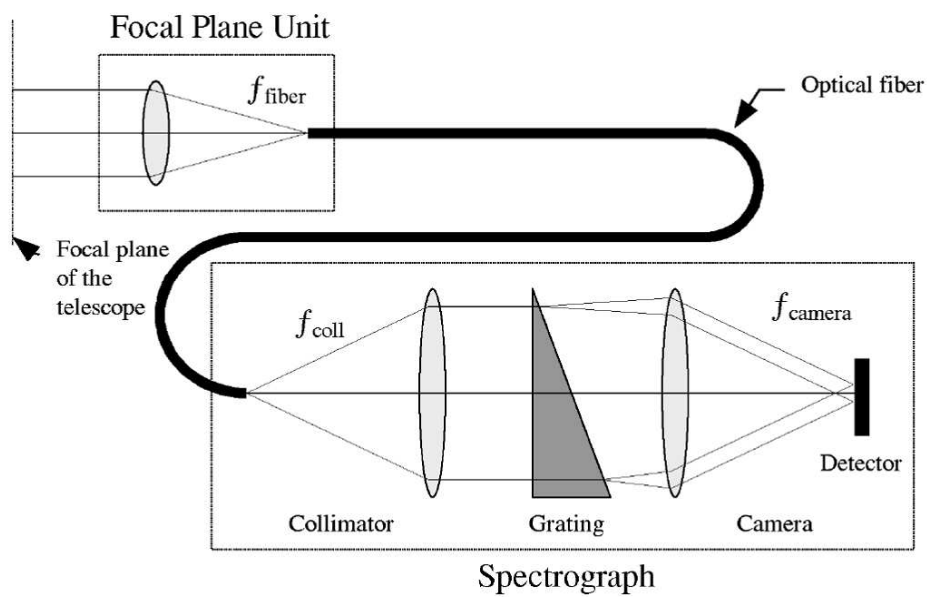


Figure 5.1: Instrument concept of a Lenslet+Fibers integral-field spectrograph (sketch from Kenworthy et al. 2001). In the context of the SERPIL/LIINUS project, the Integral Field Unit or Focal Plane Unit is located inside the LINC cryostat.

into a single-mode fiber in the absence of any atmospheric turbulence effects or obstructions in the telescope pupil is $\sim 82\%$. This is a natural limitation imposed by the mismatch of the electric field distribution of the telescope pupil and the fundamental propagation mode in a single-mode fiber. The existence of any type of turbulence or obstructions in the pupil further reduces the coupling efficiency in proportion to the Strehl ratio and the size of the central obstruction. However, the use of microlenses to focus the light into the fibers turns the situation to a pupil-plane coupling problem, and this has not been largely investigated. Horton & Bland-Hawthorn (2006) have shown that the image-plane coupling efficiency can be increased ($>90\%$) by using a few mode fiber with only 10 guided modes. Nevertheless, the background radiation from the fiber is also increased and its exact behavior has to be further investigated as well.

In this paper we present results from numerical simulations on pupil-plane and image-plane coupling to single- and few-mode fibers. The simulations were carried out not only for an interferometric configuration as the LBT but also for a single dish telescope. We discuss the main physical principles of imaging theory, interferometry and optical fibers in Section 5.2. We then describe the simulations in Section 5.3 and discuss the results for single and few mode fibers. In Section 5.4 we discuss the implications for the design of the integral-field spectrometer, including the effects of background radiation in the fiber on the performance of the instrument. Finally, the conclusions of the investigations are summarized in Section 5.5.

5.2 Optical Fundamentals

5.2.1 Imaging Interferometry on the LBT

Direct imaging in interferometry can be achieved by the Fizeau combination of beams (Fizeau 1868). In this type of interferometers, the wavefronts interfere in the focal plane, not in the pupil plane, as with most of the current interferometric instruments which perform Michelson beam combination (Keck-I, PTI, VLTI). The unique structure of the LBT allows the possibility to perform Fizeau interferometry and therefore to obtain true images (Herbst 2003). The fundamentals of Fizeau interferometry are summarized in this subsection.

Although electromagnetic waves possess inherently a vector-like character, one can turn to a scalar theory for an adequate description of the optical phenomenon of interest here, e.g., propagation through a turbulent medium and diffraction at a telescope aperture. The treatment of light as a wave is considerably simplified as one neglects the coupling between the electric and magnetic vectors, and the basic result given below is known as the Fresnel-Kirchoff theory of scalar diffraction:

$$E_1(x, y, z) = \frac{iA_1}{2\lambda} \frac{e^{ik\rho_1}}{\rho_1} \iint_{O_1} \frac{e^{iks_1}}{s_1} [\cos \alpha - \cos \theta] ds_1 \quad (5.1)$$

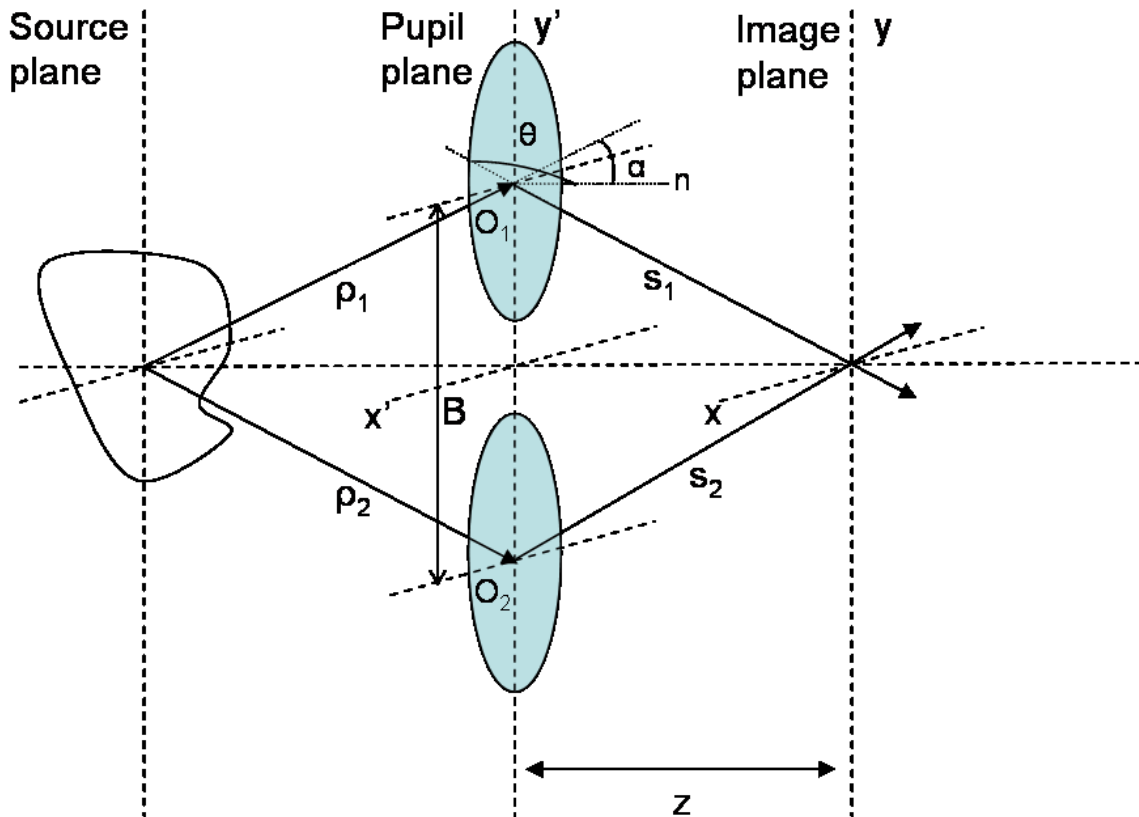


Figure 5.2: Geometry of the Fresnel-Kirchoff equation for a double pupil configuration similar to the LBT.

In Figure 5.2 the geometry of the diffraction integral is presented for a double pupil configuration similar to the LBT. We will first summarize the mathematical treatment for a single disk with aperture O_1 . The interferometric behavior will be then studied at the end of this subsection. The integral relates the field amplitude produced by a monochromatic light source (with wavenumber $k = 2\pi/\lambda$ and amplitude A_1) located at the source plane, to the field at the focal plane of the telescope with an aperture O_1 . The derivation is omitted here but can be found in the literature on physical optics, for instance in Born & Wolf (1980). The complex exponentials are two spherical Huygens elementary waves traversing distances ρ_1 and s_1 at angles α and θ respectively from the normal vector n to the pupil plane, and the cosines represent an obliquity factor. The resultant field at the focal plane is then just a superposition of the contribution of numerous such elementary waves from each point on the aperture according to the Huygens-Fresnel principle.

Generally, this diffraction integral is nontrivial and therefore it is convenient to introduce some approximations. In any astronomical observation the source will be a

distant object, and the diffracting aperture will consist of a telescope with an aperture that is many orders of magnitude smaller than the distance to the source, reducing the obliquity factor to approximately 2. An expansion of the aperture-image distance s_1 in Eq. 5.1 to first order allows the diffracted field at the focal plane to be written as:

$$E_1(x, y, z) = -\frac{ie^{ikz}}{\lambda z} \iint_{-\infty}^{\infty} E_1(x', y') e^{\frac{ik}{2z} [(x'-x)^2 + (y'-y)^2]} dx' dy' \quad (5.2)$$

The two dimensional coordinates (x, y) and (x', y') are introduced for, respectively, the diffracted field in the image plane and the field at the aperture, and z is the horizontal distance from the aperture to the focal plane. This is the Fresnel approximation, or near-field diffraction, valid for $x'^2 + y'^2 \ll z^2$ and $x^2 + y^2 \ll z^2$. The field $E_1(x', y')$ in this scenario is the incoming plane wavefront multiplied by the pupil transmission function. By rearranging terms and defining the function:

$$f(x, y, z) = -\frac{ie^{ikz}}{\lambda z} e^{\frac{ik}{2z}(x^2 + y^2)} \quad (5.3)$$

the Fresnel diffraction integral can be expressed as:

$$E_1(x, y, z) = f(x, y, z) \iint_{-\infty}^{\infty} E_1(x', y') e^{-i2\pi\left(\frac{xx'}{\lambda z} + \frac{yy'}{\lambda z}\right)} e^{\frac{ik}{2z}(x'^2 + y'^2)} dx' dy' \quad (5.4)$$

or equivalently

$$E_1(x, y, z) = f(x, y, z) \mathcal{F} [E_1(x', y') e^{\frac{ik}{2z}(x'^2 + y'^2)}] \quad (5.5)$$

where \mathcal{F} stands for the two-dimensional Fourier transform

Additionally, if the plane of observation is far away from the diffracting aperture, the formula for Fresnel diffraction can be simplified even further. If the criterion $k(x'^2 + y'^2)_{max}/2 \ll z$ is fulfilled, the exponential in the last expression for Fresnel diffraction Eq. 5.5 becomes ~ 1 and the diffracted field is simply:

$$E_1(x, y, z) = f(x, y, z) \mathcal{F} [E_1(x', y')] \quad (5.6)$$

Disregarding the function $f(x, y, z)$, which is just a multiplicative factor containing amplitude and phase, the field in the image plane becomes proportional to the Fourier transform of the field at the pupil plane. This is the Fraunhofer or far-field approximation, which is generally valid for astronomical applications.

By means of the Fraunhofer approximation and under incoherent conditions, the imaging system can be characterized by its point spread function (PSF), which describes how a point source is imaged through an optical system and it is proportional to the Fourier transform of the electric field in the exit-pupil plane. In the ideal case of perfect imaging without any aberration effects, the result will depend only on the geometrical shape of the aperture.

Consider the basic example where the pupil function is just a circle, as one of the apertures in Figure 5.2, $O_1(x', y') = \text{circ}(r')$ where $x'^2 + y'^2 = r'^2$. To obtain the PSF one first has to take the Fourier transform of this. For a disc of diameter D_1 this is given by:

$$E_1(x, y) = E_0 \left[\frac{2J_1(\pi D_1 r / \lambda z)}{\pi D_1 r / \lambda z} \right] \quad (5.7)$$

where E_0 is the electric field amplitude received from the source at the pupil, $x^2 + y^2 = r^2$ and J_1 is the first-order Bessel function. Taking the square of this and dividing by E_0 produces the normalized PSF for a diffraction limited telescope without central obscuration, also known as the Airy pattern.

Consider now the interferometric configuration with two circular apertures as shown in Figure 5.2. For this case, the pupil can be expressed as:

$$E(x', y') = \text{circ}(r') \delta(y' - B/2) + \text{circ}(r') \delta(y' + B/2) \quad (5.8)$$

where B is the distance between the centers of the two telescopes, or baseline, and δ is the Dirac function. The electric field distribution at the focal plane of the telescope will be given by the Fourier transform of this and has the form:

$$E(x, y) = E_0 \left[\frac{2J_1(\pi D_1 r / \lambda z)}{\pi D_1 r / \lambda z} \right] 2 \cos(\pi B y / \lambda z) \quad (5.9)$$

The LBT PSF is obtained by taking the square of this expression

$$PSF_{LBT}(x, y) = E_0^2 \left[\frac{2J_1(\pi D_1 r / \lambda z)}{\pi D_1 r / \lambda z} \right]^2 2 [1 + \cos(\pi(2B)y / \lambda z)] \quad (5.10)$$

Figure 5.3 shows the interferometric PSF of such a configuration based on the LBT parameters. Some important conclusions can be gleaned from this. First, only one direction of the image is affected by the cosine function, which is the high resolution direction as $B > D_1$. The Airy pattern modulates this function in the high resolution direction and is undisturbed in the low resolution direction. In this direction the width of the Airy disk, which is the distance at which the central peak encounters the first zero, occurs when $W_1 = 2.44\lambda/D_1$. In the high resolution axis, the width of the central peak is given by $W_2 = 2\lambda/(2B)$. Notice that in this case the resolution is given by two times the distance between the centers of the telescopes.

For an IFU as shown in Figure 5.1, the telescope pupil is projected by the microlens located at the telescope's focal plane onto the fiber entrance. In this application, the microlens acts as a spatial filter which cuts the image of a point source depending on the spatial sampling, and produces a micropupil at the microlens focal plane which by means of the far-field approximation and for a rectangular shaped microlens is given by

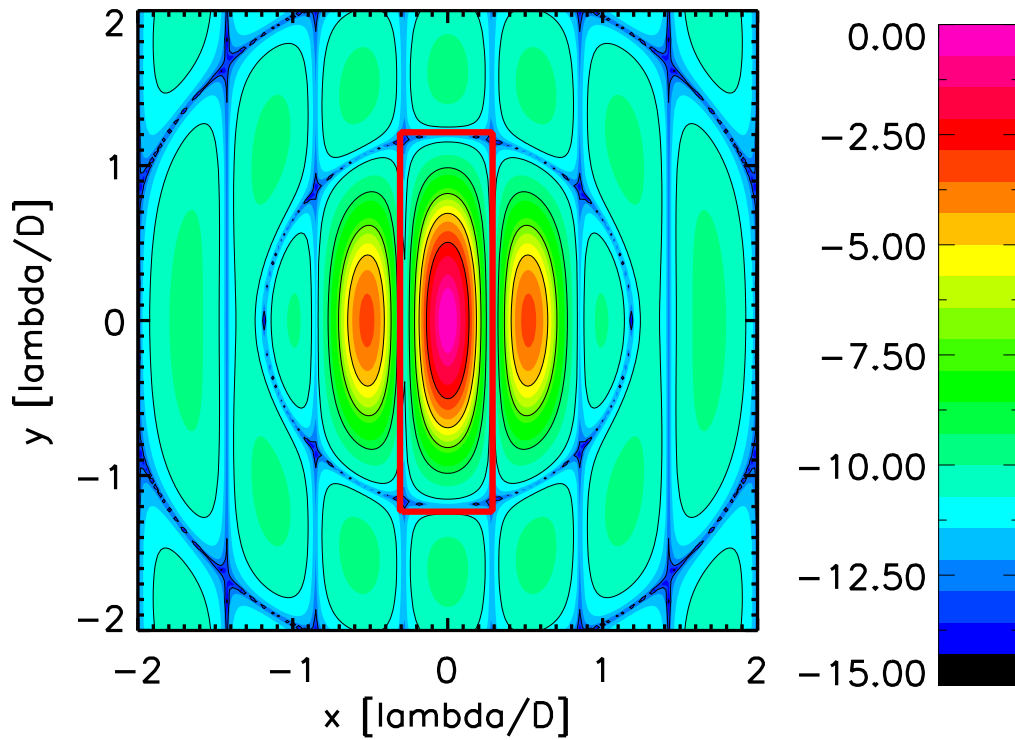


Figure 5.3: Point Spread Function of the interferometric configuration of the LBT. The combination of the two beams in the focal plane of the telescope produces an elongated PSF. The interferometric resolution direction corresponds to the x-axis, while the low resolution direction (one single dish) corresponds to the y-axis. The coordinates are given in multiples of $[\lambda/D]$, where “ λ ” is the wavelength and D is the Diameter of a single dish. The red rectangle delinates the central peak of the PSF and represents a possible spatial sampling using a rectangular microlens.

$$E_f(x_f, y_f) = \mathcal{F} [E(x, y) \text{rect}(l_x, l_y)] \quad (5.11)$$

where the subscript f stands for spatial coordinates at the fiber's entrance plane (or equivalently the microlens focal plane), \mathcal{F} indicates two-dimensional Fourier transform and **rect** is the two-dimensional rectangular function of size $l_x \times l_y$. Notice that the microlens could have in principle any geometrical shape. For another type of microlens, the adequate filter function should be substituted in Eq. 5.11 instead of the rectangular function. This was chosen for our investigations due to the symmetry of the central peak of the LBT PSF.

5.2.2 Theory of fibers

From a geometrical point of view, an optical fiber is formed by a thin cylindrical stick of a dielectric material (core) with refractive index n_1 , which is surrounded by another dielectric material (cladding) of refractive index $n_2 < n_1$. The laws governing the propagation of light in optical fibers are Maxwell's equations treated in a similar way as for dielectric waveguides (Neri 1999). The allowed distributions of the electromagnetic field across the fiber are referred to as the modes of the fiber. When the number of allowed modes becomes large, as is the case with large diameter fiber cores, geometrical optics gives an adequate description of light propagation in fibers. However, this approximation does not hold for fibers where the core size is smaller than ~ 50 times the wavelength and it becomes necessary to solve the wave equation in cylindrical coordinates for the electric field. The solutions, which are found to be harmonic in space and time, are of the form (Neri 1999):

$$E_f(r, \phi, z) = f(r) \cos(\omega t - \beta z + \gamma) \cos(q\phi) \quad (5.12)$$

where ω is the angular frequency of the light in rad s^{-1} , β is the propagation constant in rad m^{-1} , γ is a phase constant to provide the correct amplitude at time $t = 0$ and position $z = 0$, and q is an integer. Solutions for β , $f(r)$, and q are obtained by substituting Eq. 5.12 into the wave equation. The solutions will depend on the particular fibre geometry and index profile, including both the core and the cladding. Through the paper, fibers with a step-index profile for which exact solutions can be obtained, will be considered. For a rigorous mathematical treatment of the solutions we refer to Gloge (1971). For this case, the solutions for $f(r)$ are Bessel functions inside the core, and modified Hankel functions outside the core. In addition, when the fractional refractive index difference $\Delta = (n_1 - n_2)/n_2$ is much smaller than one, i.e. $\Delta \ll 1$, the exact solutions of the waveguide theory can be replaced by a set of modes which are linearly polarized, called the LP modes. These LP modes are combinations of the modes found from the exact theory of waveguides. In practice this is a reasonable approximation for a real fiber, as the difference in refractive indices is generally < 0.01 and the resulting error in mode characteristics is $< 0.1\%$. The LP

modes are characterized by two subscripts, m and n . The first subscript, m , gives the number of azimuthal, or angular, nodes (zeroes) that occur in the electric field distribution of the mode; while n gives the number of radial nodes that occur inside the core. The transverse component of the electric field of the LP_{mn} mode is then given by:

$$E_{mn}(r, \phi) = E_0 \left[\frac{J_m(u_{mn}r/a)/J_m(u_{mn})}{K_m(w_{mn}r/a)/K_m(w_{mn})} \right] \cos(m\phi) \quad (5.13)$$

where a is the core radius, J_m is the Bessel function of the first kind of order m and K_m is the corresponding modified Hankel function of the second kind. For small Δ , the longitudinal components are small compared to the transverse components and for our purposes can be neglected. The propagation constant β of any mode of this fiber is limited within the interval $n_2k > \beta > n_1k$, where $k = 2\pi/\lambda$ is the wavenumber in free space. The parameters u and w are defined as:

$$\begin{bmatrix} u \\ w \end{bmatrix} = \begin{bmatrix} a\sqrt{k^2n_2^2 - \beta^2} \\ a\sqrt{\beta^2 - k^2n_1^2} \end{bmatrix} \quad (5.14)$$

And the quadratic summation of them leads to a third parameter:

$$V = \sqrt{u^2 + w^2} = ak\sqrt{n_2^2 - n_1^2} = \frac{2\pi a\text{NA}}{\lambda} \quad (5.15)$$

where NA is the numerical aperture of the fiber defined as $\sqrt{n_2^2 - n_1^2}$ and V is called the normalized frequency, or simply, the V -number of the fiber. This is an important quantity in fiber theory because it helps to determine easily which modes of the electromagnetic field will be supported by a given fiber. When the V -number is lower than 2.405 (the value at which the first zero of the zero-order Bessel function occurs), only a single mode will propagate in the fiber, the LP_{01} mode. This has a cut-off frequency of $V_c = 0$ and is also known as the fundamental mode of the fiber because it is always present. When $V > 2.405$ the next linearly polarized mode, LP_{11} , can be supported by the fiber, so that both the LP_{01} and LP_{11} modes will propagate. For a fiber with a V -number of 3.832 (corresponding to the first zero of the first-order Bessel function), two more linearly polarized modes can propagate: the LP_{21} and the LP_{02} modes. The cutoff frequencies of the first ten LP modes are shown in Table 5.1.

5.2.3 Coupling efficiency

When employing optical fibers to transport light, it is important to know how much light can be coupled into it. In general, the coupling efficiency η is defined as the ratio of the light power P_c coupled into the fiber relative to the light power P_i at the entrance of the fiber

$$\eta = \frac{P_c}{P_i} \quad (5.16)$$

Number of modes	m	n	V_c
1	0	1	0.000
2	1	1	2.405
3	0	2	3.832
4	2	1	3.832
5	3	1	5.136
6	1	2	5.520
7	4	1	6.380
8	0	3	7.016
9	2	2	7.016
10	5	1	7.588

Table 5.1: Cutoff frequencies of the first ten linearly polarised modes of a step index fiber.

Based on this concept, one can define the modal fiber coupling receiver efficiency η_{mn} as a normalized overlap integral between the electric field distribution of the fibre mode E_{mn} and that of the incident beam E_i

$$\eta_{mn} = \frac{\left| \iint_{-\infty}^{\infty} E_i^*(x, y) E_{mn}(x, y) dx dy \right|^2}{\iint_{-\infty}^{\infty} |E_i(x, y)|^2 dx dy \iint_{-\infty}^{\infty} |E_{mn}(x, y)|^2 dx dy} \quad (5.17)$$

The incident field distribution E_i is proportional to $\mathcal{F}[E(x', y')]$ in the case of coupling at the telescope focal plane and, is given by Eq. 5.11 for coupling at the pupil plane. In both cases the asterisk indicates complex conjugation and the integrals are performed over an infinite plane. The total coupling efficiency η will be then given by summing all η_{mn} .

5.3 Results

5.3.1 Description of the simulations

In the numerical analysis described here we simulate the LBT configuration to obtain interferometric diffraction limited images that are coupled into step index single- and few-mode fibers located at both, the focal plane of the telescope and at the focal plane of the microlenses. The latter simulates the pupil-plane coupling for the proposed lenslet+fibers integral-field unit. As a byproduct, we investigate the same coupling scenarios for a single-dish telescope. All simulations were carried out using the Interactive Data Language (IDL) and the optical design software ZEMAX.

The LBT optics are simulated numerically as a complex array of $N \times N$ elements

by assuming a pixel scale S_1 in [m pixel⁻¹] such that after applying the Fourier transform, it produces in the image plane a PSF with a spatial angular sampling of 1 [mas pixel⁻¹]. The optics of the telescope incorporate two 8.4-meter mirrors on a 14.4 meter center-to-center single common mount. Then for the case of image-plane coupling, we optimize in our simulations the focal length to maximize the coupling efficiency to the fiber. The fiber is characterized by its normalized frequency which determines the number and form of the guided modes, as well as the fiber core's diameter for any given wavelength and NA. Based on the requirements of SERPIL/LIINUS, we have chosen an effective wavelength of $\lambda = 2.2 \mu\text{m}$, which is the center of the *K*-band, and NA=0.17, which is a typical value for fluoride-glass fibers working in the near-infrared (Ihle 2006). These two parameters (λ and NA) fix the diameters of the fibers corresponding to single-mode fibers with 10 μm core diameter and 10-mode fibers with 31 μm core diameter.

For the case of pupil-plane coupling, we cut the electric field at the focal plane of the telescope according to the lenslet size and shape, and then calculate the field at the focal plane of the lenslet. The micropupil in this plane is obtained numerically by applying Eq. 5.11. In this configuration we look for the optimum microlens focal length which maximizes the coupling efficiency to the fiber for any given size of the microlens.

5.3.2 Focal-Plane coupling

5.3.2.1 Single-dish telescope

The problem of coupling the electric field distribution of a point source to single- and few-mode fibers in the focal plane of a single telescope has been investigated before (Shaklan 1988, Coudé du Foresto et al. 2000, Horton & Bland-Hawthorn 2006). Our results confirm previous findings, which can be summarized as follows: 1) the maximum coupling efficiency onto single-mode fibers is $\sim 82\%$, 2) a fiber with 10 guided modes increases the maximum coupling efficiency up to $\sim 95\%$, 3) the optimum focal ratio F_{opt} is $1.4w_g/\lambda$ for single-mode fibers (Neumann 1988), where w_g is the Gaussian waist of the fundamental mode approximated from the fiber core radius as $w_g = 1.1a$, and 4) the optimum focal ratio for few-mode fibers can be approximated by $F_{opt} \approx 1/(2NA)$.

5.3.2.2 LBT's double pupil

For this case, the intensity of the interferometric electric field distribution at the focal plane is given by the telescope's PSF shown in Figure 5.3. The dependence of coupling efficiency on fiber normalized frequency and wavelength of operation will be investigated. The physical property that was first studied was the relationship between total maximum coupling efficiency and fiber normalized frequency, or equivalently, fiber core diameter. In order to do this, the coupling efficiency was optimized

against focal ratio for fibers with normalized frequencies in the range 0–7.016 (single- and few-mode fibers with up to 9 modes, see Table 5.1). To get a fuller picture of the effect of focal ratio and to show the optimization process, we calculated coupling efficiency for different focal ratios for four different fibers with normalized frequencies of 2.405 (single-mode), 3.832 (4 modes), 6.380 (7 modes) and 7.016 (9 modes). These values correspond to fibers with 10, 16, 26 and 29 μm core diameter for $\text{NA}=0.17$ and $\lambda = 2.2\mu\text{m}$. The results are shown in Figure 5.4. It is important to point out that due to the LBT configuration, two focal ratios must every time be considered, F_1 for the low resolution direction related to one $D_1 = 8.4$ m telescope, and F_2 for the high resolution direction corresponding to an equivalent $D_2 = 22.8$ m telescope. The ratio between them is ~ 2.71 . In Figure 5.4 only curves for F_2 are plotted. For a single mode fiber $V = 2.405$, the maximum coupling efficiency is achieved at $F_2 = 3.5$, corresponding to the theoretical value predicted in the case of coupling a single-dish image to a single mode fiber, given by $F_2 = 1.4w_g/\lambda$. This surprising result suggests that in a double-pupil configuration, the maximum coupling to a single-mode fiber is achieved for the focal ratio which best matches the electric field profile in the high-resolution direction with the LP_{01} mode.

The dependence of coupling efficiency on fiber normalized frequency is shown in Figure 5.5. As can be seen in this Figure, the maximum coupling efficiency for a single-mode fiber is $\sim 23\%$. As soon as the cut-off frequency of a certain mode is achieved, the mode starts propagating in the fiber. The curve then increases continuously with the appearance of some modes. The coupling efficiency for a 9-mode fiber is $\sim 83\%$. This behavior clearly suggests that few-mode fibers considerably improve the coupling efficiency in a similar way as for a single-dish telescope. However, in this case, the effect is much more pronounced due to the symmetry of the electric field distribution at the focal plane of the double-pupil telescope. In the single-dish case, the increments coincide with the cut-off frequencies of the LP_{02} and LP_{03} modes. For the LBT the LP_{21} , LP_{41} and LP_{22} contribute simultaneously with the LP_{02} and LP_{03} to the total coupling efficiency. The largest increment in the curve occurs at the cut-off frequency of the LP_{02} and LP_{21} modes. These two complement the LP_{01} to match the interferometric PSF of the telescope; while the LP_{01} couples well the central peak of the single-dish PSF in the low resolution direction, the LP_{02} couples properly the central peak of the two-telescopes PSF and at the same time the LP_{21} is a good match for the sidelobes of this PSF in the high resolution direction. These three modes can couple up to $\sim 70\%$ of the incoming light to the fiber.

The coupling to individual modes described above can be better understood by analyzing the electric field pattern of each specific mode. Figure 5.6 shows the electric field profiles of the first 12 guided modes of a multi-mode fiber. There is a fundamental mode (LP_{01}) with an approximately Gaussian distribution, and a number of higher-order modes with spatial profiles that can be classified according to their type of symmetry as even or odd functions. Notice that the LP_{0n} modes have circular symmetry and therefore cannot be treated in this manner. Based on this classification we

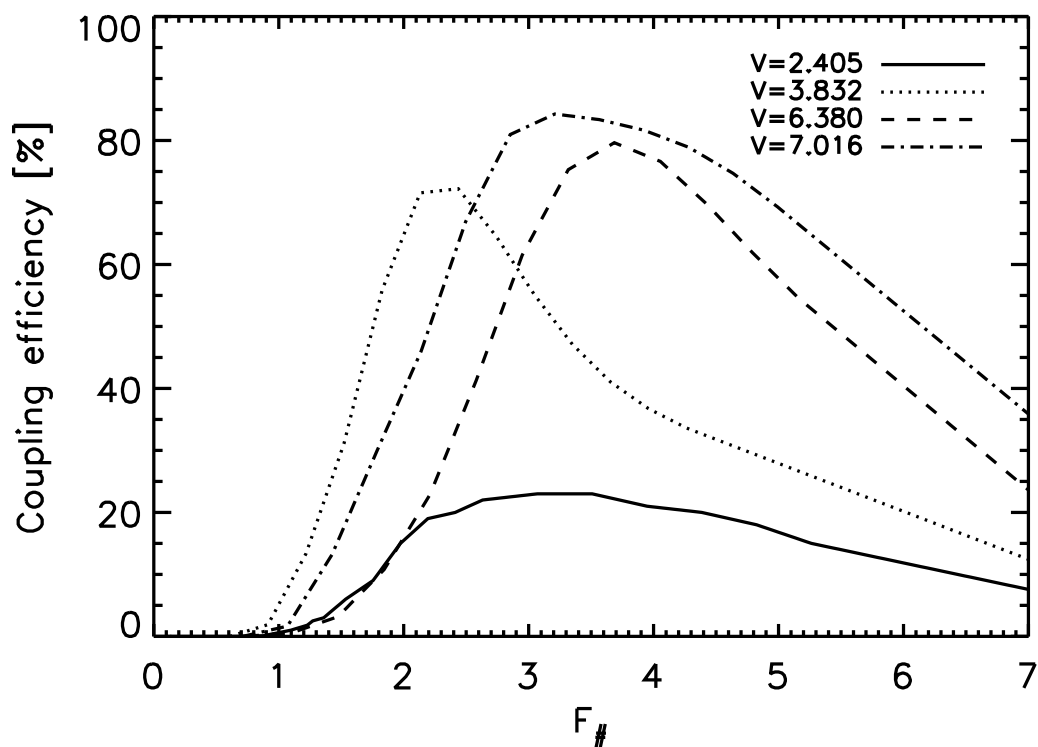


Figure 5.4: Coupling efficiency versus focal ratio. Case study: LBT focal plane coupling. The Focal Ratio axis in the Figure corresponds to F_2 or the focal ratio of an equivalent 22.8 m telescope. If the Focal Ratio axis is changed to show F_1 , the current F_2 -axis must be multiplied by a factor of ~ 2.71 . The solid line represents a single-mode fiber, the dotted line a fiber with 4 transmitting modes, the dashed line a fiber with 7 transmitting modes and the dotted-dashed line a fiber with 9 modes.

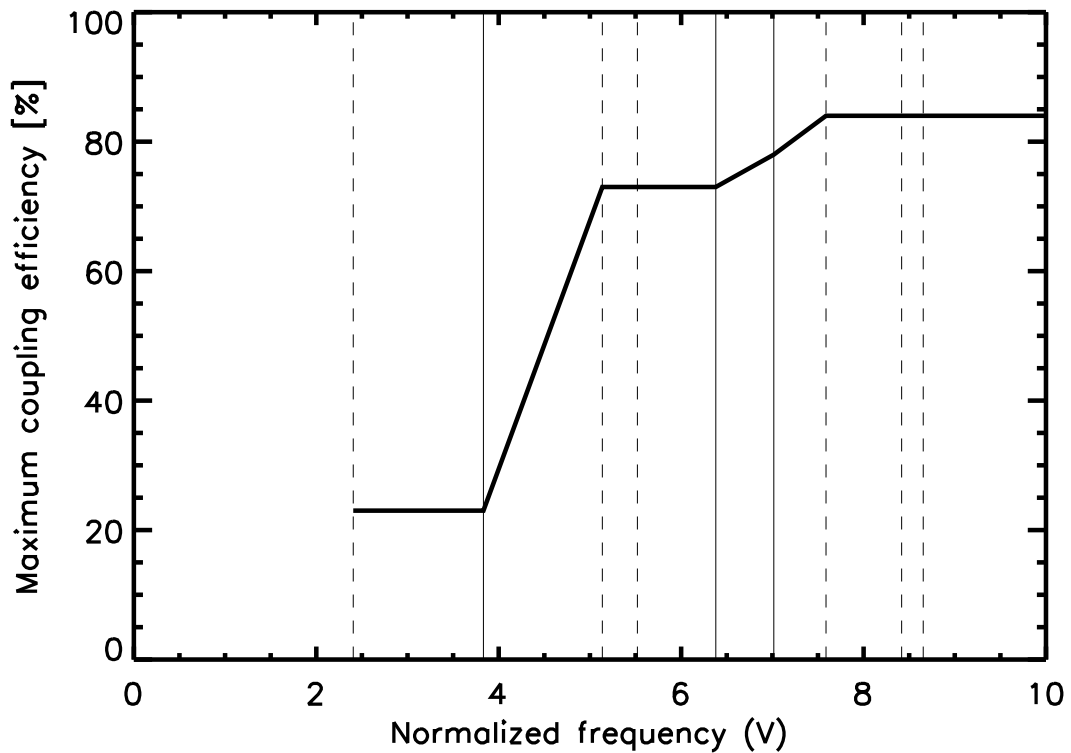


Figure 5.5: Maximum coupling efficiency versus normalized frequency (V). Case study: LBT focal plane coupling. For a given normalized frequency, the maximum coupling efficiency is obtained at the optimal focal ratio. The vertical dashed lines correspond to normalized frequencies of LP modes which do not couple light due to the symmetry of that mode. The vertical solid lines correspond to normalized frequencies of LP modes which couple incoming light into the fiber. The maximum coupling efficiency for a single mode fiber is $\sim 23\%$. For a fiber with $V = 3.832$ the LP_{02} and LP_{21} modes contribute with additional $\sim 50\%$ to the maximum coupling efficiency. For a fiber with $V = 6.38$ the LP_{41} mode increase the maximum coupling efficiency up to $\sim 80\%$ and finally in a fiber with $V = 7.018$ the LP_{03} and LP_{22} modes propagate and increase the maximum coupling efficiency up to 84% .

can conclude that the modes contributing to the total coupling of the LBT's electric field distribution are the LP_{0n} and the even modes (modes that are symmetric with respect to the y -axis, see Figure 5.6). For a single-dish, as the Airy pattern presents circular symmetry, only the LP_{0n} modes are capable of coupling its distribution.

Finally, we investigated the dependence of coupling efficiency on wavelength. The previous simulations have been carried out for a single wavelength. However astronomical applications such as SERPIL-LIINUS require good performance over a wide wavelength range. The results of these investigations are shown in Figure 5.7. This Figure shows maximum coupling efficiency as a function of wavelength for NA=0.17 fibers having their cut-off frequencies – 2.405 (single-mode), 3.832 (4 modes), 6.380 (7 modes) and 7.016 (9 modes) – at $2.2\mu\text{m}$. For each fiber, the focal ratio was fixed at the optimal value for $\lambda = 2.2\mu\text{m}$, then the wavelength was varied over the whole near-infrared ($1 - 2.6\mu\text{m}$). In all cases, light with wavelengths longer than the cutoff is coupled worse, since the number of the propagating modes are reduced, and the radius of the beam is mismatched (not optimal focal ratio). For shorter wavelengths, the maximum coupling efficiency is increased when certain modes start propagating in the fibers. In a single-mode fiber with LP_{01} mode cut-off at $2.2\mu\text{m}$, the increment in coupling efficiency is more pronounced around $1.4\mu\text{m}$ which corresponds to the LP_{02} and LP_{21} modes cutoff. However, as the image is not produced at the optimum focal ratio of the telescope, in the few-mode fibers the increments are less pronounced, translating in a wide range of wavelengths for which the coupling efficiency stays almost constant.

5.3.3 Pupil-Plane coupling

5.3.3.1 Single-dish telescope

A Lenslet+Fibers IFU uses an array of microlenses in front of the fibers to sample the field of view of the telescope. Each lenslet forms an image of the telescope pupil at the entrance of each fiber. There are a number of this type of IFUs operating already at 8-10 m class telescopes – SPIRAL (Kenworthy et al. 1998), GMOS (Allington-Smith et al. 2002), CIRPASS (Parry et al. 2004). All of these instruments have seeing-limited resolution and therefore work with multi-mode fibers. As the propagation of light inside multi-mode fibers can be treated using geometrical optics, the focal ratio of each lenslet can be easily determined by matching it to the NA of the fiber.

In this section, as an additional outcome on our investigations on the LBT, we present results on the coupling of a single telescope pupil into single- and few-mode fibers. The dependence of coupling efficiency on fiber normalized frequency, microlenses size and wavelength of operation will be investigated. To calculate these, the coupling efficiency was optimized against microlens focal ratio for different sizes of the microlenses and different fiber normalized frequencies. We decided to adopt a square geometry of the microlenses because it does not add complexity to the simulations originally prepared for the LBT, for which a rectangular geometry is mandatory

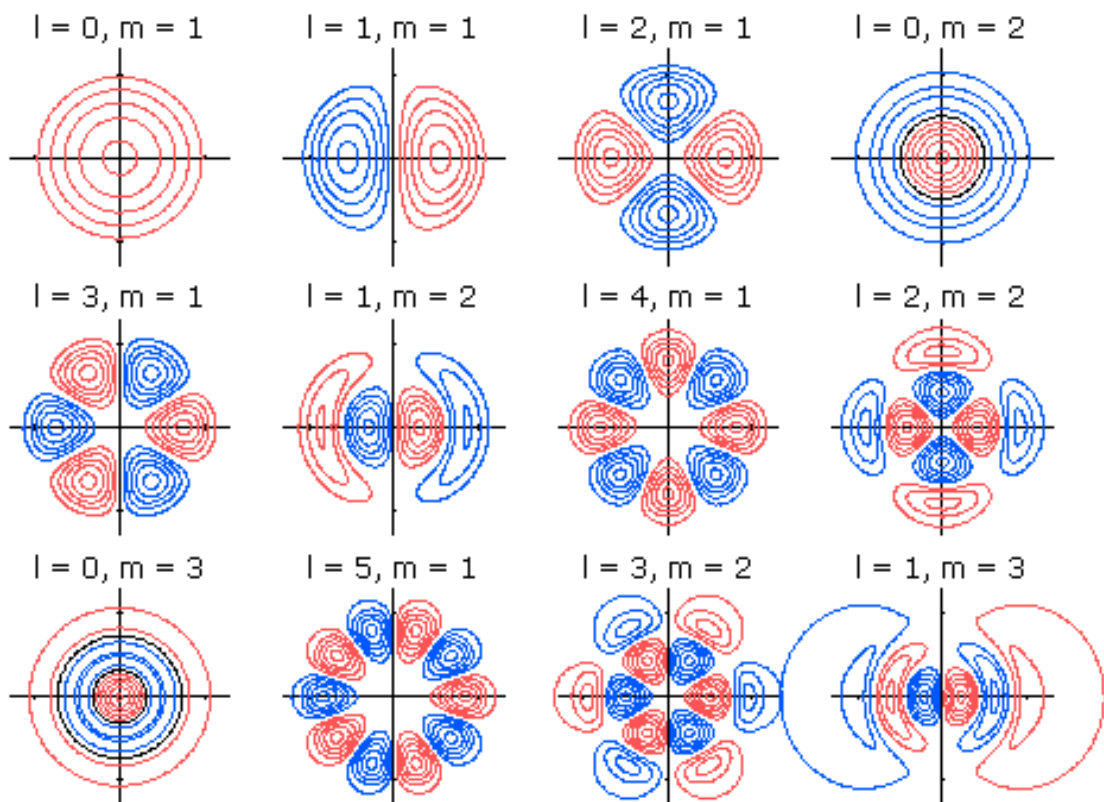


Figure 5.6: Electric field contour lines for the first 12 guided modes of an optical fiber. The red contours indicate positive values of the electric field. The blue contours represent negative values of the electric field.

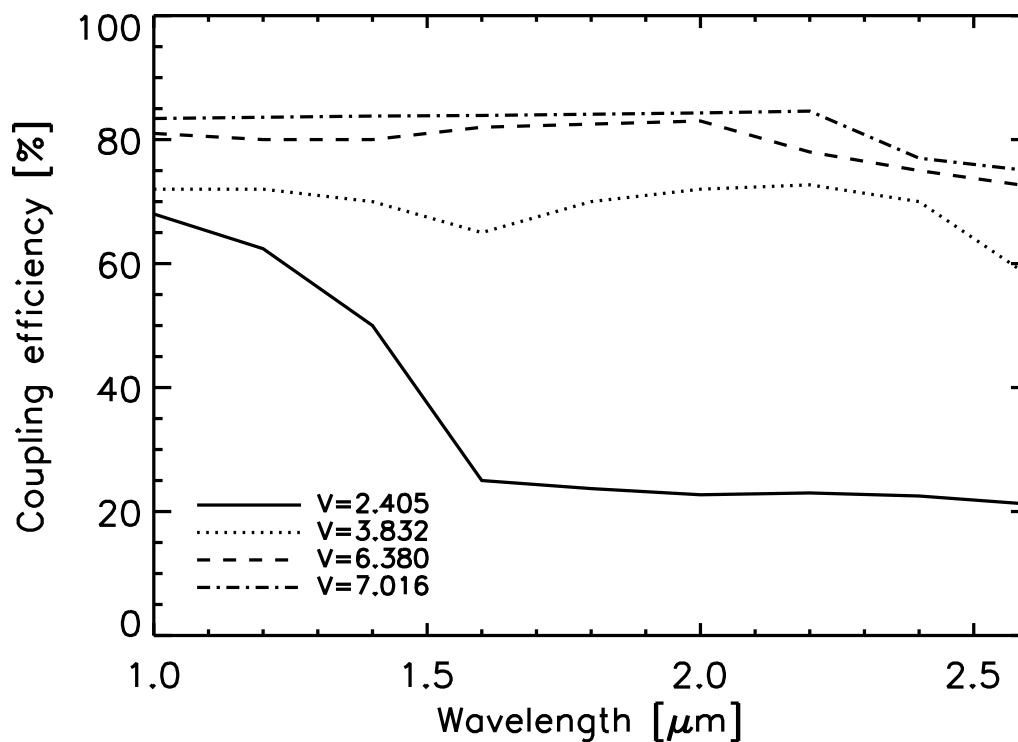


Figure 5.7: Coupling efficiency versus wavelength for $NA=0.17$ fibers having their cut-off frequencies at $2.2\ \mu\text{m}$. Case study: LBT focal plane coupling. For each fiber, the focal ratio was fixed at the optimal value for $\lambda = 2.2\ \mu\text{m}$. The studied wavelength interval covers the whole near-infrared range ($1 - 2.6\ \mu\text{m}$). The solid line represents a single-mode fiber at $2.2\ \mu\text{m}$, the dotted line a fiber with 4 transmitting modes at $2.2\ \mu\text{m}$, the dashed line a fiber with 7 transmitting modes at $2.2\ \mu\text{m}$ and the dotted-dashed line a fiber with 9 modes at $2.2\ \mu\text{m}$.

(see Section 5.3.3.2). The spatial sampling determines the size of each of the microlenses. We have considered samplings in the range 0.1 - 10 λ/D .

It is important to point out that the coupling efficiency in our investigations corresponds to the receiver coupling efficiency. According to Eq. 5.17 this is a parameter that measures the quality of the coupling between the electric field distribution that is present at the entrance of the fiber and the fiber modes. In the pupil-plane coupling scenarios this measures the amount of light coming from the microlens that goes into the fiber. The flux outside the microlens is not considered in this calculation and represents additional system losses. In the case of focal plane coupling, as there is no spatial filtering, the receiver coupling efficiency corresponds to the total coupling efficiency. For our purposes, the receiver coupling efficiency is the quantity of interest because it provides us with a measurement that directly compares the electric field pattern of the micropupils with the fiber modes. In addition, in a lenslet+fibers integral-field unit each microlens is surrounded by other equal elements forming a close-packed array. In the array there are basically no light losses, as the flux that could not be accepted by a particular microlens is contained in the neighbouring elements. Thus, along the paper we refer to receiver coupling efficiency just as coupling efficiency.

At first, the dependence of maximum coupling efficiency on the microlens size was investigated. The results for three types of fiber are shown in Figure 5.8. As it can be seen in this figure, the maximum coupling efficiency is $\sim 99\%$ and is achieved for a microlens size of $2.44 \times 2.44 [\lambda/D]$ and a fiber with $V = 7.016$, that is a nine-mode fiber. For a single-mode fiber $\eta_{max} \sim 97\%$. As the microlens size increases, the maximum coupling efficiency decreases steadily. This would be intuitively expected as the larger filter area (larger aperture), leads to a significant proportion of light falling outside the NA of the fiber. On the other hand, when the microlens size decreases, the maximum coupling efficiency decreases as well. This time the diffraction effects at the microlens take more importance and produce a wider beam which leads to light falling outside the core.

The dependence of maximum coupling efficiency on fiber normalized frequency for three different microlens sizes $0.61 \times 0.61 [\lambda/D]$, $1.22 \times 1.22 [\lambda/D]$ and $2.44 \times 2.44 [\lambda/D]$ is shown in Figure 5.9. As expected, the maximum coupling efficiency increases with the number of guided modes in the fiber, reaching efficiencies up to 99%. In this case, the appearance of the LP_{02} and LP_{03} modes give the increments to the maximum coupling efficiency.

Finally, we investigated the dependance of maximum coupling efficiency on wavelength. This time for each combination of spatial filter and fiber, the focal ratio was fixed at the optimal value for $\lambda = 2.2\mu\text{m}$, then the wavelength was varied over the whole near-infrared ($1 - 2.6 \mu\text{m}$). The results of these investigations are shown in Figure 5.10. This Figure shows maximum coupling efficiency as a function of wavelength for a microlens size of $2.44 \times 2.44 [\lambda/D]$ and for NA=0.17 fibers having their cut-off frequencies – 2.405 (single-mode), 3.832 (4 modes), and 7.016 (9 modes) – at $2.2\mu\text{m}$.

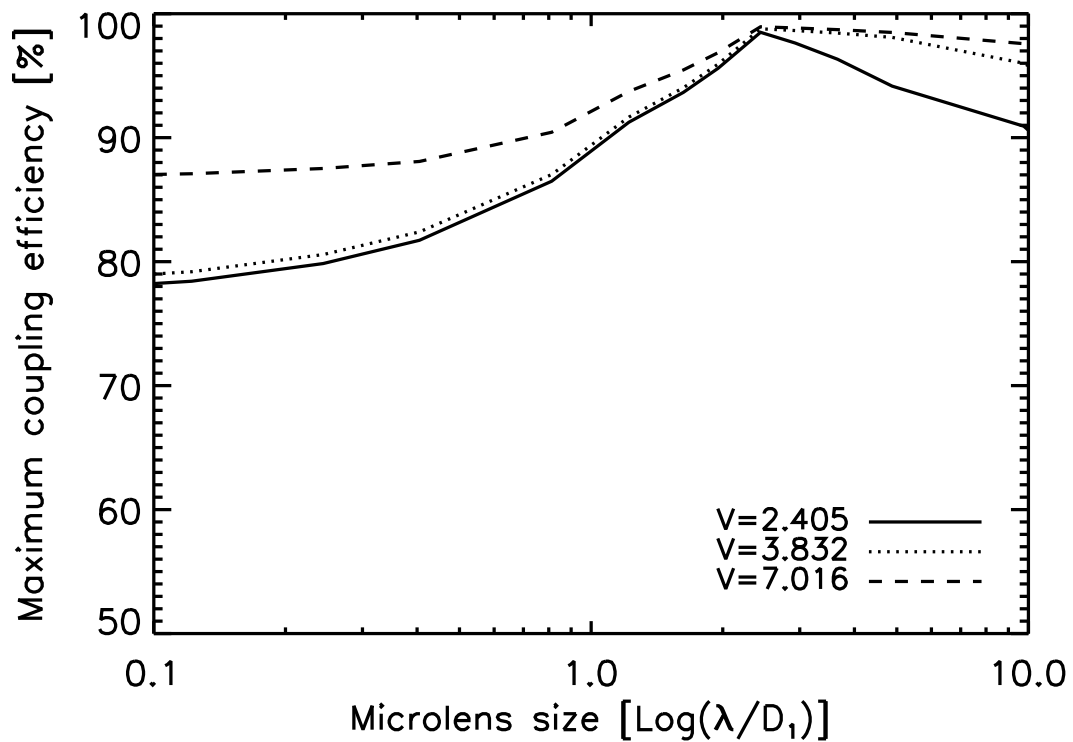


Figure 5.8: Maximum coupling efficiency versus microlens size. Case study: Single dish pupil plane coupling. The microlens has a square shape. Its size is given in units of $\text{Log}(\lambda/D_1)$ where λ is the wavelength and D_1 is the Diameter of the single dish. The coupling efficiency corresponds to the receiver coupling efficiency (see text for details). The solid line represents this relationship in a single-mode fiber, the dotted line in a fiber with 4 transmitting modes and the dashed line in a fiber with 9 modes.

For simplicity only the $2.44 \times 2.44[\lambda/D]$ case is shown, but the $0.61 \times 0.61[\lambda/D]$, $1.22 \times 1.22[\lambda/D]$ plots are similar. The general trend for the three types of fibers is an almost constant coupling efficiency with variations of $\sim 3\%$ over the near-infrared wavelength range.

5.3.3.2 LBT's double pupil

The most detailed analysis was carried out for this coupling scenario as it stands for one of the critical physical phenomena to investigate in the context of the SERPIL/LIINUS project. We present results on the coupling of a double 8.4 m telescope pupil into single- and few-mode fibers. The dependence of coupling efficiency on fiber normalized frequency, microlenses size and wavelength of operation will be investigated in a similar way as it was done for a single pupil. In addition, a few remarks on coupling in the non-ideal case will be discussed.

As can be seen in Figure 5.3, the central peak of the PSF of this interferometric configuration exhibits an elliptical morphology which can be well fitted by a rectangular shape of the lenslet. In Figure 5.11 the PSF of the telescope filtered by a rectangular microlens of size $2.0[\lambda/2B] \times 2.44[\lambda/D_1]$ is presented. This size was chosen to fully cover the central peak of the PSF. Notice that in the high resolution direction the first zero is reached at a distance $r = \lambda/2B$ in contrast to the low resolution direction for which this is reached at $r = 1.22[\lambda/D_1]$. This leads to a ratio between the two directions of ~ 4.2 . The micropupil produced by this configuration at the fiber's entrance is shown on Figure 5.12. The scale of the micropupil corresponds to that obtained at the optimal focal ratio which maximizes the coupling efficiency in a singlemode fiber of $10\mu\text{m}$ diameter.

The dependence of maximum coupling efficiency on the microlens size was investigated for four different types of fibers. The results are shown in Figure 5.13. As it can be seen in this figure, the maximum coupling efficiency for a single-mode fiber is $\sim 60\%$ and is achieved for a microlens size of $2.0[\lambda/2B] \times 2.44[\lambda/D_1]$. As the microlens size increases, the maximum coupling efficiency decreases rapidly. Notice that the ratio of the two directions is always kept constant. When the microlens size reaches $4.0[\lambda/2B] \times 4.88[\lambda/D_1]$, the decay of coupling efficiency is less pronounced because at this point the central peak of the low resolution direction becomes more important. On the other hand, when the microlens size decreases, the maximum coupling efficiency decreases progressively as well. However, as can be seen in Figure 5.13, the coupling efficiency is less sensitive to this decrement reaching a minimum of $\sim 48\%$. The curves of the other fibers under study present a similar dependence on the microlens size but with higher coupling efficiencies, e.g. for a 9-mode fiber the maximum coupling efficiency increases up to 90%.

The dependence of maximum coupling efficiency on fiber normalized frequency for three different microlens sizes $0.5[\lambda/2B] \times 0.61[\lambda/D_1]$, $1.0[\lambda/2B] \times 1.22[\lambda/D_1]$ and $2.0[\lambda/2B] \times 2.44[\lambda/D_1]$ is shown in Figure 5.14. As expected, the maximum coupling

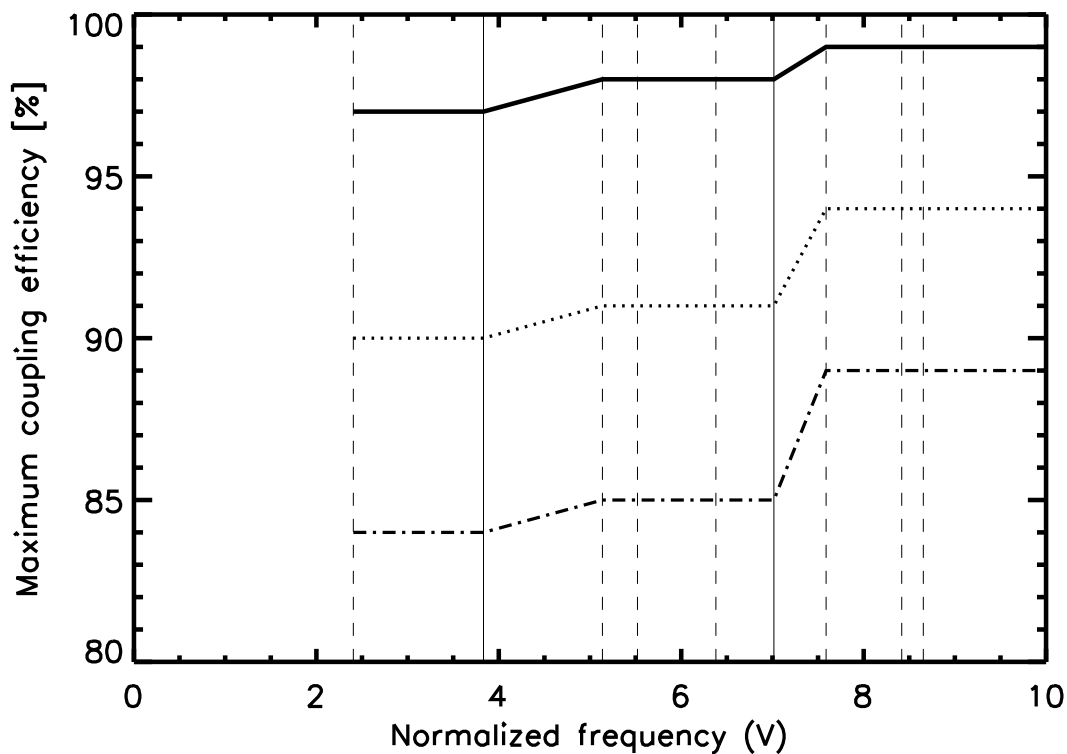


Figure 5.9: Maximum coupling efficiency versus normalized frequency for three different microlens sizes. Case study: Single dish pupil plane coupling. For a given normalized frequency, the maximum coupling efficiency is obtained at the optimal microlens focal ratio. The vertical dashed lines correspond to normalized frequencies of LP modes which do not couple light due to the symmetry of that mode (see Figure 5.6). The vertical solid lines correspond to normalized frequencies of LP modes which couple incoming light into the fiber (see Figure 5.6). The solid line stands for a microlens size of $2.44 \times 2.44[\lambda/D]$, the dotted line for a $1.22 \times 1.22[\lambda/D]$ microlens, and the dot-dashed line represents this relationship for a $0.61 \times 0.61[\lambda/D]$ microlens.

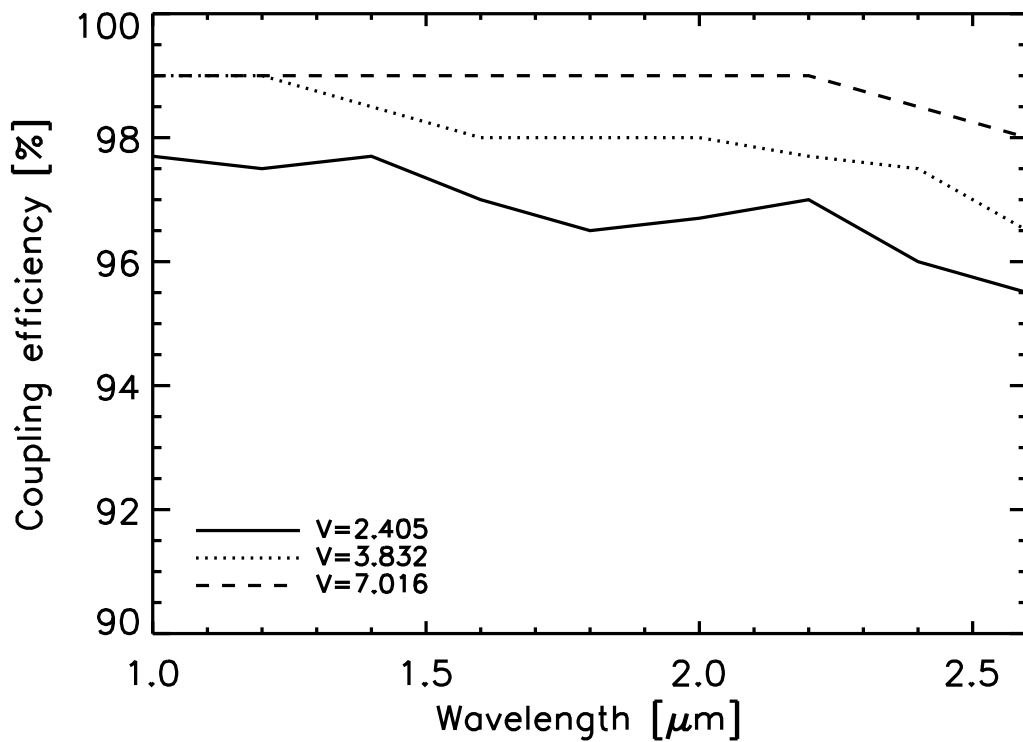


Figure 5.10: Coupling efficiency versus wavelength for a microlens size of $2.44 \times 2.44 [\lambda/D]$ and for $NA=0.17$ fibers having their cut-off frequencies at $2.2 \mu\text{m}$. Case study: Single dish pupil plane coupling. For each fiber, the focal ratio was fixed at the optimal value for $\lambda = 2.2 \mu\text{m}$. The studied wavelength interval covers the whole near-infrared range ($1 - 2.6 \mu\text{m}$). The solid line represents a single-mode fiber at $2.2 \mu\text{m}$, the dotted line a fiber with 4 transmitting modes at $2.2 \mu\text{m}$ and the dashed line a fiber with 9 modes at $2.2 \mu\text{m}$.

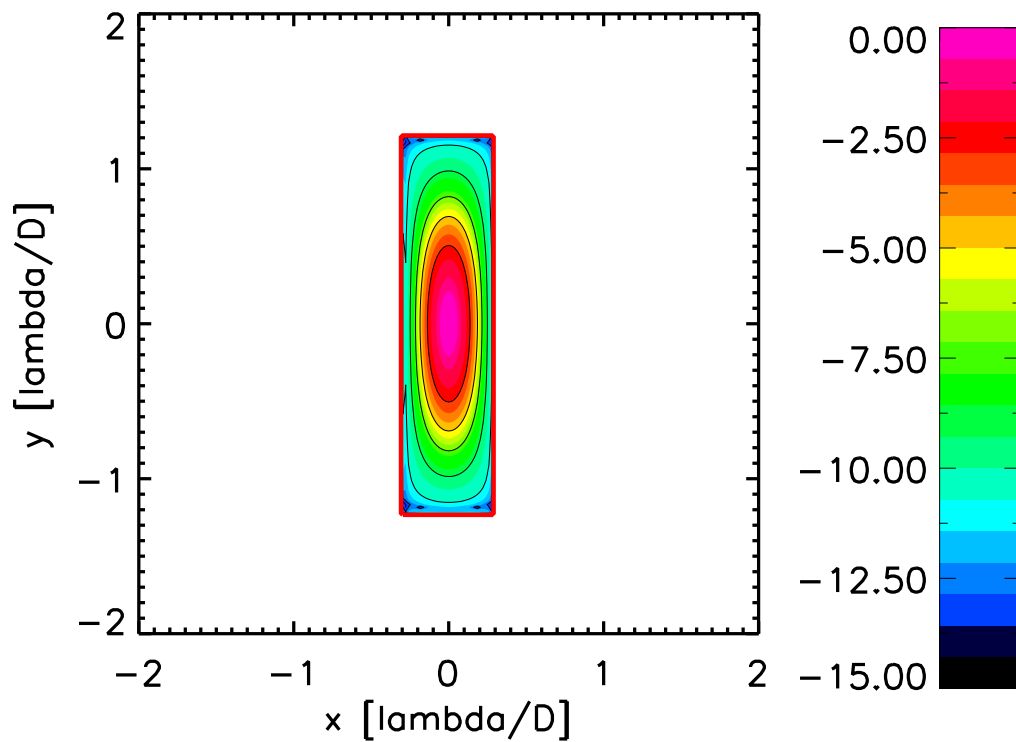


Figure 5.11: PSF of the LBT filtered by a rectangular microlens. The interferometric resolution direction corresponds to the x-axis, while the low resolution direction (one single dish) corresponds to the y-axis. The coordinates are given in multiples of $[\lambda/D]$, where λ is the wavelength and D is the Diameter of a single dish.

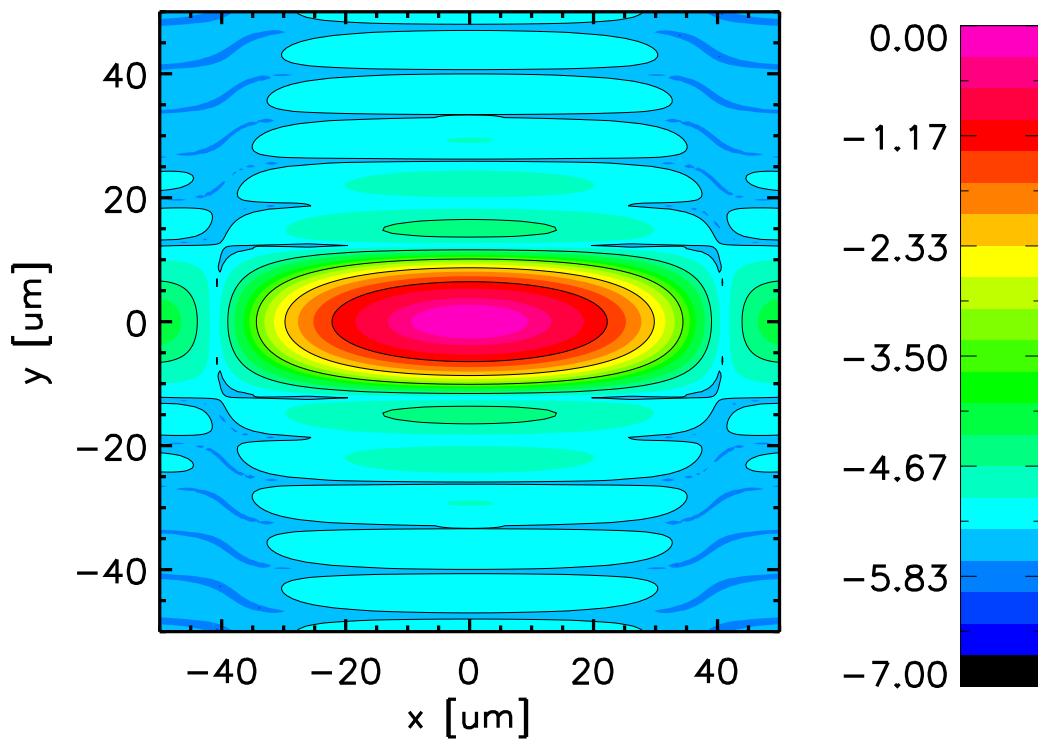


Figure 5.12: Micropupil obtained at the fiber's entrance from the filtered PSF shown in Figure 5.11. The size of the micropupil corresponds to that obtained at the optimal focal ratio which maximizes the coupling efficiency in a singlemode fiber of $10\mu\text{m}$ diameter. The coordinates are given in $[\mu\text{m}]$ in order to compare its size with the $10\mu\text{m}$ singlemode fiber considered in this paper.

efficiency increases with the normalized frequency. The total increment in the studied interval is from 63% to 90%. This behavior clearly suggests that few modes fiber improve considerably the coupling efficiency in a similar way as for the coupling in the focal plane. This increment can be elucidated by the physical explanation given in Section 5.3.2.2.

Finally, we studied the dependence of maximum coupling efficiency on wavelength. As it was done in Section 5.3.3.1, for each combination of spatial filter and fiber, the focal ratio was fixed at the optimal value for $\lambda = 2.2\mu\text{m}$. Then the wavelength was varied over the whole near-infrared ($1-2.6\mu\text{m}$). The results of these investigations are shown in Figure 5.15. This Figure shows maximum coupling efficiency as a function of wavelength for a microlens size of $2.0[\lambda/2B] \times 2.44[\lambda/D_1]$ for NA=0.17 fibers having their cut-off frequencies – 2.405 (single-mode), 3.832 (4 modes), 6.380 (7 modes) and 7.016 (9 modes) – at $2.2\mu\text{m}$. Only the $2.0[\lambda/2B] \times 2.44[\lambda/D_1]$ case is shown, but the results for the other two cases under study are analogous. The dependence of maximum coupling efficiency on wavelength exhibits a similar behavior as in the focal-plane coupling scenario and as such, it can be explained by the physical interpretation given in Section 5.3.2.2.

5.4 Implications for interferometric instruments at the LBT

5.4.1 The case of Anamorphic magnification

An alternative to coupling a double pupil to a conventional optical fiber is to modify the shape of the PSF so that it matches the symmetry of the fiber. This can be achieved by using anamorphic magnification. By means of an anamorphic magnifier, which can be an array of prisms or lenses (Gál et al. 2008), located between the pupil and focal planes of the telescope, it is possible to change the elliptical shape of the PSF to something with a circular morphology that probably will be easier to couple to optical fibers. As part of our investigations, we have simulated the coupling of an anamorphic double pupil to optical fibers. First, a magnification in the non-interferometric direction of ~ 3.5 was applied to the LBT configuration. By means of a χ^2 minimization between the electric field profile of the original double pupil in the high resolution direction and the electric field profile of the new anamorphic double pupil at the focal plane, this was found to be the optimal magnification factor. The new anamorphic double pupil is presented in the upper panel of Figure 5.16. The PSF of this anamorphic double pupil is shown in the lower panel of Figure 5.16. As can be seen in this Figure, the shape of the PSF is more roundish and has the same FWHM in all directions. This correspond approximately to the PSF of an equivalent 29 m telescope at $2.2\mu\text{m}$. We have found that the coupling of the electric field distribution of the anamorphic double pupil to single- and few-mode fibers located at the focal

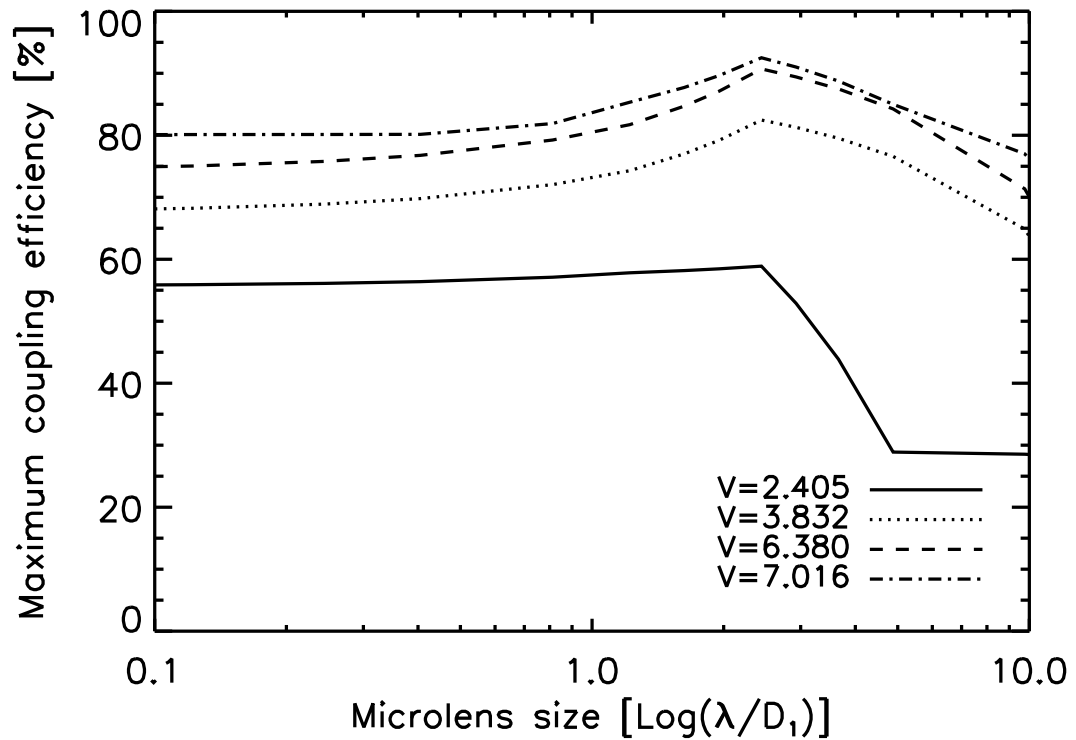


Figure 5.13: Maximum coupling efficiency versus microlens size for four different types of fibers. Case study: LBT pupil plane coupling. The microlens has a rectangular shape. Its size is given in units of $\text{Log}(\lambda/D_1)$ where λ is the wavelength and D_1 is the Diameter of a single dish. The microlens size in the Figure corresponds to L_1 or the size of the microlens in the low resolution direction. If the size-axis is changed to show L_2 (the microlens size in the high resolution direction), the current L_1 -axis must be divided by a factor of ~ 4.2 . The solid line represents a single-mode fiber, the dotted line a fiber with 4 transmitting modes, the dashed line a fiber with 7 transmitting modes and the dotted-dashed line a fiber with 9 modes.

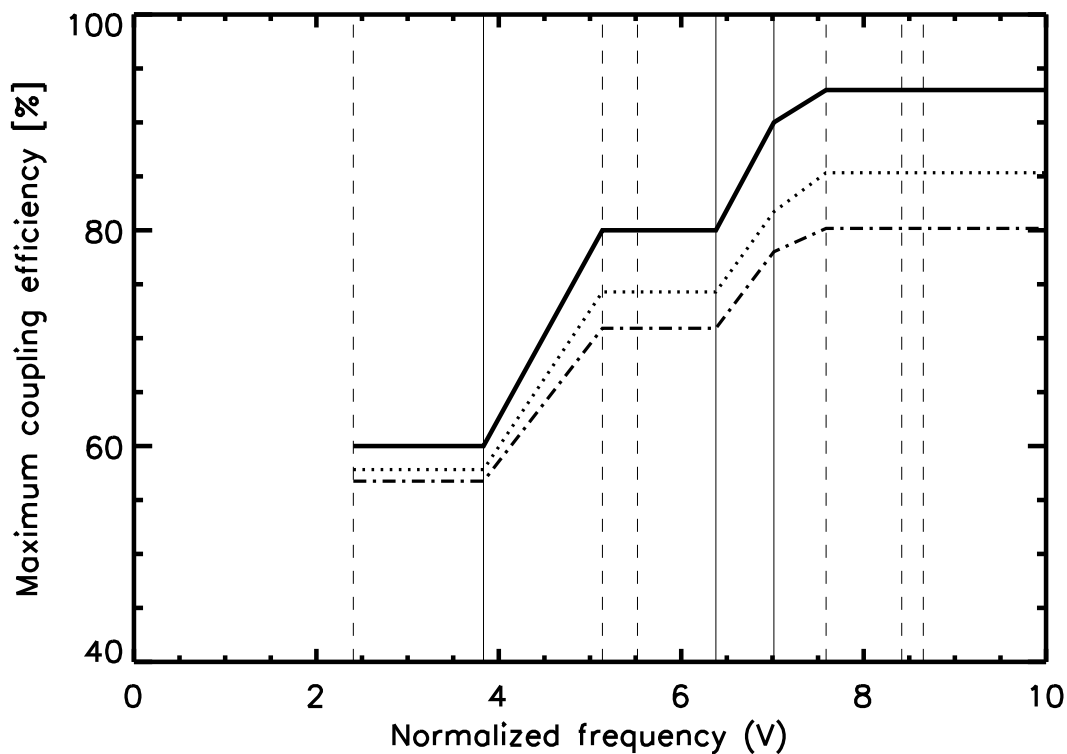


Figure 5.14: Maximum coupling efficiency versus normalized frequency for three different microlens sizes. Case study: LBT pupil plane coupling. For a given normalized frequency, the maximum coupling efficiency is obtained at the optimal microlens focal ratio. The vertical dashed lines correspond to normalized frequencies of LP modes which do not couple light due to the symmetry of that mode (see Figure 5.6). The vertical solid lines correspond to normalized frequencies of LP modes which couple incoming light into the fiber (see Figure 5.6). The solid line stands for a microlens size of $2.0[\lambda/2B] \times 2.44[\lambda/D_1]$, the dotted line for a $1.0[\lambda/2B] \times 1.22[\lambda/D_1]$ microlens, and the dot-dashed line represents this relationship for a $0.5[\lambda/2B] \times 0.61[\lambda/D_1]$ microlens.

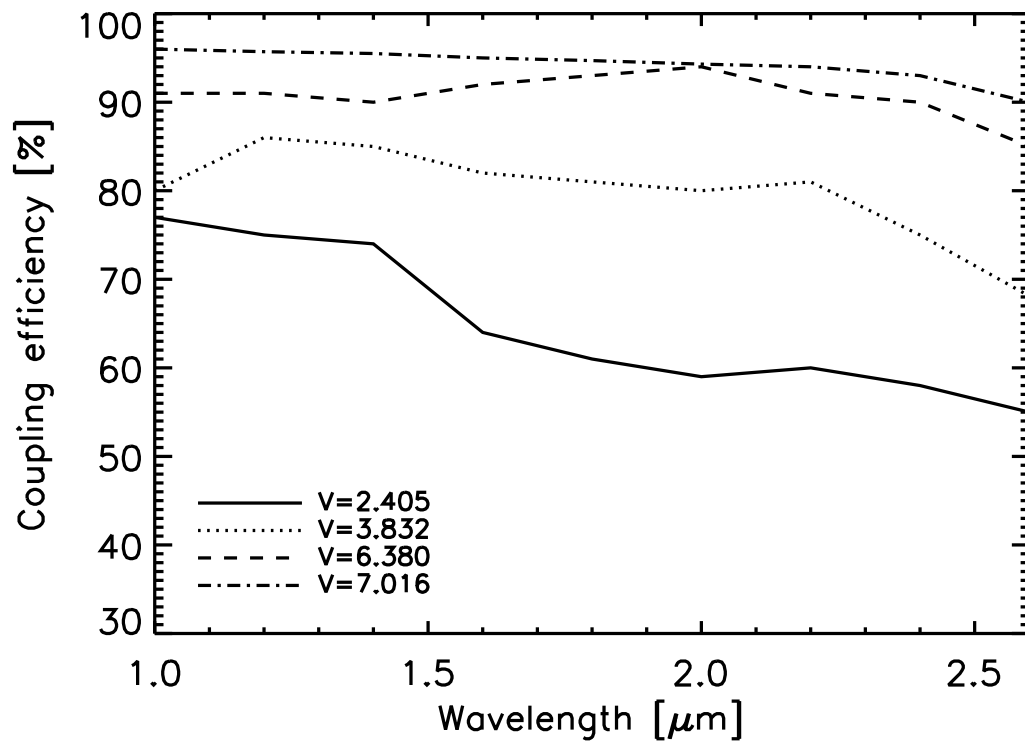


Figure 5.15: Coupling efficiency versus wavelength for a microlens size of $2.0[\lambda/2B] \times 2.44[\lambda/D_1]$ and for $NA=0.17$ fibers having their cut-off frequencies at $2.2 \mu\text{m}$. Case study: LBT pupil plane coupling. For each fiber, the focal ratio was fixed at the optimal value for $\lambda = 2.2 \mu\text{m}$. The studied wavelength interval covers the whole near-infrared range ($1 - 2.6 \mu\text{m}$). The solid line represents a single-mode fiber at $2.2 \mu\text{m}$, the dotted line a fiber with 4 transmitting modes at $2.2 \mu\text{m}$, the dashed line a fiber with 7 transmitting modes at $2.2 \mu\text{m}$ and the dotted-dashed line a fiber with 9 modes at $2.2 \mu\text{m}$.

plane of the telescope is almost equivalent to the coupling of a single dish to optical fibers studied in Section 5.3.2.1.

For the pupil-plane coupling, we have placed a square microlens in the focal plane of the telescope. The shape of the microlens was chosen based on the symmetry of the new PSF. At the focal plane of this microlens a symmetrical micropupil is formed. The micropupil in this case is shown in Figure 5.17. The size of the micropupil corresponds to that obtained at the optimal focal ratio which maximizes the coupling efficiency in a singlemode fiber of $10\mu\text{m}$ diameter. The coordinates are given in $[\mu\text{m}]$ in order to compare its size with the $10\mu\text{m}$ singlemode fiber considered in this paper. We found that the coupling of this micropupil to single- and few-mode fibers is almost equivalent to the single telescope case and therefore the results from Section 5.3.3.1 are applicable here as well.

The main optical implication of these results is that anamorphic magnification and sampling using rectangular microlenses are not equivalent. While the former really eliminates the elongated shape of the electric field's central peak at the focal plane and therefore produces a round micropupil, the sampling using rectangular microlenses preserves the difference in the two directions of the PSF and generates an elliptical micropupil.

5.4.2 The SERPIL/LIINUS spectrograph

The goal of the SERPIL/LIINUS project is to design an instrument that will expand the capabilities of the present interferometric camera LINC with imaging spectroscopy by means of an IFU located inside the LINC cryostat. The spectrometer could be then placed either inside LINC or in a new cryostat by transporting the light via optical fibers. Due to space constraints, in both cases the field sampling will be performed by a microlens array. The choice of the IFU for SERPIL/LIINUS is then either a TIGER-like lenslet IFU (Bacon et al. 1995) or a lenslet+fibers IFU (Le Fevre et al. 2000).

Notice that a fiber IFU in which the optical fibers are arranged in a close-packed bundle at the telescope focal plane could also be a possibility if fibers with ≥ 9 propagating modes are used (see Section 5.3.2.2) or if anamorphic magnification is performed (see Section 5.4.1). However, fiber IFUs suffer from low packing efficiency (generally less than 75% due to geometrical loss and cladding) and focal ratio degradation. This strongly constrains the designs of the spectrograph and the IFU itself. Adding lenses in front of the fibers helps to solve these two problems. Thus, for SERPIL/LIINUS only the lenslet+fibers approach is considered. Nevertheless, our analysis on the coupling of the electric field distribution of the LBT's double pupil to single- and few-mode fibers at the focal plane presented in Section 5.3.2.2 demonstrates that interferometric light can be successfully coupled to fewmode fibers without suffering from considerable losses. These results can then be used for other applications.

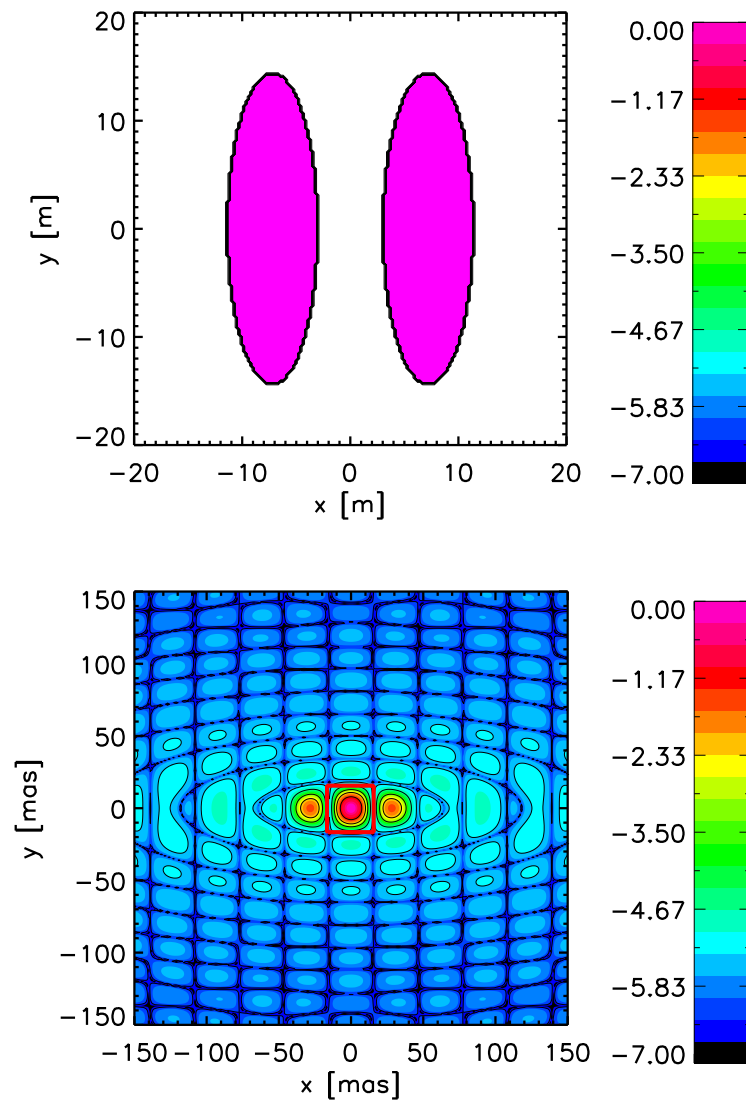


Figure 5.16: *Up:* Anamorphic double pupil. The coordinates are given in [m], *Down:* PSF of the Anamorphic double pupil. The coordinates are given in [mas]. This correspond approximately to the PSF of an equivalent 29 m telescope at $2.2 \mu\text{m}$.

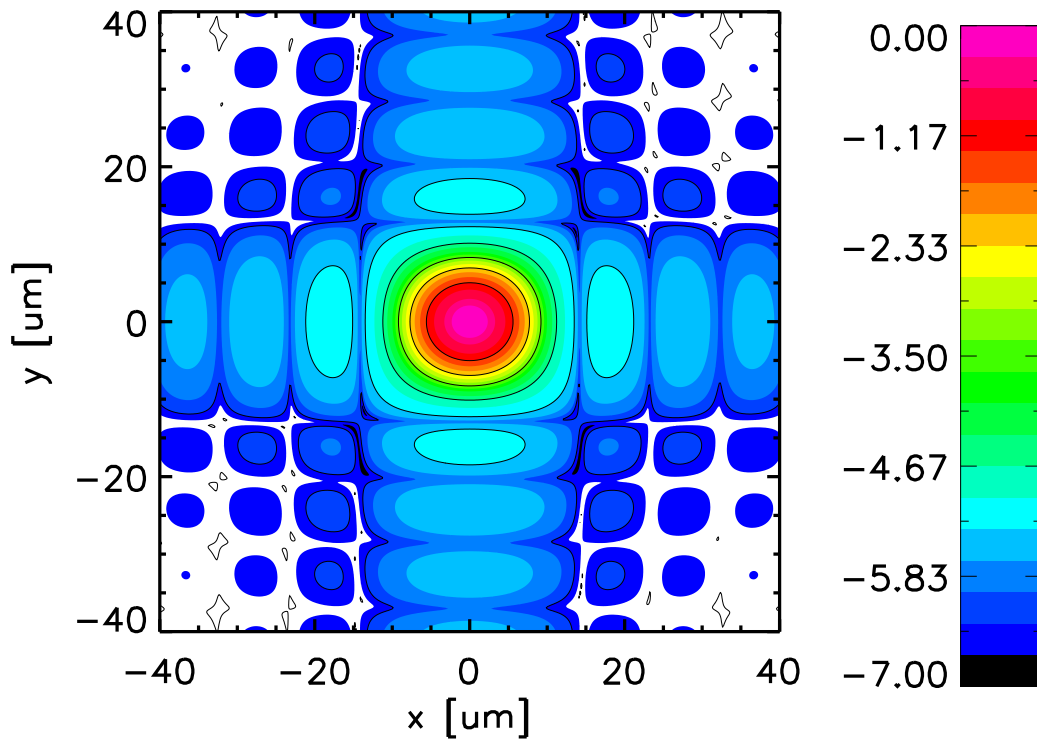


Figure 5.17: Micropupil obtained at the fiber's entrance from the PSF shown in the lower panel of Figure 5.16 filtered with a square microlens. The size of the micropupil corresponds to that obtained at the optimal focal ratio which maximizes the coupling efficiency in a singlemode fiber of $10\mu\text{m}$ diameter. The coordinates are given in $[\mu\text{m}]$ in order to compare its size with the $10\mu\text{m}$ singlemode fiber considered in this paper.

The TIGER-like lenslet approach depends strongly on the space available inside LINC cryostat. Our investigations suggest that it is feasible to build the spectrograph in the upper part of LINC (Gál et al. 2008). The space available as seen from the top of the cryostat is shown in Fig. 5.18. The crescent-moon (or Pac-man) shape offers the possibility to fold the light at some stage, translating in ~ 1.2 m length available for the spectrograph. In this approach, the microlens array has to be placed in the upper part of the cryostat as well. This implies that the LINC's focal plane has to be re-imaged at the position of the microlenses, translating in the creation of an optical path inside LINC that will bring the light from LINC's original focal plane at the bottom of the cryostat to the upper section. A preliminary design of this optical path together with the necessary optical elements is shown in Figure 5.19. The optics in the path perform in addition anamorphic magnification in case round micropupils are desired as input of the spectrograph. Currently, a very compact design of the spectrograph is being investigated in order to fit the entire instrument inside LINC and fulfill the top-level requirements defined by the science drivers (Gál et al. 2008).

In the lenslet+fibers approach, each micropupil is transported via optical fibers from the LINC hardware to a separate cryostat containing a conventional spectrograph. This implies that the fibers will work partially at ambient temperatures. This would alleviate space limitations for the spectrograph and therefore will give more flexibility in the design. In addition, few modifications to LINC are planned, a scenario that is desirable for many reasons. In this approach no optical path inside LINC is needed. A focal plane unit, consisting of the microlens array and the fiber bundle, and possibly an anamorphic magnifier, are the only elements of the whole integral field spectrograph that will be placed inside LINC. The light is picked from a reflecting mirror located at the filter wheel of the camera. The main problem to investigate in this approach is the physics of coupling a double pupil to optical fibers. The results presented in this paper helped to understand better this problem, and suggest that two options are feasible: Anamorphic magnification together with single- or few-mode fibers, and rectangular microlenses together with few-modes fibers (9 modes have $\sim 90\%$ coupling efficiency). Although anamorphic magnification offers high coupling efficiencies similar to those obtained for a single-dish, it also reduces the overall throughput due to additional active optical elements, and presents the difficulty of fitting the necessary optics into the confined space at LINC's focal plane. On the other hand, the sampling with rectangular microlenses gives worse coupling efficiencies if a fiber with < 7 propagation modes is used, but offers the advantage of reducing the number of optical elements and therefore improves the total throughput, reduces complexity and requires less space inside the LINC cryostat. Multi-mode fibers are not considered because they will add too much thermal background at ambient temperatures (see Section 5.4.3).

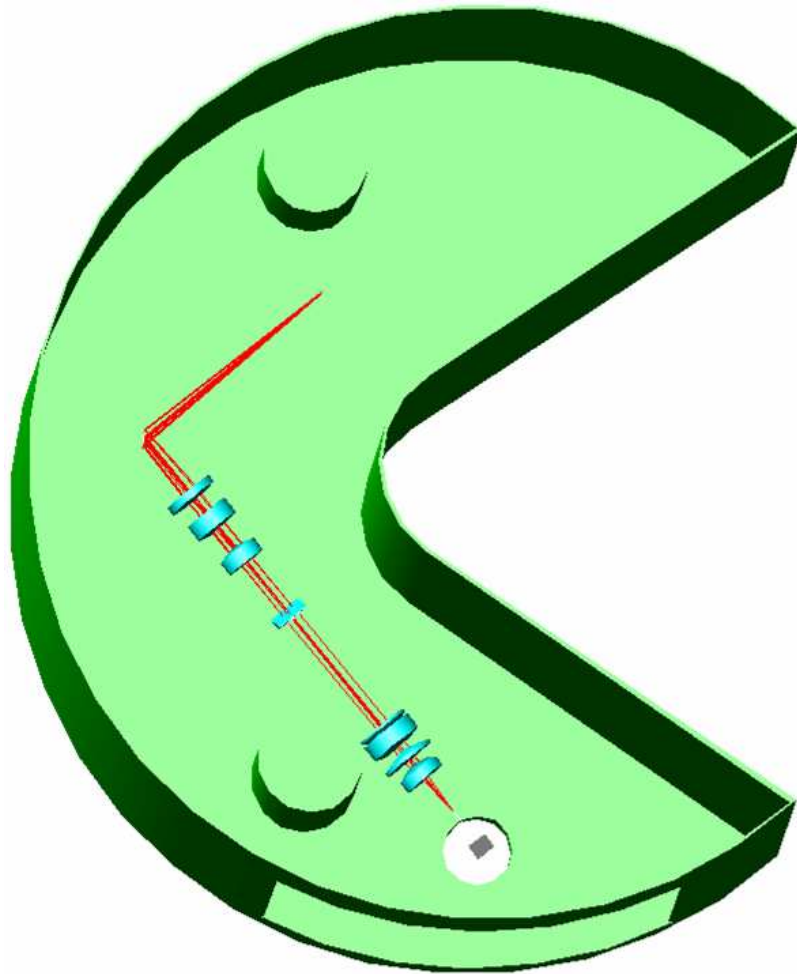


Figure 5.18: The space available inside LINC as seen from the top of the cryostat. The crescent-moon shape offers the possibility to fold the light to fit a spectrograph with a total optical track of ~ 1.2 m.

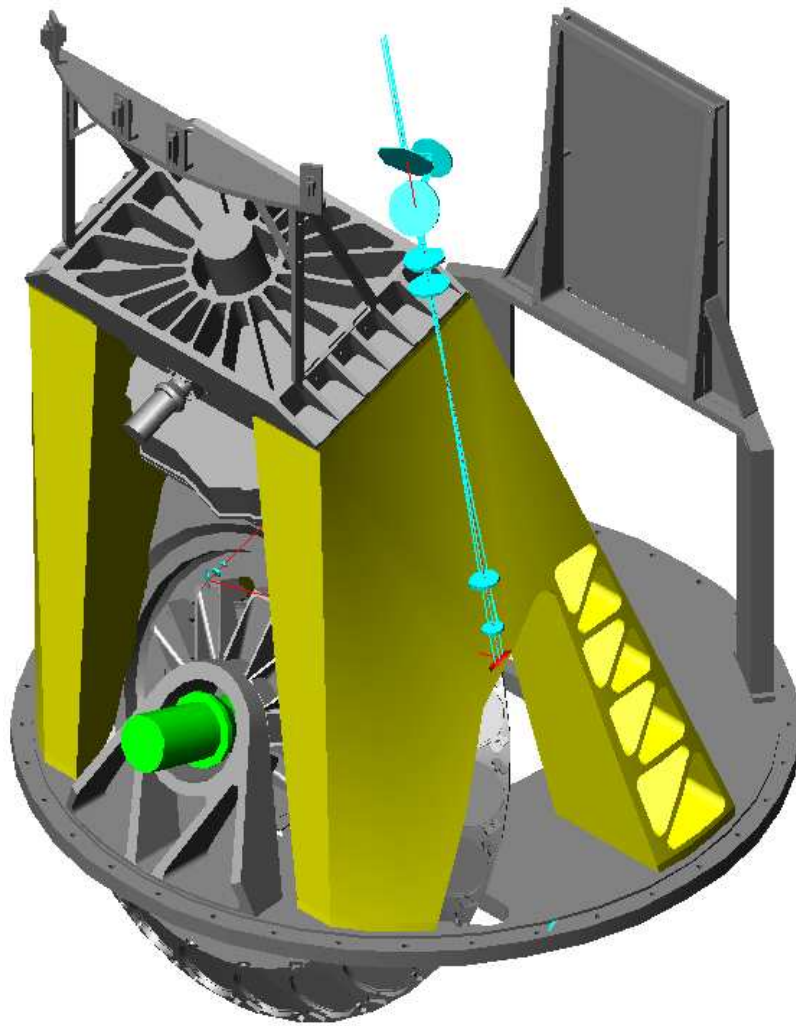


Figure 5.19: Required optical path to re-image LINC's focal plane at the upper part of the cryostat with preliminary optical design of the elements of the path including anamorphic magnification.

5.4.3 Background Noise considerations

An important issue to consider in the lenslet+fibers instrument concept presented in Figure 5.1 is the thermal background at near-infrared wavelengths and ambient temperatures. This radiation originates from the background produced by the LBT and the thermal emission from the fiber itself. The global optical transmission of the LBT in the K -band is $\sim 24\%$ (LINC FDR). This means that 76% of the light coming from the observed source is lost at the optical input of the interferometric instruments. This means, according to Kirchoffs law, that all optical elements in the optical path act as one grey body radiating with an estimated overall emissivity of $\epsilon_{LBT}=0.76$. Additionally, the fiber increases the background by thermal emission. Considering the fiber as a grey body with an emissivity given by $\epsilon_f=1-10^{-\alpha L/10}$, where α is the attenuation of the fiber in [dB/km] and L is the length of the fiber, one can estimate the fraction of additional background due to the fiber's thermal emission. At first, we found that the thermal emission from the fiber is proportional to the number of guided modes, that is: $P_f = B_{(\lambda,T)}\epsilon_f M \lambda^2$, where $B_{(\lambda,T)}$ is the black body equation, M is the number of modes and ϵ_f is the fiber emissivity. By assuming values of $\alpha=5$ [dB/km] (Ihle 2006) and $L=5$ [m], the fiber emissivity is $\epsilon_f=0.0052$. On the other hand, the LBT background is given by Planck's law multiplied by the emissivity of the telescope and the product $A\Omega$ which depends on the size of the microlenses. For a spatial sampling of $2.0[\lambda/2B] \times 2.44[\lambda/D_1]$ and a maximum number of guided modes of 9, we found that the fiber thermal emission is only $\sim 1.5\%$ of the total background radiation. For a Nyquist sampled instrument, this ratio is increased to $\sim 20\%$, becoming more significant. In order to minimize the overall background, one can reduce the number of guided modes in the fiber to e.g. 7. This will not have a considerable impact on the coupling efficiency, and will reduce the fiber thermal emission of a Nyquist sampled instrument to $\sim 15\%$.

Finally, as the expected observations with SERPIL/LIINUS will be limited to low power level light sources and small propagation lengths, only linear effects on fibers are realized. It is found that e.g. stimulated Brillouin scattering may initiate cross-talk in fibers at a power level above 4 mW at $1.5 \mu\text{m}$ and for fiber lengths >10 m. As both conditions are not met for SERPIL/LIINUS, nonlinear effects can be ignored.

5.5 Conclusions

The results presented in this paper helped to understand the physics of coupling light to optical fibers in several configurations. For the LBT, our results on diffraction-limited pupil-plane coupling have shown that single mode fibres do not couple well the interferometric micropupil of the LBT (60% coupling efficiency). Few mode fibres offer higher maximum coupling efficiency ($> 90\%$) and do not suffer much from background noise at ambient temperatures when the number of modes is lower than 10. Alternatively, anamorphic magnification before the microlenses can be used to

compensate for the large aspect ratio of the LBT pupil. This solution is almost equivalent to the coupling of a single telescope pupil to optical fibers.

Although anamorphic magnification and sampling using rectangular microlenses are not equivalent, the two options are feasible for an integral-field unit based on a microlens array inside LINC/NIRVANA. The two possibilities are: Anamorphic magnification together with square or hexagonal microlenses coupled to single- or few-mode fibers, and rectangular microlenses coupled to few-mode fibers with more than 3 propagating modes.

The coupling scenarios studied in this paper correspond to ideal cases. However, in a real astronomical observation, the coupling will be achieved most probable under non-ideal conditions. First, the incident wavefront may not be planar. Furthermore, optical power may be reflected back at the fiber's entrance (reflection loss). And principally, the fiber can be misaligned compared to the ideal position. All of these will decrease the coupling efficiency in different amounts. We have undertaken a research program to investigate the coupling under non-ideal conditions. The results will be presented in a subsequent publication (Müller Sánchez et al. 2008d), which will contain not only theoretical results from simulations but also real measurements from a laboratory experiment.

Chapter 6

Conclusions and Outlook

The work documented in this thesis consisted of developing key technologies for integral-field spectroscopy (SERPIL/LIINUS) in Fizeau interferometric mode at the LBT, and examining datacubes from an existing integral-field spectrograph (SINFONI) to elucidate the astrophysics of nearby AGN.

In the observational part, the aim of this thesis has been to reveal the nature of the nuclear star formation and the molecular gas in a selected number of nearby AGN. Emphasis was given to the Circinus galaxy and NGC1068, the two most prominent and brightest Seyfert 2 galaxies. Our extensive analysis have allowed us to obtain important scientific results in the field of modern AGN research which can be summarized as follows:

The Circinus galaxy

- The stellar component on scales of a few parsecs from the nucleus has been resolved. Vigorous and recent star formation has been found. The bolometric luminosity of the stars at these scales accounts for $\sim 1.4\%$ of the bolometric luminosity of the entire galaxy. The age of the starburst is ~ 80 Myr for a starformation timescale of 100 Myr. The observed clumpy morphology of the stars is explained by hundreds of young stellar clusters of average mass of $1 \times 10^{3-4} M_{\odot}$. No stellar kinematics could be extracted from the datacube.
- The molecular gas surrounding the nucleus has been resolved as well. The morphology and kinematics of the gas are consistent with those of a rotating opaque thick disk, which we associate with the molecular/dusty torus. Since the scales on which the gas and stars exist are similar, this torus must be forming stars, and due to the limits on extinction to the stars, it must be a clumpy medium rather than an uniform structure.
- An extensive study of the coronal lines showed that they are composite: one narrow component associated to the AGN and a broad component, which is

flowing out from the nucleus and which is most probably excited by shocks.

NGC1068

- The distribution of the molecular gas traced by the H₂ 1–0S(1) emission in the central 0.8'' × 0.8'' of the galaxy has been resolved. The flux map of molecular hydrogen emission reveals two prominent linear structures leading to the AGN from the north and south: one lying right in front of the nucleus (the core) and another one 0.35'' north of the center (the tongue). The tongue correlates with the mid-IR emission and its tip coincides with a knot of radio continuum emission providing direct evidence of the shock interface between the jet and a molecular cloud that has caused the jet direction to change.
- Dynamical modeling shows that the gas in these features is streaming towards the nucleus. The infalling gas is contained on highly elliptical/parabolic orbits whose orientation is consistent with that of the plane of the galaxy. We interpret this as strong evidence of how gas, on scales of a few parsecs, is fueling the AGN.
- The gas transport is from ~ 70 pc to a few parsec from the nucleus in the plane of the galaxy. The modeling reveals the existence of two streamers: a northern streamer associated with the tongue that passes very close to the nucleus (pericenter of 5 pc), and a southern streamer which lies currently in front of the nucleus associated with the core, and has a pericenter of ~ 1 pc.
- The dM/dt is ~ 15 M_⊙ yr⁻¹ from scales of 30 pc to a few pc. This is about 1000 times that from a few pc to a few R_S, a ratio similar to that observed in the Galactic Center. This may be a natural consequence of inefficient angular momentum transport.
- The geometry, kinematics and high column density of the core can be explained by a central component consisting of a set of infalling clouds that form the optically thick outerpart of an amorphous clumpy molecular/dusty structure.

This was the first time that such a detailed analysis of an AGN using data from optical/infrared integral-field spectroscopy has been performed.

On the instrumental part of the thesis, the work presented here helped to understand the physics of coupling light to optical fibers in several configurations. This is crucial for the design of an interferometric integral-field spectrograph at the LBT based on a lenslet+fibers integral-field unit. For a double-pupil configuration such as the LBT, our results on diffraction-limited pupil-plane coupling are the following:

- Single mode fibers do not couple well the interferometric micropupil of the LBT (60% coupling efficiency).

- Few-mode fibers offer higher maximum coupling efficiency ($> 90\%$) and do not suffer much from thermal background at ambient temperatures when the number of modes is lower than 10.
- Anamorphic magnification eliminates the elongation of the interferometric electric field pattern and produces round micropupils. This solution is almost equivalent to the coupling of a single telescope pupil to optical fibers.
- Two options are viable for a lenslet+fibers integral-field unit at the LBT: Anamorphic magnification together with square or hexagonal microlenses coupled to single- or few-mode fibers, and rectangular microlenses coupled to few-mode fibers with more than 3 propagating modes.

The status and future prospects of this project have already been discussed in Section 4.5.3.

6.1 Outlook

The investigation of AGN using high resolution integral field spectroscopy is a very new topic in astronomy. The first results (part of them presented in this thesis) have shown that this is a very powerful observational technique to probe the distribution and kinematics of the nuclear matter in AGN on scales of a few parsec. In order to continue elucidating the physical properties of nearby AGN, further analysis of the existing SINFONI data and new observations have to continue:

1. Further analysis of the existing and new data: The immediate task is to continue the analysis of the data which is already available. The data for several targets listed in Table 1.1 have not yet been fully analysed. The results of this analysis will not only add new insights to the current interpretations, but also provide the ground to plan further, more detailed studies of the most interesting objects. Additionally, new targets are being observed with SINFONI at the time of writing this thesis. Recent data of Arp220 and NGC6240 have to be reduced and then analysed.
2. Use of other observational techniques and facilities: Millimeter interferometry has been a very successful technique to analyse the distribution of cold molecular gas. Data from such interferometers would be complementary to the SINFONI data and would help to better constrain the distribution and dynamical models of the gas. For instance, for NGC1068, tracing the cold molecular gas across the central arcsec would confirm the existence of gas streaming motions along the linear feature leading directly to the AGN.

3. Comparison to simulations and models: The determination of the M_{BH} from spatially resolved stellar dynamics has been a difficult and long process. This is mainly due to the difficult extraction of the stellar kinematics in some of the data, translating in problems for the models to constrain the black hole mass. The modelling of the stellar dynamics of more objects of the sample, not only NGC3227 and NGC1068, has to be done. In addition, in order to fully understand the assembly of AGN and the processes involved in their functioning, radiative transfer modelling has to be used in conjunction with the observations. Such models are especially important for the interpretation of the molecular gas distribution. The comparison of our molecular gas data to the models has only just begun (see Section 3.3) and must be continued.
4. Enlargement of the source sample: as was already pointed out in Section 1.4, a larger sample of objects has to be studied in order to draw more general conclusions on the physics of Nearby AGN. Many sources are still in reach of the actual adaptive-optics correction of SINFONI. In addition, the Nearby AGN program with SINFONI will benefit from the Laser Guide Star Facility (LGSF) already on operation at the VLT. This will allow the creation of a sample based on scientific objectives rather than technical constraints. Among the new and interesting science that could be done with the LGSF are:
 - Nearby Spiral galaxies: Emphasis this time is given to the stellar kinematics to measure the black hole masses in very nearby spiral galaxies, and hence to probe the low-mass end of the $M_{BH} - \sigma_*$ relation. Such measurements, which would show whether the relation remains valid for bulges and pseudo-bulges, or how it changes, are a crucial step in understanding how secular evolution and merging of galaxies influence black hole growth.
 - Nuclear stellar disks in Seyfert and spiral galaxies: Recent results from Davies et al. 2007 show that on scales of a few parsec from the nucleus, drops in stellar velocity dispersion are seen in some Seyfert galaxies (NGC1097 and NGC1068). By mapping the distribution and kinematics at high S/N of the stars as well as the molecular and ionized gas in a larger sample of objects which are putative candidates of showing this drops, it will be possible to test theories of the origin of this phenomenon and its impact on fuelling nuclear activity and black hole growth.
 - Low luminosity AGN: These objects are taking more and more attention in the field of AGN astronomy, not only because of the physical properties of their central black hole and their position at the $M_{BH} - \sigma_*$ relation, but also because of the new predictions from theoretical torus models which suggest that the putative torus in AGN vanishes in this type of objects regardless of their classification as Type 1 or Type 2. Integral field spectroscopic observations with the LGSF will allow to probe the existence of molecular gas surrounding the nucleus, and test current theoretical models.

All of this suggests that the study of AGN using near-infrared integral-field spectroscopy has a very promising future, especially if the AGN are observed with an instrument such as SERPIL/LIINUS which will provide three times better spatial resolution compared with current 8-10m facilities. In fact, the study of Nearby AGN is the main scientific motivation for building this instrument. Therefore the future work mentioned above could eventually not only be done using SINFONI at the VLT but also SERPIL/LIINUS at the LBT.

Bibliography

- Abuter, R., Schreiber, J., Eisenhauer, F., Ott, T., Horrobin, M., & Gillesen, S. 2005, *New Astronomy Reviews*, 50, 398
- Allington-Smith, J., Murray, G., Content, R., Dodsworth, G., Davies, R., Miller, B. W., Turner, J., Jorgensen, I., Hook, I., Crampton, D., et al. 2002, *ASPC*, 282, 415
- Alloin, D., Galliano, E., Cuby, J. G., Marco, O., Rouan, D., Clénet, Y., Granato, G. L., & Franceschini, A. 2001, *A&A*, 369, L33
- Antonucci, R. R. J., & Miller, J. S. 1985, *ApJ*, 297, 621
- Antonucci, R. R. J. 1993, *Ann. Rev. Astron. Astrophys.*, 31, 473
- Arribas, S., Mediavilla, E., & Rasilla, J. L. 1991, *ApJ*, 369, 260
- Asari, N., Garcia-Rissmann, A., González Delgado, R., Storchi-Bergmann, T., & Cid Fernandes, R. 2007 in *Galaxy Evolution Accross the Hubble Time*, eds. Combes F., Palous J., IAU Symposium, 235, 71
- Bacon, R., Adam, G., Baranne, A., Courtes, G., Dubet, D., Dubois, J. P., Emsellem, E., Ferruit, P., Georgelin, Y., Monnet, G., et al. 1995, *A&AS*, 113, 347
- Bacon, R., Copin, Y., Monnet, G., Miller, B. W., Allington-Smith, J. R., Bureau, M., Carollo, C. M., Davies, R. L., Emsellem, E., Kuntschner, H., et al. 2001, *MNRAS*, 326, 23
- Baker, A. 2000, Ph.D. thesis, Caltech
- Bannikova, E.Yu., & Kontorovich, V.M. 2007, *ARep*, 51, 264
- Bassani, L., Dadina, M., Maiolino, R., Salvati, M., Risaliti, G., della Ceca, R., Matt, G., & Zamorani, G. 1999, *ApJS*, 121, 473
- Bender, R., Kormendy, J., Bower, G., Green, R., Thomas, J., Danks, A. C., Gull, T., Hutchings, J. B., Joseph, C. L., Kaiser, M. E., et al. 2005, *ApJ*, 631, 280

- Bender, R., Burstein, D., & Faber, S. M. 1992, ApJ, 399, 462
- Bland-Hawthorn, J., Gallimore, J., Tacconi, L., Brinks, E., Baum, S. A., Antonucci, R. R. J., & Cecil, G. N. 1997, Ap&SS, 248, 9
- Blietz, M., Cameron, M., Drapatz, S., Genzel, R., Krabbe, A., van der Werf, P.V.D., Sternberg, A., & Ward, M. 1994, ApJ, 421, 92
- Bock, J. J., et al. 2000, AJ, 120, 2904
- Bonnet, H., Ströbele, S., Biancat-Marchet, F., Brynnel, J., Conzelmann, R. D., Delabre, B., Donaldson, R., Farinato, J., Fedrigo, E., Hubin, N. N., et al. 2003, in *Adaptive Optical System Technologies II*, eds. Wizinowich P., Bonaccini D., Proc. SPIE, 4839, 329
- Bonnet, H., Abuter, R., Baker, A., Bornemann, W., Brown, A., Castillo, R., Conzelmann, R., Damster, R., Davies, R., Delabre, B., et al. 2004, in *The ESO Messenger*, 117, 17
- Born, M., & Wolf, E. 1959, "Principles of Optics - Electromagnetic Theory of Propagation, Interference and Diffraction of Light", Pergamon Press, New York
- Bryant, P. M., Scoville, N. Z. 1999, ApJ, 117, 2632
- Cameron, M., Storey, J. W. V., Rotaciuc, V., Genzel, R., Verstraete, L., Drapatz, S., Siebenmorgen, R., & Lee, T. J. 1993, ApJ, 419, 136
- Cappellari, M., & Copin, Y. 2003, MNRAS, 342, 345
- Cecil, G., Dopita, M. A., Groves, B., Wilson, A. S., Ferruit, P., Pcontal, E., & Binette, L. 2002, ApJ, 568, 627
- Charbonneau, D. 2005, ApJ, 626, 523
- Cid Fernandes, R., Gu, Q., Melnick, J., Terlevich, E., Terlevich, R., Kunth, D., Rodrigues Lacerda, R., & Joquet B. 2004, MNRAS, 355, 273
- Condon, J. J. 1992, ARAA, 30, 575
- Content, R. 1997, in *Optical Telescopes of Today and Tomorrow*, eds. Ardeberg A. L., Proc. SPIE., 2871, 1295
- Contini, M., & Contini, T. 2003, MNRAS, 342, 299
- Coudé du Foresto, V., Perrin, G., Ruilier, C., Mennesson, B. P., Traub, W. A., & Lacasse, M. G. 1998, in *Astronomical Interferometry*, eds. Reasenberg R. D. , Proc. SPIE, 3350, 856

- Coudé du Foresto, V., Faucherre, M., Hubin, N., & Gitton, P. 2000, *A&AS*, 145, 305
- Cuadra, J., Nayakshin, S., Springel, V., & di Matteo, T. 2006, *MNRAS*, 366, 358
- Dale, D., Sheth, K., Helou, G., Regan, M., & Hüttemeister, S. 2005, *AJ*, 129, 2197
- Dakin, J. P., & Kahn, D. A. 1977, *Optical and Quantum Electronics Letters*, 9, 540
- Das, V., Crenshaw, D.M., Kraemer, S.B., & Deo, R.P. 2006, *ApJ*, 132, 620
- Davies, R., Forbes, D. A., Ryder, S., Ashley, M. C. B., Burton, M., Storey, J. W. V., Allen, L. E., Ward, M. J., & Norris, R. P. 1998, *MNRAS*, 293, 189
- Davies, R., Sternberg, A., Lehnert, M., & Tacconi-Garman, L. 2003, *ApJ*, 597, 907
- Davies, R., Tacconi, L., & Genzel, R. 2004a, *ApJ*, 602, 148
- Davies, R., Tacconi, L., & Genzel, R. 2004b, *ApJ*, 613, 781
- Davies, R., Tacconi, L., Genzel, R., Ott, T., & Rabien, S. 2004, in *Advancements in Adaptive Optics*, eds Bonnacini D., Ellerbroek B., Raggazoni R., Proc. SPIE, 5490, 473
- Davies, R. L., Thomas, J., Genzel R., Müller Sánchez, F., Tacconi, L., Sternberg, A., Eisenhauer, F., Abuter, R., Saglia, R., & Bender, R. 2006, *ApJ*, 646, 754
- Davies, R., Genzel, R., Tacconi, L., Müller Sánchez, F., & Sternberg, A. 2006, in *Mapping the Galaxy and Nearby Galaxies*, eds. Wada K., Combes F., arXiv:0610.203
- Davies, R., Müller Sánchez, F., Genzel, R., Tacconi, L.J., Hicks, E., Friedrich, S., & Sternberg, A. 2007, *ApJ*, 671, 1388
- Deming, D., & Seager, S., 2005, *Nature*, 434, 740
- Dopita, M. A., & Sutherland, R. S. 1995, *ApJ*, 455, 468
- Draine, B. 2003, *ARA&A*, 41, 241
- Eardley, D. M., & Press, W. H. 1975, *ARA&A*, 13, 381
- Efstathiou, A., & Rowan-Robinson, M. 1995, *MNRAS*, 273, 649
- Eisenhauer, F., Tecza, M., Thatte, N., Genzel, R., Abuter, R., Iserlohe, C., Schreiber, J., Huber, S., Roehrlé, C., Horrobin, M., et al. 2003a, in *The ESO Messenger*, 113, 17

- Eisenhauer, F., Abuter, R., Bickert, K., Biancat-Marchet, F., Bonnet, H., Brynnel, J., Conzelmann, R. D., Delabre, B., Donaldson, R., Farinato, J., et al. 2003b, in *Instrument Design and Performance for Optical/Infrared Ground-based Telescopes*, eds Iye M., Moorwood A., Proc. SPIE, 4841, 1548
- Eisenhauer, F., Genzel, R., Alexander, T., Abuter, R., Paumard, T., Ott, T., Gilbert, A., Gillessen, S., Horrobin, M., Trippe, S., et al. 2005, *ApJ*, 628, 246
- Ferland, G.J., & Netzer, H. 1983, *ApJ*, 264, 105
- Ferrarese, L., & Merritt, D. 2000, *ApJ*, 539, L9
- Ferrarese, L., & Ford, H. 2005, *SSRv*, 116, 523
- Fizeau, H., 1868, "Prix bordin: Rapport sur le concours de l'année 1867", *C.R.Acad.Sci.*, 66, 932
- Freeman, K. C., Karlsson, B., Lyngå, G., Burrell, J. F., van Woerden, H., Goss, W. M., & Mebold, U. 1977, *A&A*, 55, 445
- Fritz, J., Franceschini A., & Hatziminiaoglou, E. 2006, *MNRAS*, 366, 767
- Gál, C., Müller Sánchez, F., Krabbe, A., Eisenhauer, F., Iserlohe, C., Haug, M., & Herbst, T. M. 2006, in *Ground-based and Airborne Instrumentation for Astronomy*, eds McLean I. S., Iye M., Proc. SPIE, 6269, 62693
- Gál, C., et al. 2008, in prep.
- Galliano, E., & Alloin, D. 2002, *A&A*, 393, 43
- Galliano, E., Alloin, D., Granato, G. L., & Villar-Martín, M. 2003, *A&A*, 412, 615
- Galliano, E., Pantin, E., Alloin, D., & Lagage, P. O. 2005, *MNRAS*, 363, L1
- Gallimore, J. F., Baum, S. A., & O'Dea, C. P. 1996, *ApJ*, 464, 198
- Gallimore, J. F., Baum, S. A., & O'Dea, C. P. 2004, *ApJ*, 613, 794
- Gao, Y., Solomon, P. M. 2004, *ApJ*, 606, 271
- Gebhardt, K., Richstone, D., Kormendy, J., Lauer, T. R., Ajhar, E. A., Bender, R., Dressler, A., Faber, S. M., Grillmair, C., Magorrian, J., et al. 2000a, *AJ*, 119, 1157
- Gebhardt, K., Bender, R., Bower, G., Dressler, A., Faber, S. M., Filippenko, A. V., Green, R., Grillmair, C., Ho, L. C., Kormendy, J., et al. 2000b, *ApJ*, 539, L13
- Genzel, R., & Townes, C. H. 1987, *ARA&A*, 25, 377

- Genzel, R., Schödel, R., Ott, T., Eisenhauer, F., Hofmann, R., Lehnert, M., Eckart, A., Alexander, T., Sternberg, A., Lenzen, R., et al. 2003, *ApJ*, 594, 812
- Gloge, D. 1971, "Weakly guiding fibers", *Applied Optics*, 10, 2252
- Goldader, J. D., Joseph, R. D., Doyon, R., & Sanders, D. B. 1997, *ApJs*, 108, 449
- González Delgado, R. M., Heckman, T., & Leitherer, C. 2001, *ApJ*, 546, 845
- González Delgado, R. M., & Cid Fernandes, R. 2005, in *Starbursts: from 30 Doradus to Lyman Break Galaxies*, eds. de Grjs R., González Delgado R., (Dordrecht: Springer), *ASSL*, 329, 263
- Granato, G. L., & Danese, L. 1994, *MNRAS*, 268, 235
- Gratadour, D., Rouan, D., Boccaletti, A., Riaud, P., & Clénet, Y. 2005, *A&A*, 429, 433
- Gratadour, D., Rouan, D., Mugnier, L. M., Fusco, T., Clénet, Y., Gendron, E., & Lacombe, F. 2006, *A&A*, 446, 813
- Greenhill, L. J., Gwinn, C. R., Antonucci, R., & Barvainis, R. 1996, *ApJ*, 472, L21
- Greenhill, L. J., Booth, R. S., Ellingsen, S. P., Herrnstein, J. R., Jauncey, D. L., McCulloch, P. M., Moran, J. M., Norris, R. P., Reynolds, J. E., & Tzioumis, A. K. 2003, *ApJ*, 590, 162
- Gu, Q., Dultzin-Hacyan, D., & de Diego, J. 2001, *RMxAA*, 37, 3
- Heckman, T., González Delgado, R., Leitherer, C., Meurer, G., Krolik, J., Wilson, A., Koratkar, A., & Kinney, A. 1997, *ApJ*, 482, 114
- Hatziminaoglou, E., Fritz, J., Perez-Fournon, I., Franceschini, A., Hernan-Caballero, A., Afonso-Luis, A., Lonsdale, C., Fang, F., Oliver, S., Rowan-Robinson, M., et al. 2006, in *Infrared Diagnostics of Galaxy Evolution*, ASP conference, arXiv:0603.359
- Hege, E. K., Angel, J. R. P., Cheselka, M., & Lloyd-Hard, M. 2001, in *Advanced Imaging Technologies and Commercial Applications*, eds. Natalie Clark, John D. Gonglewski, *Proc. SPIE*, 2566B, 144
- Herbst, T. M., Rix, H. W., Bizenberger, P., & Ollivier, M. 2000, in *Interferometry in Optical Astronomy*, eds. Pierre J. Lena, Andreas, Quirrenbach, *Proc. SPIE*, 4006, 673
- Herbst, T. M. 2003, *Ap&SS*, 286, 45

- Herbst, T. M., Ragazzoni, R., Eckart, A., & Weigelt, G. 2004, in *Ground-based Instrumentation for Astronomy*, eds. Moorwood A. F., Masanori I., Proc. SPIE, 5492, 1045
- Hicks, E. K. S., et al. 2008, in prep.
- Hill, J. M. 1994, in *Amplitude and Intensity Spatial Interferometry II*, eds. James B. Breckinridge, Proc. SPIE, 2200, 248
- Hill, J. M. & Salinari, P. 2002, in *Large Ground-based Telescopes*, eds. Oschmann, Jacobus M., Stepp Larry M., Proc. SPIE, 4837, 15
- Hinz, P. M., Angel, J. R. P., McCarthy, D. W. Jr., Hoffman, W. F., & Peng, C. Y. 2003, in *Interferometry for Optical Astronomy II*, eds. Wesley A. Traub, Proc. SPIE, 4838, 108
- Hodapp, K. W., et al. 2004, ASSL, 300, 501
- Hönig, S., Beckert, T., Ohnaka, K., & Weigelt, G. 2006, A&A, 452, 459
- Horton, A. J., & Bland-Hawthorn, J. 2006, in *Ground-based and Airborne Instrumentation for Astronomy*, eds. McLean Ian S., Masanori I., Proc. SPIE, 6269, 62691K
- Howarth, I. D. 1983, MNRAS, 203, 301
- Ihle, S. 2006, "Implementation of a fiber-coupler for astronomical interferometry and its thermal analysis", Diplomarbeit TU München
- Jaffe, W., Meisenheimer, K., Röttgering, H. J. A., Leinert, Ch., Richichi, A., Chesneau, O., Fraix-Burnet, D., Glazenberg-Kluttig, A., Granato, G.-L., Graser, U., et al. 2004, Nature, 429, 47
- Jaffe, W., Raban, D., Röttgering, H., Meisenheimer, K., & Tristram, K. 2007, ASPC, 373, 439
- Kaspi, S., Smith, P., Netzer, H., Maoz, D., Jannuzi, B., & Giveon, U. 2000, ApJ, 533, 631
- Kaspi, S., Maoz, D., Netzer, H., Peterson, B., Vestergaard, M., & Jannuzi, B. 2005, ApJ, 629, 61
- Kenworthy, M., Parry, I., & Taylor, K. 1998, Proc. Soc. Photo-Opt. Instrum. Eng., 3354, 419
- Kenworthy, M., Parry, I., & Taylor, K. 2001, PASP, 113, 215
- Khachikian, E. Y., & Weedman, D. W. 1974, ApJ, 192, 581

- Knapen, J. 2004, in *Penetrating bars through masks of cosmic dust: The Hubble tuning fork strikes a new note*, eds Block D., Puerari I., Freeman K., Groess R., Block E. (Dordrecht: Kluwer Academic Publishers), ASSL, 319, 189
- Kormendy, J., & Richstone, D. 1995, *ARA&A*, 33, 581
- Kormendy, J., & Gebhardt, K. 2001, in *Proc of 20th Texas Symposium on Relativistic Astrophysics*, eds. H. Martel & J. Wheeler, AIP, 586, 363.
- Koski, A. T. 1978, *ApJ*, 223, 56
- Larkin, J. E., Quirrenbach, A., Krabbe, A., Aliado, T., Barczys, M., Brims, G., Canfield, J., Gasaway, T. M., LaFreniere, D., Magnone, N., et al. 2003, in *Instrument Design and Performance for Optical/Infrared Ground-based Telescopes*, eds. Masanori I., Moorwood A. F. M., Proc. SPIE, 4841, 1600
- Lawrence, A. 1987, *PASP*, 99, 309
- Le Fevre, O., Saisse, M., Mancini, D., Vettolani, G., Maccagni, D., Picat, J. P., Mellier, Y., Mazure, A., Cuby, J., Delabre, B., et al. 2000, in *Optical and IR Telescope Instrumentation and Detectors*, eds. Masanori I., Moorwood A. F. M., Proc. SPIE, 4008, 546
- Lucy, L. B. 1974, *AJ*, 79, 745
- Maiolino, R., & Rieke, G. H. 1995, *ApJ*, 454, 95
- Maiolino, R., Ruiz, M., Rieke, G. H., & Keller, L. D. 1995, *ApJ*, 446, 561
- Maiolino, R., Krabbe, A., Thatte, N., & Genzel, R. 1998, *ApJ*, 493, 650
- Maiolino, R., Alonso Herrero A., Anders S., Quillen A., Rieke M., Rieke G., & Tacconi-Garman, L. 2000, *ApJ*, 531, 219
- Maloney, P. 1997, *Ap&SS*, 248, 105
- Marco, O., Alloin, D., & Beuzit, J. L. 1997, *A&A*, 320, 399
- Marrone, D. P., Moran, J. M., Zhao, J., & Rao, R. 2007, *ApJ*, 654, L57
- Marconi, A., Moorwood, A. F. M., Salvati, M., & Oliva, E. 1994, *A&A*, 291, 18
- Marconi, A., Moorwood, A. F. M., Origlia, L., & Oliva, E. 1994, *The ESO Messenger*, 78, 20
- Marconi, A., & Hunt, L. 2003, *ApJ*, 589, L21

- Mason, R.E., Geballe, T.R., Packham, C., Levenson, N.A., Elitzur, M., Fisher, R. S., & Perlman, E. 2006, *ApJ*, 640, 612
- Matt, G., Fiore, F., Perola, G., Piro, L., Fink, H. H., Grandi, P., Matsuoka, M., Oliva, E., & Salvati, M. 1996, *MNRAS*, 281, L69
- Matt, G., Guainazzi, M., Frontera, F., Bassani, L., Brandt, W. N., Fabian, A. C., Fiore, F., Haardt, F., Iwasawa, K., Maiolino, R., et al. 1997, *A&A*, 325, L13
- Matt, G., Guainazzi, M., Maiolino, R., Molendi, S., Perola, G. C., Antonelli, L. A., Bassani, L., Brandt, W. N., Fabian, A. C., Fiore, F., et al. 1999, *A&A*, 341, L39
- McCarthy, D. W., Sabatke, E. M., Sarlot, R. J., Hinz, P. M., & Burge, J. H. 2000, in *Interferometry in Optical Astronomy*, eds. Pierre J. Lena, Andreas Quirrenbach, Proc. SPIE, 4006, 659
- Meurer, G. R., Heckman, T. M., Leitherer, C., Kinney, A., Robert, C., & Garnett, D. R. 1995, *ApJ*, 110, 2665
- Michelson, A. A., & Pease, F. G. 1921, “Measurement of the diameter of α orionis with the interferometer”, *ApJ*, 53, 249.
- Miller, J.S., & Antonucci, R.R.J. 1983, *ApJ*, 271, L7
- Miller, J. S., Goodrich, R. W. & Mathews, W. G. 1991, *ApJ*, 378, 47
- Mirabel, I. F., Booth, R. S., Garay, G., Johansson, L. E. B., & Sanders, D. B. 1990, *A&A*, 236, 327
- Müller Sánchez, F., Davies, R. I., Eisenhauer, F., Tacconi, L.J., Genzel, R., & Sternberg, A. 2006, *A&A*, 454, 481
- Müller Sánchez, F., Davies, R. I., Genzel, R., Tacconi, L.J., Eisenhauer, F., Hicks, E., Friedrich, S., & Sternberg, A. 2008a, *ApJ*, to be submitted
- Müller Sánchez, F., et al. 2008b, in prep.
- Müller Sánchez, F., Eisenhauer, F., Genzel, R., Gál, C., Krabbe, A., & Herbst, T. 2008c, *ApJS*, to be submitted
- Müller Sánchez, F., et al. 2008d, in prep.
- Marcuse, D. 1975, *Applied Optics*, 14, 3016
- Neri Vela, R. 1999, “Líneas de Transmisión”, McGrawHill, Mexico
- Nenkova, M., Ivezić, Ž., Elitzur, M. 2002, *ApJ*, 570, L9

- Neufeld, D. A., Maloney, P. R., & Conger, S. 1994, ApJ, 436, L127
- Neumann, E. G. 1988, "Single-mode fibers", Springer Series in Optical Sciences, Berlin
- Oliva, E., Salvati, M., Moorwood, A. F. M., & Marconi, A. 1994, A&A, 288, 457
- Oliva, E., Marconi, A., Cimatti, A., & di Serego Alighieri, S. 1998, A&A, 329, L21
- Oliva, E., Marconi, A., & Moorwood, A. F. M. 1999, A&A, 342, 87
- Onken, C., Ferrarese, L., Merritt, D., Peterson, B., Pogge R., Vestergaard, M., & Wandel, A. 2004, ApJ, 615, 645
- Osterbrock, D. E. 1989, "Astrophysics of Gaseous Nebulae and Active Galaxies", University Science Books, USA
- Ozernoy, L., & Genzel, R. 1996, eds Blitz L., Teuben P., Kluwer Proc. IAU Symposium 169, p.181
- Poncelet, A., Perrin, G., & Sol, H. 2006, A&A, 450, 483
- Poncelet, A., Doucet, C., Perrin, G., Sol, H., & Lagage, P. O. 2007, A&A, 472, 823
- Parry, I., Bunker, A., Dean, A., Doherty, M., Horton, A., King, D., Lemoine-Busserole, M., Mackay, C. D., McMahon, R. Medlen, S., et al. 2004, in *Ground-based Instrumentation for Astronomy*, eds. A. F. M. Moorwood and M. Iye, Proc. SPIE, 5492, 1135
- Paumard, T., Genzel, R., Martins, F., Nayakshin, S., Beloborodov, A. M., Levin, Y., Trippe, S., Eisenhauer, F., Ott, T., et al., 2006, ApJ, 643, 1011
- Perrin, G., Lai, O., Woillez, J. M., Guerin, J., Kotani, T., Vergnole, S., Adamson, A. J., Ftaclas, C., Guyon, O., Lena, P. J. et al. 2004, in *New Frontiers in Stellar Interferometry*, eds. Wesley A. Traub, Proc. SPIE, 5491, 391
- Petrov, R., Malbet, F., Richichi, A., Hofmann, K. H., Mourard, D., Agabi, K., Antonelli, P., Aristidi, E., Baffa, C., Beckmann, U., et al. 2000, in *Interferometry in Optical Astronomy*, eds. Pierre J. Lena, Andreas Quirrenbach, Proc. SPIE, 4006, 68
- Pier, E., & Krolik, J. 1992, ApJ, 401, 99
- Pier, E., Krolik, J. 1993, ApJ, 418, 673
- Prieto, M. A., Meisenheimer, K., Marco, O., Reunanen, J., Contini, M., Clenet, Y., Davies, R. I., Gratadour, D., Henning, Th. Klaas, U., et al. 2004, ApJ, 614, 135

- Prieto, M. A., Marco, O., & Gallimore, J. 2005, MNRAS, 364, L28
- Rees, M. J., 1984, ARA&A, 22, 471
- Rhee, J. H., & Larkin, J. E. 2006, ApJ, 640, 625
- Robson, I. 1996, "Active Galactic Nuclei", Praxis Publishing Ltd, Chichester, UK
- Rodríguez-Ardilla A., Pastoriza, M., Viegas, S., Sigut, T., Pradhan, A. 2004, A&A, 425, 457
- Rotaciuc, V., Krabbe, A., Cameron, M., Drapatz, S., Genzel, R., Sternberg, A., & Storey, J.W.V. 1991, ApJ, 370, L23
- Rouan, D., Rigaut, F., Alloin, D., Doyon, R., Lai, O., Crampton, D., Gendron, E., & Arsenault, R. 1998, A&A, 339, 687
- Rouan, D., et al. 2004, A&A, 417, L1
- Sarzi, M., Shields, J., Pogge, R., & Martini, P. 2007, in *Stellar Populations as Building Blocks of Galaxies*, eds. Peletier R., Vazdekis A., IAU Symposium 241, 489
- Seyfert, C. K. 1943, ApJ, 97, 28
- Shaklan, S., & Roddier, F. 1988, Appl. Opt., 27, 2334
- Schartmann, M., Meisenheimer, K., Camenzind, M., Wolf, S., Henning, Th. 2005, A&A, 437, 861
- Schartmann, M. 2007, PhD Thesis, MPIA Heidelberg
- Schinnerer, E., Eckart, A., Tacconi, L. J., Genzel, R., & Downes, D. 2000, ApJ, 533, 850
- Stasinska, G. 1984, A&A, 135, 341
- Sternberg, A. 1998, ApJ, 506, 721
- Storchi-Bergmann, T., González Delgado, R., Schmitt, H., Cid Fernandes, R., & Heckman, T. 2001, ApJ, 559, 147
- Sugai, H., Malkan, M., Ward, M., Davies, R., & McLean, I. 1997, ApJ, 481, 186
- Sugai, H., Davies, R., Ishii, M., & Ward, M. 2000, MNRAS, 317, 447
- Sutherland, R. S., Bicknell, G.V., & Dopita, M. A. 1993, ApJ, 414, 510

- Tacconi, L. J., Genzel, R., Blietz, M., Cameron, M., Harris, A. I., & Madden, S. 1994, ApJ, 426, L77
- Tacconi, L. J., Genzel, R., Tecza, M., Gallimore, J. F., Downes, D., & Scoville, N. Z. 1999, 524, 732
- Tecza, M., & Thatte, N. 1998, ASPC, 152, 271
- Tecza, M., Thatte, N., & Maiolino, R. 2001, IAUS, 205, 216
- Tecza, M., Thatte, N., Clarke, F., Goodsall, T., & Symeonidis, M. 2006, New Astronomy Reviews, 49, 647
- Telesco, C. M., & Harper, D. A. 1980, ApJ, 235, 392
- Thatte, N., Quirrenbach, A., Genzel, R., Maiolino, R., & Tecza, M. 1997, ApJ, 490, 238
- Thornley, M., Förster Schreiber, N., Lutz, D., Genzel, R., Spoon, H., Kunze, D., & Sternberg, A. 2000, ApJ, 539, 641
- Tomono, D., Doi, Y., Usuda, T., & Nishimura, T. 2001, ApJ, 557, 637
- Tomono, D., Terada, H., & Kobayashi, N. 2006, ApJ, 646, 774
- Tran, H. D. 2001, ApJ, 554, L19
- Tremaine, S., Gebhardt, K., Bender, R., Bower, G., Dressler, A., Faber, S. M., Filippenko, A. V., Green, R., Grillmair, C., Ho, L. C., et al. 2002 ApJ, 574, 740
- Tristram, K. R. W., Meisenheimer, K., Jaffe, W., Scharmann, M., Rix, H.-W., Leinert, Ch., Morel, S., Wittkowski, M., Röttgering, H., Perrin, G., et al. 2007, A&A, 474, 837
- Urry, C. M., & Padovani, P. 1995, PASP, 107, 803.
- Vestergaard, M. 2002, ApJ, 571, 733
- Vestergaard, M. 2004, ApJ, 601, 676
- Wallace, J. K., Boden, A. F., Colavita, M., Dumont, P. J., Gursel, Y., Hines, B. E., Koresko, C., Kulkarni, S. R., Lane, B., Malbet, F., et al. 1998, in *Astronomical Interferometry*, eds. Robert D. Reasenberg, Proc. SPIE, 3350, 864
- Weigelt, G., Wittkowski, M., Balega, Y. Y., Beckert, T., Duschl, W. J., Hofmann, K.-H., Menshchikov, A. B., & Schertl, D. 2004, A&A, 425, 77

Weitzel, L., Krabbe, A., Kroker, H., Thatte, N., Tacconi-Garman, L. E., Cameron, M., & Genzel, R. 1996, *A&AS*, 119, 531

Wittkowski, M., Kervella, P., Arsenault, R., Paresce, F., Beckert, T., & Weigelt, G. 2004, *A&A*, 418, L39

Young J., & Scoville N. 1991, *ARA&A*, 29, 581

Young, S., Packham, C., Hough, J. H., & Efstathiou, A. 1996, *MNRAS*, 283, L1

Acknowledgements

First and foremost I would like to thank my primary supervisor Prof. Dr. Reinhard Genzel for providing me the opportunity to complete a PhD in Astronomy in the Infrared Group, always encouraging me to move in new directions and motivating me to do very good science.

I very much thank my supervisors Dr. Frank Eisenhauer and Dr. Ric Davies for my training as an astronomer. Most of my knowledge I learned from them. I thank them for all the patience, advices and experiences.

I also would like to thank to all the members of the Nearby AGN group for the fruitful collaboration: Erin Hicks, Susanne Friedrich and Hauke Engel. I extend thanks to the whole engineering group and workshop staff, especially Marcus Haug who helped me with the design, manufacturing and setup of my experiments. Special thanks to Linda Tacconi for always supporting me with professional advice and managerial work, and thanks to Susane Harai-Ströbl for taking care of administrative tasks.

I would like to thank Sebastian Rabien, Dieter Lutz, Eckart Sturm, Albrecht Poglitsch, Stefan Gillessen, Roberto Abuter, Natascha Förster-Schreiber, Thomas Ott and all the other current and past members of the Infrared Group for the pleasant working atmosphere and offering me their support when I needed it.

I am grateful to all my office mates over the years Mario Schweitzer, Yohei Harayama and Katie Dodds-Eden for help, advice, distraction and most of all for their friendship and I thank Giovanni Cresci, Fabrice Martins, Elisabetta Valiante, Sascha Trippe and Peter Buschkamp for their friendship and the many joyful hours.

I extend my deepest thanks to my family. I would like to especially thank my mother and father for their love and encouragement. I credit my mother Gloria for inspiring my love of science. Thanks to my brother Adolfo. There is not enough space in this entire dissertation to list all the nice things he has done for me. Finally, I would like to thank my beloved Serpil for not only providing all the normal kinds of support and understanding that a slightly stressed PhD student needs, but also for proofreading this dissertation and inspiring me to name the instrumental project of my thesis.